# PROSPECTIVE AND RETROSPECTIVE RETOOLING OF MAGNETIC RESONANCE IMAGING AND RECONSTRUCTION

A Dissertation
Presented to
The Academic Faculty

By

Nishant Zachariah

In Partial Fulfillment
of the Requirements for the Degree
Doctor of Philosophy in the
School of Electrical and Computer Engineering

Georgia Institute of Technology

August 2017

**PROSPECTIVE AND RETROSPECTIVE RETOOLING OF MAGNETIC RESONANCE IMAGING AND RECONSTRUCTION**

Approved By:

Dr. Justin K. Romberg, Chair and Advisor
School of Electrical and Computer Engineering
*Georgia Institute of Technology*

Dr. Xiaoping P. Hu, Co-Advisor
Department of Bioengineering
*University of California at Riverside*

Dr. Christoper J. Rozell
School of Electrical and Computer Engineering
*Georgia Institute of Technology*

Dr. John Oshinski
Department of Radiology and Biomedical Engineering
*Emory University and Georgia Institute of Technology*

Dr. Robert Butera
School of Electrical and Computer Engineering
*Georgia Institute of Technology*

Dr. Shella Keilholz
Department of Biomedical Engineering
*Emory University and Georgia Institute of Technology*

Approved On : April 18, 2017

*”Do nothing out of selfish ambition or vain conceit. Rather, in humility value others above yourselves.”*

Philippians 2:3

*”True humility is not thinking less of yourself, it is thinking of yourself less”*

Clive Staples Lewis

To little Gideon, for filling our lives as parents with such indescribable joy.

## ACKNOWLEDGEMENTS

I was once told during my master's training at a different institution, that you know when you are ready to graduate when the student becomes the teacher. If I had lived by that piece of advice, I would be at Georgia Tech for another decade. I have been incredibly blessed to train under two exceptional researchers: Dr. Justin Romberg and Dr. Xiaoping Hu. The two of them represent the quintessential drivers of scientific thought in their respective disciplines. They are more than crafters of their fields, they are pioneers. I have learned more science and engineering from each of them than I have from anyone in my combined 11 years as a professional undergraduate, masters and PhD student.

In the years that I have known Dr. Romberg, his ability to recast any complex problem into the framework of harmonic analysis / advanced linear algebra baffles me to this day. It is an incredibly useful skill that I can only hope to hone in the years to come. I can remember countless meetings in his office talking about specific research challenges where his insights have saved me months of work chasing down dead ends. For anyone who knows Dr. Romberg, the hallmarks of his character are his exceptional work ethic and his dedication to the penultimate teaching standard. Those who know him less well, will not know of his constant unending ability to ruminate and innovate when faced with a technical problem. I have received emails from him at 3am with new insights that he might have had. When I think of Dr. Romberg, I think of C.S. Lewis who said, "The task of the modern educator is not to cut down jungles, but to irrigate deserts".

Integral to my graduate journey was a fateful meeting that I had in April of 2012 at Emory University with Dr. Hu. I realized then and in the next 4 years, that to spend time with Dr. Hu, was to spend time in the presence of ideas. In nearly half a decade of lab meetings with him, I cannot remember a single one in which novel research directions were not discussed / handed to one of us to explore. In all the time that I spent at his lab at Emory University, I was always struck by his constant faith in both my potential and his

desire to see me rise to that potential. He gave me a wide latitude and encouraged me to set my own direction and pace. All the while, being available if I needed him.

Looking back at the last five years, it is hard for me to miss the patience and fortitude with which Dr. Romberg and Dr. Hu have mentored me. They found a healthy balance between letting me run off into the deep and reeling me back into practical waters. They have been the best mentors that I could have ever hoped to have. I am and always will be deeply indebted to them for the roles that they have played in shaping the engineer that I am today.

Dr. Rozell, Dr. Oshinski, Dr. Keilholz and Dr. Butera form the core, without whom this part of my formal training would not be possible. They have been kind enough to take time out of their busy schedules to both pour over this dissertation and my defense. I am deeply grateful for their altruism and the effort they continue to invest in me through this process to make me a better trainee.

Graduate school would have been exceeding dull had it not been for my peers in the BITC core, Romberg, Rozell and Davenport labs. I am thankful for their support. I am especially grateful to Jason Langley, Shiyang Chen, Candace Fleicher, Mac Merritt and Sangoen Park for their friendship and countless conversations about life, signal processing and everything in between. Anant Giridar, Siddharth Varughese and Deepu Jose were and still are, friends that Christa and I made late in graduate school. The board game nights, resident life programs and Bible study sessions will always form cherished memories of the invaluable nature of great friends.

Through it all, there were two individuals who never stopped believing : dad and mom. They pushed me, prodded me, prayed for me and encouraged me every single day. If a cumulative sum were to be computed, my dad and mom have probably spent entire months of their lives, on their knees praying for me. They have taught me to love, to live and to learn. Everything that I have learned from them did not come out of dogmatic pedagogy but rather as an outworking of the sacrificial lives that they have led for me through the

years. They have always put me first, always taken the harder road on my account while still giving me room to fail. I cannot envision how they found time to be successful in their own professional lives while still investing incredible amounts of time in me. I can only hope to be as good a parent to Gideon as they have been to me.

My rock and the source of unending encouragement has been my best friend and my wife, Christa. From the existential crises that punctuate graduate life, to the elation at getting a simulation to work after months of failure, she has been my shoulder to lean on. She has picked me up at my lowest of lows and celebrated with me at the highest highs. I cannot envision this journey or the last ten years without her. At every turn, she always had an encouraging word and a steady hand for me to grab a hold of. As a scientist, engineer, mother, wife and daughter to my parents, Christa inspires me with every hat that she wears. It has been and continues to be an honor to run this race of life by her side.

Gideon our son, has transformed Christa's and my life in so many ways. His smile haunts us while we at work and brings such jubliant exultation while we are at home. Gideon, despite being only 7 months old, teaches me daily. Often when masked in the veneer of graduate school challenges, his very presence brings clairvoyance to that which truly matters.

*Soli Deo Gloria*

*Solo Christo*

**TABLE OF CONTENTS**

## LIST OF TABLES

## LIST OF FIGURES

## SUMMARY

At its heart, signal processing can be broken down into two broad categories based on a single core query. How can a given objective (higher resolution, reduction in noise interference, statistical inferences, signal separation / characteristic etc) be achieved when the data has been acquired (retrospective) versus how the acquisition system must be designed to achieve the desired objective(prospective). In this work, we consider retrospective and prospective medical image reconstruction with special attention to magnetic resonance imaging.

Convex relaxations of sparse priors have given birth to strident improvements in the way signals are recovered from underdetermined systems. In the retrospective vein of image reconstruction, we seek to extend the benefits afforded by sparse regularization through the use of non convex sparse priors. We develop a novel algorithmic solution, both in its design and computational efficiency, for analysis based non convex sparse priors in tight frames. Theoretically, we show that our algorithm is guaranteed to converge to a local minimum based on the non convex objective function being examined. Numerically, this class of non convex regularized linear inverse problems have a range of practical applications: underdetermined signal recovery, single image super-resolution and image denoising. In each of these applications, we demonstrate that our non convex formulation can out perform both convex and non convex state of the art counterparts.

In order to truly achieve a desired objective, both the data acquisition methodology and reconstruction pipeline must be jointly constructed. Speed of imaging is of great concern in magnetic resonance imaging (MRI). In MR systems, faster imaging translates to a range of benefits from increased temporal / spatial resolution to reduced motion artifacts. In the prospective approach, we develop a novel MR data acquisition and reconstruction framework to accelerate MR imaging beyond what is currently commercially available. This is done by leveraging phase encoding gradients during the data acquisition process thereby

affording better control over the spectral distribution of the underlying encoding operator. In doing so, we are able to decorrelate the coils to recover signals higher acceleration factors than the current state of the art. We demonstrate the viability of our method through proof of concept 1D simulations and 3D phantom data acquired on a 3T human scanner. Finally, our reconstruction methodology forms a generalized framework seamless transition between 1D and 3D MR image reconstruction.

# Part I

# Retrospective Retooling

# CHAPTER 1

# INTRODUCTION

## 1.1 Overview

In this work, we formulate a novel algorithmic solution for the analysis non convex problem

$$\min_{\vec{x}\in\mathbb{C}^n}\left(\frac{1}{2}\left\|\boldsymbol{A}\left(\vec{x}\right)-\vec{y}\right\|_2^2+\lambda\left\|\boldsymbol{W}\left(\vec{x}\right)\right\|_p^p+\iota_C(x)\right) \tag{1.1}$$

where $0 \leq p \leq 1$, $\boldsymbol{A}(\cdot)$ is a linear operator which maps $\mathbb{C}^n \rightarrow \mathbb{C}^m (m << n)$, $\boldsymbol{y} \in \mathbb{C}^m$, $\boldsymbol{W}(\cdot)$ is a tight frame which maps $\mathbb{C}^n \rightarrow \mathbb{C}^k$ where $k > n$ and $\iota_C(\vec{x})$ is an indicator for the convex set C. In addition, we also solve the total variation regularized non convex recovery problem

$$\min_{\vec{x}\in\mathbb{C}^n}\left(\frac{1}{2}\left\|\boldsymbol{A}\left(\vec{x}\right)-\vec{y}\right\|_2^2+\lambda_1\left\|\boldsymbol{W}\left(\vec{x}\right)\right\|_p^p+\lambda_2\left\|\vec{x}\right\|_{TV}+\iota_C(\vec{x})\right). \tag{1.2}$$

Our algorithm IAN (**I**terative **A**nalaysis based **N**on-convex solver), solves the optimization problem specified in (1.1) and (1.2) by integrating a proximal splitting framework [1] with an iteratively estimated optimal shrinkage operator for a given $L_p$ norm [2].

## 1.2 Background

The least squares approach to solving ill conditioned or under determined linear inverse system

$$\min_{\vec{x}\in\mathbb{C}^n}\left(\frac{1}{2}\left(\left\|\boldsymbol{A}\left(\vec{x}\right)-\vec{y}\right\|_2^2\right)\right.$$

where $\vec{y} \in \mathbb{C}^m, \boldsymbol{A}(\cdot)$ is a mapping from $\mathbb{C}^n$ to $\mathbb{C}^m$ $(m << n)$ is inadequate for most signal recovery applications. In these under determined cases, signal recovery is greatly

aided by the injection of apriori information about the type of behavior we expect from the recovered signal $(\vec{x})$. In the signal processing literature, apriori information takes the form of regularization. In the late 1940s, a method was proposed to control the overall energy of the signal while explicitly controlling the trade off with the true least least squares solution [3, 4]. This method results in an optimization problem that takes the well known form:

$$\min_{\vec{x}\in\mathbb{C}^n} \left( \frac{1}{2} \left\| \boldsymbol{A}\left(\vec{x}\right) - \vec{y} \right\|_2^2 + \lambda \left\| \vec{x} \right\|_2^2 \right).$$

This optimization problem, like the least squares problem, has an analytic closed form solution. When dealing with under-determined systems, conjecturing signal sparsity has resulted in remarkable breakthroughs [5, 6, 7, 8, 9, 10]. Formally, the convex version of enforcing a sparse prior takes the form of the $L_1$ norm. The $L_1$ regularized recovery problem then takes the form

$$\min_{\vec{x}\in\mathbb{C}^n} \left( \frac{1}{2} \| \boldsymbol{A}\left(\vec{x}\right) - \vec{y} \|_2^2 + \lambda \| \vec{x} \|_1 \right), \tag{1.3}$$

The ability to solve the optimization problem (1.3) laid the foundation for the field of compressive sensing. Early work focused on the specfic constraints under which the optimization problem (1.3) was feasible. The number of samples required for exact recovery was shown to be on the order of $C(S\log(n))$ where $C$ is a fixed constant, $S$ is the number of non zero entries in $\vec{x}$ and $n$ is the dimensionality of $\vec{x}$ [11, 5, 12]. Furthermore, it was demonstrated that the encoding matrix $\boldsymbol{A}()$ must satisfy the restricted isometry property (RIP) [5, 13, 14]. Briefly stated, the restricted isometry property states that for every $S$ sparse vector $\vec{z} \in \mathbb{R}^n$, there exists a $\delta$ for which the expression

$$(1-\delta)\|\vec{z}\|_2^2 \leq \|\boldsymbol{A}(\vec{z})\|_2^2 \leq (1+\delta)\|\vec{z}\|_2^2$$

holds. The ability to solve problems of the form (1.3) has generated breakthroughs in the fields ranging from radar signal processing to medical imaging [15, 16, 17, 8, 6, 18, 19]. While the number of publications in the compressive sensing field has grown to well over tens of thousands, we discuss only a few seminal papers here for brevity. Integral to the rapid adaptation of the $L_1$ sparse prior in a range of applications was the development of a proximal $L_1$ shrinkage operator by Ingrid Daubechies and colleagues [20]. The utilization of a proximal map provided an alternative to the second order cone programitic approach that was presented by the original pioneers of compressed sensing [5, 6, 11]. Daubechies was able to demonstrate that the proximal $L_1$ operator could be used in a trivial forward backward splitting approach [20]. The proximal operator $S$ itself has a closed form that can be written as

$$S_\lambda(z) = \begin{cases} z+\lambda & if \quad z < \lambda \\ 0 & if \quad |z| < \lambda \\ z-\lambda & if \quad z > \lambda \end{cases}$$

where $\lambda$ is the regularization parameter and $z \in \mathbb{R}$. Thus the operator functions on each component of a vector independently of another. From the definition of the operator it is trivial to see that $\|\boldsymbol{S}(\vec{z})\| < \|\vec{z}\| \quad \forall \vec{z} \in \mathbb{R}^n$. In the complex case, the operator can be rewritten to function on the magnitude:

$$S_\lambda(z) = \begin{cases} (|z|+\lambda)\exp^{(i(\arg(z)))} & if \quad |z| < -\lambda \\ 0 & if \quad |z| < \lambda \\ (|z|+\lambda)\exp^{(i(\arg(z)))} & if \quad |z| > -\lambda \end{cases}$$

where $z \in \mathbb{C}$. While the development of a proximal operator was pivotal, the original algorithm developed in Daubechie's work (ISTA) [20] was slow to converge. Beck and Teboulle adapted Nesterov's acceleration technique [21] to ISTA [9]. In doing so, they developed

an algorithmic method that kept the simplicity of ISTA but drastically accelerated the system's convergence rate without significantly increasing the computational complexity of each iterate [9].

Mathematically, the truly sparse prior requires replacing the $\|\cdot\|_1$ in (1.3) with the non convex $L_0$ norm $\|\cdot\|_0$. This makes the problem highly non convex and algorithmically intractable. The convex relaxation of the $L_0$ norm on the other hand benefits from the advantages afforded by convexity (local minimum is a global minimum) and has well established stable algorithmic formulations [9, 22, 23, 24].

There has also been algorithmic work exploring the non convex optimization problem

$$\min_{\vec{x}\in\mathbb{C}^n}\left(\frac{1}{2}\left\|\boldsymbol{A}\left(\vec{x}\right)-\vec{y}\right\|_2^2+\lambda\left\|\vec{x}\right\|_p^p\right).$$

Recent work [25, 26, 27, 28, 29, 2, 30, 31] has demonstrated the ability of non-convex prior based recovery to surpass standard convex prior ($L_1$) based recovery. Non convex problems of this form have been shown to be especially beneficial in medical imaging [29, 31, 32, 33, 34, 35].

As the core of our work revolves around the use of proximal algorithms with tight frame analysis non convex priors. Background on each of these four concepts are briefly presented here.

### 1.2.1 Non Convex Priors

The most common method used to approximate the $L_0$ norm is through the use of reweighted $L_1$. Reweighted $L_1$ uses a weighting matrix to transform the $L_1$ magnitude contribution of a vector into its pseudo $L_0$ counterpart [36]. The optimization problem takes the form

$$\min_{\boldsymbol{x}\in\mathbb{C}^n}\frac{1}{2}\|\boldsymbol{A}(\vec{x})-\vec{y}\|_2^2+\lambda\|\boldsymbol{D}\vec{(}x)\|_1$$

(where $\boldsymbol{D}$ is a diagonal weighting matrix) and has garnered significant algorithmic and analytic attention [36, 37, 38, 39, 25, 26]. Reweighted $L_1$ functions by designing a weighting matrix that seeks to negate the magnitude of each norm component by scaling each entry (approximately) by its own magnitude with an additive scalar offset (for stabiliy) [36]. In doing so, the $L_1$ ball is slowly morphed into a geometric form that is closer to the $L_0$ ball. The diagonal entries of the matrix $D$ can be written as

$$d_j^{(i)} = \frac{1}{x_j^{(i)} + \epsilon}$$

where $j$ is the $j$ th element, $i$ is the iteration number and $\epsilon$ is the scalar additive factor that stabilizes the recovery when $x_j^i = 0$.

The authors in [25, 26] develop a state of the art reweighted analysis $L_1$ solver (SARA) based on Douglas Rachford splitting. The challenge with [25, 26] is a lack of global control over the final non-convex norm that the solution converges to. In short, this type of formulation results in a loss of control over the exact optimization problem being solved. Furthermore, the reweighted algorithm architecture requires a nested iterative structure which results in very high computational cost. We will demonstrate in later sections, that even with the default parameter settings of [25, 26], our method (IAN) converges to quantitatively better results with an order of magnitude less computational cost than SARA. Furthermore, if the threshold and maximum iteration bounds are ignored, SARA requires specification of three times as many parameters as IAN (6 parameter versus 2 respectively).

Other work has sought to approximate the $L_0$ norm directly [40, 41, 42, 43]. The optimization problem in this case, takes the form

$$\min_{\boldsymbol{x} \in \mathbb{C}^n} \frac{1}{2} \left\| \boldsymbol{A}\left(\vec{x}\right) - \vec{y} \right\|_2^2 + \lambda \|\vec{x}\|_0.$$

In [43], the $L_0$ optimization problem is directly applied for signal deconvolution through

the use of hard thresholding. The hard thresholding operator typically takes the form [44] :

$$H_\lambda(z) = \begin{cases} 0 & if \quad |z| < \lambda^{0.5} \\ z & if \quad |z| > \lambda^{0.5} \end{cases}$$

Hard thresholding, while appealing from a theoretical perspective, has found limited practical application given its limited tolerance to poor initialization [44, 45]. Furthermore, the direct choice of the $L_0$ norm instead of the $L_p$ norm where $0 < p < 1$, is restrictive as the optimal norm might vary based on application.

The last major class of algorithms used to approximate $L_0$ norm, seeks to solve the $L_p$ norm problem for $p < 1$. In [32, 33, 34, 35] the authors use a Laplacian functional form to approximate the $L_p$ prior for specific applications such as MR angiography. The authors impose an image smoothness constraint in the form of finite difference sparsity. The authors do not explore the benefits of signal sparsity in a frame / basis. The iterative shrinkage used in our work is based on the generalized shrinkage and thresholding method outlined in [2]. As such, it is neccesary to discuss where our work diverges. In [2], the authors present a generalized shrinkage and thresholding methodology for $L_p$ regularization. In contrast with [2], we consider the harder analysis reconstruction problem as opposed to the synthesis reconstruction problem that was presented in [2]. Unlike [2], our algorithmic framework leverages the benefit of proximal algorithms and tight frames while also providing convergence guarantees. In [31], Chartrand approaches the non-convex optimization problem by implementing a split Bregmann approach for reconstructing highly undersampled Shepp Logan phantom image. The closed form shrinkage operator that Chartrand utilizes for $L_p$ recovery is

$$S_p^\lambda(z) = \max(|z| - \lambda|z|^{p-1}, 0)\frac{z}{|z|}$$

where $p < 1$ and $\lambda$ is the regularization parameter [31]. It must be noted that in order to ob-

tain a closed form shrinkage operator, the optimization objective is altered into a non closed form expression. In doing so, the algorithm presented in [31] does not attempt to minimize the same objective function as in our work. However in the interest of throughness, since the algorithm [31] was designed for undersampled recovery, we benchmark our undersampled recovery results against the algorithm presented in [31]. In doing so, we demonstrate IAN's ability to reconstruct the underlying signal with greater fidelity. Furthermore, it must be noted that the authors in [31] failed to provide any form of convergence analysis. The computational cost of the non convex algorithm presented in [31] is approximately twice as expensive as our method (IAN).

### 1.2.2 Analysis versus Synthesis Priors

In enforcing sparse priors, a subtlety revolves in the formulation of the problem. The problem can be formulated to recover either the signal itself (analysis) or the transform coefficients signal in the basis / frame that the signal is sparse in (synthesis). The two types of prior formulation result in different results under certain conditions. The standard synthesis prior based recovery takes the form

$$\min_{\alpha \in \mathbb{C}^k} \left( \frac{1}{2} \left\| \boldsymbol{A} \left( \boldsymbol{W}^* \left( \vec{\alpha} \right) \right) - \vec{y} \right\|_2^2 + \lambda \| \vec{\alpha} \|_p^p \right)$$

where $\vec{\alpha} = \boldsymbol{W}(\vec{x})$. Analysis based recovery on the other hand, seeks to reconstruct the signal

$$\min_{\vec{x} \in \mathbb{C}^n} \left( \frac{1}{2} \left\| \boldsymbol{A} \left( \vec{x} \right) - \vec{y} \right\|_2^2 + \lambda \left\| \boldsymbol{W} \left( \vec{x} \right) \right\|_p^p \right)$$

These two methods are equivalent when dealing with injected / assumed sparsity in a basis. However, when the signal is conjectured to be sparse in a frame, the two recovery methods loose their equivalence [46]. The authors in [46] were able to show that analysis based signal priors can outperform synthesis based priors for sparse recovery. The fundamental

difference between the two methods can be found in its construction. The synthesis prior is highly dependent on each dictionary element with co-dependence between the elements that are active [46]. Analysis priors on the other hand weigh each dictionary element with the same priority thereby providing for stable reconstruction [46]. This difference is best understood from the perspective of high dimensional geometry. The polytope defined by the analysis $L_1$ operator has a large number of vertices with very low "neighborliness" [46]. The synthesis $L_1$ polytope on the other hand has the exact opposite [47]. In the $L_1$ case, it can be shown that the analysis prior is a subset of the synthesis prior (provided the synthesis dictionary was appropriately expanded) [46]. For denosing of natural images, analysis priors outperformed synthesis priors [46]. Furthermore, they noticed that analysis sparse priors tended to be less sensitive to proper regularization relative to synthesis sparse priors. This can be understood geometrically as outlined earlier or from an algebraic standpoint. Analysis priors enforce a joint recovery where all the dictionary elements are utilized simultaneously thereby providing for stable reconstruction in the presence of noise [46].

This results has subsequently been corroborated in other work. In [48] Selsenick and Figueiredo examined the recovery afforded by $L_1$ analysis and synthesis priors for denoising and deconvolution. They found, as in [46], that analysis sparse priors far outperformed synthesis priors for natural signals. Intrestingly, analysis priors have been shown to recover the underlying signal with greater fidelity even in the non convex case. In [49] the authors demonstrated the ability of analysis based reweighted $L_1$ to recover radar like modulated signal perfectly. In fact, the authors in [49] did not utilize a synthesis based reweighted $L_1$ approach since (presumably) the results they obtained with sythesis based $L_1$ was worse than that obtained with analysis based $L_1$ (see Fig. 11 in [49]).

Finally, synthesis based approaches require that the combination of the sensing matrix and the sparsifying transform remain incoherent for guaranteed signal recovery. In recent theoretical work [50], provable recovery guarantees were shown for even maximally co-

herent dictionaries provided an analysis based signal recovery framework was employed.

### 1.2.3 Proximal Methods

The following section is a brief summary of the work presented in [1, 51]. To understand the utilization of proximal methods, we must begin with a generic optimization problem. Given the following problem :

$$\min_{x \in \mathbb{R}^n} \sum_i g_i(\vec{x})$$

where $g_i(\cdot)$ is some "well behaved" (notions of smoothness, convexity etc) function. Then the proximal method to solve this optimization problem will seek to solve a series of smaller (and hopefully computationally simpler) optimization problems

$$prox_{g_i}\ y = \min_{\vec{z} \in \mathbb{R}^n} \frac{1}{2}\|\vec{y} - \vec{z}\|_2^2 + g_i(\vec{z})$$

From this, it is easy to envision the nested nature that could be utilized to enforce each proximal operator based on the result obtained from the previous application. By relaxing each sub-problem into the form shown above, we tradeoff computational tractability with accuracy. More strictly, we gain analytical properties that are important for demonstrating convergence : non-expansiveness of the operators [1]. Strict non-expansiveness is defined as

$$\|prox_g(\vec{u}) - prox_g(\vec{v})\|^2 + \|(\vec{u} - prox_g(\vec{u})) - (\vec{v} - prox_g(\vec{v}))\|^2 \leq \|\vec{u} - \vec{v}\|^2$$

$\forall \vec{u}, \vec{v} \in \mathbb{R}^n$. Forward backward splitting, alternating projections, Douglas Rachford splitting, Dykstra like splitting are all examples classes of algorithms that leverage proximal optimization methods [1]. Proximal algorithms are particularly desirable for non convex objective functions as they make the underlying optimization problem tractable [30]. An

important difference that needs to be highlighted lies in the formulation difference between the Douglas Rachford splitting method (which is used in the competing reweighted $L_1$ algorithm we compare our results with : SARA [25]) and Dykstra like splitting which is utilized in our method. Douglas Rachford splitting allows for the minimization of an objective functional composed of the sum of two functions whose relative interior has some overlap [1, 52, 53]. Furthermore, these two functionals (of which the objective is comprised) must tend to infinity as the norm of their inputs tend to infinity. On the other hand, Dykstra like proximal splitting works with less restrictive assumptions and relaxes the objective functional. In the Dykstra like case, the objective functional is composed of the sum of two functionals with a quadratic penalty for deviation from a provided reference signal. By relaxing the objective functional, Dykstra like splitting only requires that the underlying functionals which form the objective have some overlap [1, 52, 53, 51] (no requirement on the behavior of the norms of these function). A fascinating method that was introduced by Pustelnik [54] was that of parallel proximal operators for efficient computation. In this work, they consider the case when the objective is composed of more than just two functions [54, 1]. The authors were able able to demonstrate that the underlying objective can be minimized by utilizing a framework in which each proximal operator was computed independently of the other and then combined using a weighted linear combination. Inspired by computational efficiecy afforded by the parallelizable proximal method presented in [54], we extend one of our more costly computational methods to be parallizable (shown in Appendix A).

It is interesting to note that proximal algorithms and methods provide a generalized framework for most modern optimization. The well known $L_1$ shrinkage operator is exactly that: a proximal operator for the $L_1$ norm [20]. Methods such as ADMM which have made a resurgance in the recent past are also instantiations of proximal algorithms / methods. A good list functions and their corresponding proximity operators can be found in [1].

### 1.2.4 Frames

An excellent introduction to frames can be found in [55, 56] and the following is a brief summary of the work presented by Kovacevic and Chebira [55, 56]. The concept of frames evolved as a result of the direct limitations of bases. Given a signal composed of a finite number of frequencies, the fourier transform can be a efficient (sparse) representation of the underlying signal. However, if we were to add a range of discontinuities in the original signal, the fourier representation would no longer be sparse nor is it the most efficient representation. In such instances, it is best to have access to a range of representations to efficiently capture the underlying signal. Frames are formed by relaxing the underlying requirements for basis: linear independence of the constituent vectors that span a given space [55]. Based on the properties of the frame that is formed, a frame maybe classified as an equal norm frame, tight frame, equal norm tight frame, unit norm frame, parseval tight frames or equal norm parseval tight frames [55, 56]. All these definitions follow from the frame bounds which is explained below.

Formally, we can define a frame as follows. $\psi_k$ (where $k \in K$ belongs to an index set $K$) is considered a frame in a Hilbert space $\mathbb{H}$ if there exists bounds $C_1$ and $C_2$ such that $0 < C_1 \leq C_2 < \infty$, $\forall \vec{x} \in \mathbb{H}$, we can write

$$C_1\|x\|^2 \leq \sum_k |\langle \psi_k, \vec{x} \rangle|^2 \leq C_2\|x\|^2$$

Then a tight frame is one in which $C_1 = C_2$. A parseval tight frame is similar to a tight frame but adds the additional constraint that both frame bounds must be equal to 1. The classification of unit norm frames and equal norm frames are largely based on the energy of the underlying frame vectors. In instances when all the frame vectors $\psi_i$ have the same energy as measured by a valid norm, the frame is classified as a equal norm frame. Additional if all the frame vectors are constrained to have unit norm, then the frame is classified as a unit norm frame [55, 56].

In this work, we utilize the concept of tight frames which are in principle, the closest that frames get to sharing the properties of an orthonormal basis set. The benefit afforded by tight frames is that they are self dual i.e. $\Psi = \tilde{\Psi}$. We also have the property $\Psi\Psi^* = I$. Frames have a range of useful properties from reconstruction stability to resiliance to noise [55, 56]. Commonly used frames are the dual tree complex wavelet transform [57], double density dual tree complex wavelet transform [58] and the undecimated dual tree wavelet transform [59]. Tight frames can also be constructed by concatenating a series of orthonormal basis.

### 1.3 Novelty

We present a new algorithm for 'analysis' when $p < 1$ and explore its implementation for a variety of different applications. To the best of our knowledge, this is novel in both design and/or computational efficiency relative to previously published work [25, 26, 43, 60, 28, 29, 30, 31, 32, 33, 34, 35]. Our method leverages the benefit of tight frames, uses a computationally efficient architecture that is is significantly cheaper than existing convex / non convex regularized inverse problem solvers and can be trivially modified to examine either the synthesis or analysis prior. IAN can also enforce convex set membership constraints thereby generating a signal that lies within a convex set but is closest to the desired non convex $L_p$ ball. In addition, we are the first to demonstrate convergence of an analysis based non convex prior $((\|\cdot\|_p), 0 < p < 1)$ algorithm for linear inverse problems.

We apply IAN to ill-posed inverse problems such as single image super-resolution, undersampled medical image reconstruction and image denoising. In all these applications, we benchmark our results against state of the art algorithms in these domains and demonstrate IAN's ability to perform better than the state of the art. In order to handle image denoising, we extend IAN to handle a total variation regularizer (both isotropic and anisotropic). In addition, we demonstrate that for denoising, IAN can be used in the monte carlo based Stien's unbiased risk estimator for automated parameter tuning. Finally,

in instances when the parameters of the forward model are unknown for super-resolution (Ex.point spread function of a system) we demonstrate that IAN can be used with standard blind deconvolution splitting approaches [61] to recover the unknown signal and point spread function.

# CHAPTER 2

# METHODS

In this chapter, five main sections are presented. First, we explore our algorithmic approach to solving an optimization problem that has a non-convex analysis prior with a data fidelity term when the result must belong to a convex set (IAN). Second, we show how to extend the IAN framework by adding a total variation regularizer for gradient smoothness / sparsity. Third, we discuss SARA [25, 26], the state of the art analysis based non-convex (reweighted $L_1$) solver, that forms the core of our benchmark results. Fourth, we examine Chartrand's specific work on an approximation to the analysis $L_p$ objective function [31]. Since Chartrand's work in [31] focused on undersampled reconstruction, we benchmark IAN against the algorithm presented in [31] for undersampled recovery. Fifth and finally, we present the details of our numerical experiments for single image super-resolution, undersampled image reconstruction, image denoising and robust recovery (blind deconvolution).

## 2.1 IAN: Non-Convex Prior

IAN seeks to solve the following non-convex optimization problem

$$\min_{\vec{x}\in\mathbb{C}^n} \left( \frac{1}{2} \left\| \boldsymbol{A}\left(\vec{x}\right) - \vec{y} \right\|_2^2 + \lambda \left\| \boldsymbol{W}\left(\vec{x}\right) \right\|_p^p + \iota_C\left(\vec{x}\right) \right) \tag{2.1}$$

Above $p \in [0, 1]$, $\boldsymbol{A}(\cdot)$ is any linear operator, $\boldsymbol{W}(\cdot)$ is a tight frame s.t. $\boldsymbol{W}^*\left(\boldsymbol{W}\left(\cdot\right)\right) = I$ and, $\vec{y} \in \mathbb{C}^{m\times 1}$. The indicator of a convex set $\iota_C\left(\vec{x}\right)$ is optional and can be enforced flexibly based on application in question. In this work, when optimization over the real numbers $(\mathbb{R}^n)$, the set $C = \left\{\boldsymbol{W}\left(\vec{x}\right), \text{ s.t. } \vec{x} \succeq 0\right\}$ was used. For some applications the positivity constraint was not applicable and was removed (Ex. undersampled reconstruction over the set of complex numbers $(\mathbb{C}^n)$). IAN was inspired by the work on proximal dykstra-like

framework [1, 52, 53].

The Dykstra-like framework which forms the core of IAN solves the following general optimization problem. $\min_{\vec{x}\in\mathbb{C}^n}\left(f_1(\vec{x})+f_2(\vec{x})+\frac{1}{2}\|\vec{x}-\vec{r}\|_2^2\right)$ with the imposed feasibility condition that $\text{dom}(f_1(\vec{x}))\cap\text{dom}(f_2(\vec{x}))\neq\emptyset$ [1].Within the context of solving an analysis non-convex prior, $f_1(\vec{x})$ takes the form of the sparse analysis prior, $f_2(\vec{x})$ takes the form of an indicator function of a desired convex set, and $'r'$ is the frame coefficients of the intermediate signal obtained from the previous splitting step which in turn enforces data fidelity. Thus the sub optimization problem for IAN can be expressed as $\min_{\vec{x}\in\mathbb{C}^n}\left(\|\boldsymbol{W}(\vec{x})\|_p^p+\iota_C(\vec{x})+\frac{1}{2}\|\vec{x}-\vec{r}\|_2^2\right)$.

The norm constraint is applied through the use of a proximal shrinkage operator. Since the $L_p$ norm for $p<1$ does not have a closed form solution (except for special cases such as $p=0.5$), we use an iteratively computed shrinkage operator[2]. The shrinkage operator is the solution to the optimization problem : $\min_{\vec{z}\in\mathbb{C}^k}\|\vec{z}\|_p^p+\frac{1}{2}\|\vec{z}-\vec{v}\|_2^2$ where $0\leq p\leq 1$. The shrinkage operator can be mathematically summarized as

$$\boldsymbol{S}_{\lambda,p}(x_i)=\begin{cases}\text{sign}(x_i)\left(|x_i|-\hat{\tau}(x_i)\right) & |x_i|>\tau_{\lambda,p}\\ 0 & |x_i|\leq\tau_{\lambda,p}\end{cases} \tag{2.2}$$

where $0<\hat{\tau}(x_i)<\tau_{\lambda,p}$. The implementation of the Shrinkage operator is shown in Algorithm 1 (see [2] for more shrinkage algorithmic details).

The $t$ parameter defined in Algorithm 2-4 is the step size which is defined to be the inverse of the Lipschtiz constant. The Lipschitz constant can be exactly computed using the power iteration on the $\boldsymbol{A}^*(\boldsymbol{A}(\cdot))$ operator to extract the largest eigenvalue of the symmetric operator. The $\boldsymbol{S}_{\lambda,p}(\cdot)$ is the non convex shrinkage operator summarized in (5.4). For greater detail see [2]. $\boldsymbol{P}_C(\cdot)$ is the projection operator onto the convex set $C$ which solves the optimization problem $\min_{\vec{z}\in C}\|z-u\|_2^2$.

It must be highlighted that the versatility of IAN arises from step 13 of Algorithm

**Algorithm 1** Shrinkage Operator: $\vec{v} = \boldsymbol{S}_{\lambda,p}(\vec{u})$

$i \leftarrow 0$, $q \leftarrow 1-p$, $r \leftarrow 2-p$, $\vec{w} \leftarrow |\vec{u}|$, $\vec{s}^{\,(0)} \leftarrow \vec{0}$, $k \leftarrow 5$
$\tau \leftarrow (2\lambda q)^{\left(\frac{1}{r}\right)} + \lambda p\,(2\lambda q)^{\left(\frac{q}{r}\right)}$
$\iota \leftarrow \vec{w} > \tau$ ... *Logical Indices*
$\vec{s}_{\iota}^{\,(0)} = \vec{w}_{\iota}$
**repeat**
  $i \leftarrow i+1$
  $\vec{s}_{\iota}^{\,(i)} = \vec{w}_{\iota} - \lambda p \left(\vec{s}_{\iota}^{\,(i-1)}\right)^{(p-1)}$
**until** $i < k$
**return** $\vec{v} \leftarrow \text{sign}(\vec{u})\vec{s}^{\,(i)}$

**Algorithm 2** IAN ($y$, $p$, $\lambda$, $\boldsymbol{W}(\cdot)$, $\boldsymbol{W}^*(\cdot)$, $\boldsymbol{A}(\cdot)$, $\boldsymbol{A}^*(\cdot)$, $x^{(0)}$, $k$, $m$, $c$, $tol$, $tol_d$,$tol_g$, $t$)

$i \leftarrow 0$, $l \leftarrow 0$, $\hat{x}^{(l)} \leftarrow x^{(i)}$,
**repeat**
  $i \leftarrow i+1$
  **repeat**
    $\hat{x}^{(l+1)} \leftarrow \hat{x}^{(l)} - t\boldsymbol{A}^*\left(\boldsymbol{A}\left(\left(\hat{x}^{(l)}\right)\right) - y\right)$
    $l \leftarrow l+1$
  **until** $l > c$ OR $\|\hat{x}^{(l)} - \hat{x}^{(l-1)}\|_2 \leq tol_g$
  **return** $x^{(i+0.5)} \leftarrow \hat{x}^{(l)}$
  $r \leftarrow \boldsymbol{W}\left(x^{(i+0.5)}\right)$, $\tilde{x}^{(0)} \leftarrow r$, $s^{(0)} \leftarrow \boldsymbol{0}$, $q^{(0)} \leftarrow \boldsymbol{0}$, $j \leftarrow 0$
  **repeat**
    $u^{(j)} \leftarrow \boldsymbol{S}_{\lambda,p}\left(\tilde{x}^{(j)} + s^{(j)}\right)$
    $s^{(j+1)} \leftarrow \tilde{x}^{(j)} + s^{(j)} - u^{(j)}$
    $\tilde{x}^{(j+1)} \leftarrow \boldsymbol{P}_C\left(u^{(j)} + q^{(j)}\right)$
    $q^{(j+1)} \leftarrow u^{(j)} + q^{(j)} - \tilde{x}^{(j+1)}$
    $j \leftarrow j+1$
  **until** $j \geq m$ OR $||\tilde{x}^{(j)} - \tilde{x}^{(j-1)}||_2 \leq tol_d$
  **return** $x^{(i)} \leftarrow \boldsymbol{W}^*\left(\tilde{x}^{(j)}\right)$
**until** $i \geq (k)$ **or** $||x^{(i)} - x^{(i-1)}||_2 \leq tol$
**return** $x^{(i)}$

2. If a synthesis approach is desired, then set $C$ can be trivially modified to no longer require $x \in \text{span}(\boldsymbol{W}(\cdot))$. This change will alter the projection operator and will in fact further decrease the computational cost of the algorithm. The result of this change will be a solution that minimizes the synthesis objective function instead of the analysis framework shown in (2.4).

A tight frame was generated by using a redundant bank of real wavelets and / or dual tree complex wavelets [58, 62]). Shift invariance was enforced either through cycle spinning in the case of real wavelets or through the use of undecimated wavelet transforms / double density dual tree complex wavelet transforms [59, 58, 57, 62]. Rotational invariance can be enforced when desired using transformations such as the curvelet transform [63] and steerable pyramids. In order to accelerate convergence, interpolation based warm starts was used in the super-resolution application. Accelerated algorithms which solve $L_1$ regularized recovery problem were used as warm starts for the undersampled recovery case.

Synthesis based $Lp$ prior

In this context, it is important to disambiguate the benefits afforded by IAN's algorithmic framework versus the utilization of an $L_p$ analysis prior. To explore this in greater detail, we develop a test case algorithm for comparison which utilizes a simple forward-backward splitting approach to solve the synthesis problem

$$\min_{\vec{x}\in\mathbb{C}^k} \left( \frac{1}{2} \left\| \boldsymbol{A}\left(\boldsymbol{W}^*\left(\vec{x}\right)\right) - \vec{y} \right\|_2^2 + \lambda \left\| \vec{x} \right\|_p^p \right)$$

Algorithmicly, this can be implemented almost trivially as shown in Algorithm 3 below. The $prox$ operator used in the algorithm solves the sub-optimization problem $\min_{\vec{x}\in\mathbb{C}^k} \lambda\|\vec{x}\|_p^p + \|\vec{x}-\vec{v}\|^2$. The same tight frames and shrinkage operator used in IAN was provided to this algorithm for a fair comparison.

## 2.2 IAN with Total Variation (TV) Prior

A total variation (TV) prior seeks smooth the image while preserving high frequency edges. IAN with TV seeks to solve the following optimization problem.

$$\min_{\vec{x}\in\mathbb{C}^n}\left(\frac{1}{2}\left\|\boldsymbol{A}\left(\vec{x}\right)-\vec{y}\right\|_2^2+\lambda_1\left\|\boldsymbol{W}\left(\vec{x}\right)\right\|_p^p+\lambda_2\|\vec{x}\|_{TV}+\iota_C\left(\vec{x}\right)\right) \tag{2.3}$$

The TV operator seeks to minimize the horizontal and the vertical derivatives in an image. The manner in which these derivatives are combined define isotropic and anisotropic TV [64].

$$\|u\|_{TVIso}=\|\sqrt{|G_h(x)|^2+|G_v(x)|^2}\|_1$$
$$\|u\|_{TVAniso}=\|G_h(x)\|_1+\|G_v(x)\|_1$$

where $G_h$ and $G_v$ represent the discrete approximation to the horizontal and vertical gradient respectively. In this paper we consider isotropic TV. In order to solve the optimization problem specified in (2.3), we use a similar algorithmic framework as IAN .

In step 3 of algorithm 4, the $prox_{(\nabla+TV)}(\cdot,y,t,\lambda_2)$ operator refers to the proximal Chambolle Pock gradient TV projection [65]. This operator seeks to minimize $\min_{\vec{x}\in\mathbb{C}^n}\left(\frac{1}{2}\left\|\boldsymbol{A}\left(\vec{x}\right)-\vec{y}\right\|_2^2+\lambda_2\|\vec{x}\|_{TV}\right)$ by invoking a proximal mapping for the dual objective. Convergence for this operator is then measured by computing the primal - dual gap. The sets and other operators used in Algorithm 4 are identical to Algorithm 2 and have been previously defined.

Key to the utilization of the TV operator is the definition of the divergence operator that is essential for the proximal TV operator. In [65], the divergence operator is defined as .

**Algorithm 3** Forward-Backward Splitting ($y$, $p$, $\lambda$, $\boldsymbol{W}$, $\boldsymbol{W}^*$, $\boldsymbol{A}$, $\boldsymbol{A}^*$, $k$, $tol$,$t$)

$i \leftarrow 0$
**repeat**
  $x^{(i+0.5)} \leftarrow x^{(i)} - t\boldsymbol{W}\left(\boldsymbol{A}^*\left(\boldsymbol{A}\left(\boldsymbol{W}^*\left(x^{(i)}\right)\right) - y\right)\right)$
  $x^{(i)} \leftarrow prox_{\lambda,p}\left(x^{(i+0.5)}\right)$
  $i \leftarrow i + 1$
**until** $i \geq (k)$ **or** $||x^{(i)} - x^{(i-1)}||_2 \leq tol$
**return** $x^{(i)}$

**Algorithm 4** IAN with TV($\vec{y}$, $p$, $\lambda_1$, $\lambda_2$, $\boldsymbol{W}(\cdot)$, $\boldsymbol{W}^*(\cdot)$, $\boldsymbol{A}(\cdot)$, $\boldsymbol{A}^*(\cdot)$, $k$, $m$, $tol$, $tol_d$, $t$)

$i \leftarrow 0$
**repeat**
  $x^{(i+0.5)} \leftarrow prox_{(\nabla+TV)}(x^{(i)}, y, t, \lambda_2)$
  $r \leftarrow \boldsymbol{W}\left(x^{(i+0.5)}\right)$, $\tilde{x}^{(0)} \leftarrow r$, $s^{(0)} \leftarrow \mathbf{0}$, $q^{(0)} \leftarrow \mathbf{0}$, $j \leftarrow 0$
  **repeat**
    $u^{(j)} \leftarrow \boldsymbol{S}_{\lambda_1,p}\left(\tilde{x}^{(j)} + s^{(j)}\right)$
    $s^{(j+1)} \leftarrow \tilde{x}^{(j)} + s^{(j)} - u^{(j)}$
    $\tilde{x}^{(j+1)} \leftarrow \boldsymbol{P}_C\left(u^{(j)} + q^{(j)}\right)$
    $q^{(j+1)} \leftarrow u^{(j)} + q^{(j)} - \tilde{x}^{(j+1)}$
    $j \leftarrow j + 1$
  **until** $j \geq m$ OR $||\tilde{x}^{(j)} - \tilde{x}^{(j-1)}||_2 \leq tol_d$
  **return** $x^{(i)} \leftarrow \boldsymbol{W}^*\left(\tilde{x}^{(j)}\right)$
  $i \leftarrow i + 1$
**until** $i \geq (k)$ **or** $||x^{(i)} - x^{(i-1)}||_2 \leq tol$
**return** $x^{(i)}$

$$-\text{div}\begin{pmatrix}\Delta_h z\\ \Delta_v z\end{pmatrix} = \Delta_h z_{m-1,n} - \Delta_h z_{m,n} + \Delta_v z_{m,n-1} - \Delta_v z_{m,n}$$

where $m, n \in 1, 2, \ldots, K$, $z \in \mathbb{R}^{K,K}$ and the operators $\Delta_h$ and $\Delta_v$ are the horizontal and vertical difference operators (defined below) with reflective boundary conditions. The horizontal difference operator can be written as

$$\Delta_h(z) = \begin{cases} z_{m+1,n} - z_{m,n} & if \quad m < K \\ -z_{m,n} & if \quad m = K \end{cases}.$$

The vertical difference operator can equivalently be written as

$$\Delta_v(z) = \begin{cases} z_{m,n_1} - z_{m,n} & if \quad n < K \\ -z_{m,n} & if \quad n = K \end{cases}.$$

This type of TV operator (reflective / reflexive boundary condition) stands in contrast to the computationally efficient TV operator that can be implemented when periodic boundary conditions are assumed. When using periodic boundary conditions, the properties of the Fourier transform can be exploited to invoke the FFT for efficient computation [66]. For all the results presented in this work, a reflective boundary condition was assumed.

Parallel Architecture

When solving the combined $L_p$ and TV optimization problem the algorithm presented earlier is ideal for a single core architecture. When dealing with a parallelized framework, we found the following algorithm to work just as well as the serial proximal algorithm.

A parallel proximal Dykstra framework is used which allows for versatility in TV filter selection, choice of isotropic versus anisotropic TV, has theoretical guarantees [54, 1] and can be implemented in parallel.

The parallel Dykstra proximal framework [1, 54] was designed to solve problems of the form

$$\min_{\vec{x}\in\mathbb{C}^k}\left(\sum_{i=1}^{n}\omega_i f_i(\vec{x})+\frac{1}{2}\left\|\vec{x}-\vec{r}\right\|_2^2\right)$$

with the imposed feasibility condition that $\cap_i$ dom$(f_i(x)) \neq \emptyset$ and $\sum_i \omega_i = 1$. Within the context of solving an analysis non-convex prior, $f_1(\vec{x})$ is the indicator function for the convex set $C$ (defined in manuscript), $f_2(\vec{x})$ takes the form of a sparse analysis prior, $f_3(\vec{x})$ is the imposed TV regularizer and $\vec{r}$ represents the result of the previous fidelity enforcement. $\omega_i$ can be defined as the normalized regularization parameters. Thus the problem then takes the form

$$\min_{\vec{x}\in\mathbb{C}^n}\left(\iota_C\left(\vec{x}\right)+\omega_1\left\|\boldsymbol{W}\left(\vec{x}\right)\right\|_p^p+\omega_2\|\vec{x}\|_{TV}+\frac{1}{2}\|\vec{x}-\vec{r}\|_2^2\right)$$

The $prox_{TV}(\cdot)$ in the algorithm solves the sub-optimization problem $\min_{\vec{x}\in\mathbb{C}^n}\|\vec{x}-\vec{v}\|_2^2+\|\vec{x}\|_{TV}$. A proximal algorithm for TV is provided in [54] and was used here.

The TV operator can be enforced through custom edge filters (based on the needs of application under consideration) [54] . These custom filters must satisfy $tr(HV^T)=0$ where $H, V$ are the horizontal and vertical edge detection filters respectively (see [54]). Depending on the size of the edge detection filters used, $3\times3$ or $2\times2$ based block processing is necessary for this approach. In order to prevent artifacts along block boundaries, this procedure must be repeated for shifts of each block and with subsequent averaging of the results obtained from each stage. When access to a parallel framework is not available, the serialized algorithm presented earlier can be used.

### 2.3 SARA: Reweighted Analysis based $L_1$

Numerous published studies have demonstrated the ability of reweighted $L_1$ to enhance sparse recovery beyond that which is obtained by standard $L_1$ [49, 38, 67, 50]. This princi-

ple was extended into the analysis domain by [25, 26]. The authors dubbed their algorithm SARA and demonstrated its use for radio-interferometric imaging. SARA solves the following optimization problem

$$\min_{\vec{x}\in\mathbb{R}^n} \|\boldsymbol{D}\left(\boldsymbol{W}\left(\vec{x}\right)\right)\|_1 \text{ subject to } \|\boldsymbol{A}\left(\vec{x}\right)-\vec{y}\|_2 \leq \epsilon \ \ \& \ \ \vec{x} \succeq 0$$

(where $\boldsymbol{D}\left(\cdot\right)$ is a diagonal weighting operator, $\boldsymbol{W}\left(\cdot\right)$ is a frame operator and $\boldsymbol{A}\left(\cdot\right)$ is a linear operator). SARA is the state of the art non-convex solver and it is the algorithm against which we benchmark IAN for single image superresolution. To ensure a fair comparison, the original SARA solver was kept intact but the external operators ($\boldsymbol{A}\left(\cdot\right)$, $\boldsymbol{A}^*\left(\cdot\right)$, $\boldsymbol{W}\left(\cdot\right)$, $\boldsymbol{W}^*\left(\cdot\right)$) and tolerances were modified to the specific application [68]. As such, although SARA applied to single image super-resolution is a novel application of the original algorithm, it is not the focus of this work. Also, it must be noted that the parameters of the algorithm were only modified from their default setting if reconstruction accuracy was improved.

### 2.4 Chartrand : Analysis $L_p$

In order to solve the non convex $L_p$ analysis problem, Chartrand [31] uses the surrogate objective functional

$$\min_{\vec{x},\vec{v},\vec{w}} \sum_i \left(\psi(v_i)+\lambda\psi(w_i)\right) + \frac{\beta_D}{2}\|\vec{v}-\boldsymbol{D}\left(\vec{x}\right)\|_2^2 + \frac{\beta_W}{2}\|\vec{w}-\boldsymbol{W}(\vec{x})\|_2^2 + \frac{\mu}{2}\|\boldsymbol{A}(\vec{x})-\vec{y}\|_2^2$$

where $i$ iterates across all samples of a signal, $\boldsymbol{D}(\cdot)$ is the discrete TV operator, $\boldsymbol{W}(\cdot)$ is the basis operator, $\boldsymbol{A}(\cdot)$, $\vec{v},\vec{w}$ are splitting variables, $\psi(\cdot)$ is a closed form function, $\vec{y}$ is the observed data and $\beta_W$, $\beta_D$, $\mu$ are regularization constants. The algorithm uses a bregmann framework with a nested iterative structure. The algorithm itself lacks appropriate stopping criteria and requires external input on iteration limits (which is impractical for real world application). It must also be noted that this algorithm lacks any convergence guarantees.

However, given the promising numerical results presented in [31] and its $L_p$ formulation, we benchmark our undersampled recovery results with this non convex solver.

## 2.5 Experimental Details

The core of our numerical results examine three ill posed challenging inverse problems in imaging : single image super-resolution, undersampled image reconstruction and denoising. In this section, we provide details of the algorithms that we benchmarked our results against for each of these applications. In the interest of reproducible research, a representative parameter set which can be used to replicate our findings can be found in Appendix A. It must be noted that except for the custom phantom that was created for this study, medical images were downloaded from the publicly available database [70]. Fluroscopic images were provided by Siemens Corporate Technology, Princeton, NJ and the cardiac MR image was acquired in-house on a Siemens 3T Magnetom Trio (Malvern, PA) scanner with ECG gating (acquisition details provided below).

### 2.5.1 Single Image Super-resolution

For single image super-resolution, we motivate our application by examining medical images for which super-resolution would greatly aid clinical diagnosis. We specifically consider MRI image of cerebral tumor and angiographic images with fine capillary details. We also super-resolve guidewires in CT fluroscopic images which is of significant clinical interest to physicians. To generate a low resolution image for each of these applications, the images are blurred with a 3x3 gaussian kernel and then downsampled in the pixel domain by a factor of 2 for each dimension.

The reconstructed results are compared to standard interpolation based approaches (bilinear, bicubic, box kernel, Lanczos 2 kernel, Lanczos 3 kernel), the method of sparse mixing estimators (SME) [71], sparse representation based nonlocal autoregressive modelling (NARM) [72], spatially adaptive iterative singular value thresholding (SAIST) [73]

and the well known fast iterative shrinkage and thresholding algorithm (FISTA) [9]. In each of these instances, when code was made available on the author's website, parameters were tuned only if they provided a better reconstruction than the default parameter setting. In instances where the code was not publicly available, we implemented the algorithm based on the authors' published paper. To quantify the accuracy of image recovery, we used the peak signal to noise ratio (defined below) and the structure similarity metric (SSIM) as defined in [74].

$$PSNR(x, \hat{x}) = (20 \log_{10} \max(x)) + (10 \log_{10}(MSE(x, \hat{x}))$$

Where $MSE$: mean square error, $x$ is the reference signal and $\hat{x}$ is the recovered signal.

### 2.5.2 Undersampled Medical Image Reconstruction

Undersampling has garnered much interest in signal acquisition over the past decade since seminal work [5, 7, 11] demonstrated that signals could be recovered with far fewer measurements than that dictated by the Nyquist rate. In medical imaging, undersampled acquisition results in faster scan times which in turn mitigates motion artifacts. Motion artifacts are a significant challenge in medical imaging and are the cause of image streaks and ghosting artifacts. Patient motion (internal and external) necessitates image registration between long acquisitions which further reduces in the interpretability of the data. In this section, we demonstrate IAN's ability to reconstruct undersampled pathological and regular MRI and CT medical images with greater fidelity than both state of the art convex and non convex methods. For all the undersampling results presented in this paper, we use the undecimated dual tree complex wavelet transform to ensure some degree of directional and rotational invariance [59]. In MRI undersampling, true random sampling results in an inefficient use of hardware gradients. True random sampling (as defined in the compressive sensing literature [5]) might even prolong acquisition times instead of reducing it. Thus,

undersampling in MRI for a 2D acquisition is performed along the phase encode direction in k-space. This ensures that gradient slew rates do not become a temporal limiting factor. In the discrete domain, this is equivalent to undersampling along one dimension of a 2D Fourier transform. Given the concentration of signal near the center of k-space, phase encodes are sampled with greater likelihood near the center of k-space relative to the fringes of k-space. For all the results presented in this paper, less than $30\%$ of k-space was sampled (i.e. undersampling $\geq 70\%$) resulting in an undersampling factor $(R \approx 4)$. Specific undersampling factors can be found in Table 4.2. It must be noted that larger degree of undersampling (without loss in image quality) is possible provided non cartesian (radial/ spiral) sampling is used. We use cartesian sampling to demonstrate that even with simple cartesian undersampling, IAN performs better than state of the art convex and non convex methods. Details of the MRI acquisition (for the reconstruction shown) is as follows: Data was acquired on a Siemens 3T Tim Trio using EKG gating for a total of 7 cardiac phases. An echo time of 1.43msec with a repetition time of 81msec was used. The data was acquired with 10 averages and a slice thickness of 5.5 mm using a flip angle of $40^o$. The in plane resolution was 1.6mm isotropic with a matrix size of 176 x 130. A body coil with 6 channels was used for acquisition with a pixel bandwidth of 980 Hz.

For CT, undersampling takes the form of restricting the number of projection views obtained. In order to obtain the projection operator, each column of the forward operator contains the radon projection of an indicator basis function of an image across all desired projection angles. Given that adjacent projections are highly correlated, the projection operator is rarely full rank. We show, that even when very few views are used, IAN reconstructs undersampled CT images with greatest fidelity relative to other convex, non convex and standard non iterative reconstruction methods (filtered back projection). Since total variation regularizers are commonly used in CT image reconstruction [65, 31], we provide results for IAN with TV for undersampled CT reconstruction as well. We quantify reconstruction accuracy using the peak signal to noise ratio metric defined in the previous

section.

### 2.5.3 Image Denoising

Medical images are noisy given the inability to control factors such as thermal noise, electromagnetic interference and other non laboratory conditions. In order to combat this, we use IAN to denoise ground truth MRI and CT Fluroscopic images with the explicit goal of aiding clinical diagnosis.

The denoised results are bench marked against the state of the art block matching and 3D filtering algorithm [75], fast gradient projection method [10] and the recent patch based optimal Wiener filtering [76]. When code was publicly available, parameters were only tuned if they resulted in a better reconstruction than the default setting. When code was not available, we implemented the method based on the author's published report. For algorithms that required oracle information about the noise variance, a portion of the input image devoid of signal was used to estimate the noise variance.

In most denoising scenarios, since the ground truth is being denoised, standard reference based metrics cannot be used. As such, we use the metric (IQM) outlined in [77].

### 2.5.4 Robust Recovery and Blind Deconvolution

As an extension, we also consider the case when the forward model parameters are unknown. The optimization problem is extremely ill-posed and for single image super-resolution, takes the form

$$\min_{\vec{x}\in\mathbb{C}^n,\boldsymbol{B}} \left( \frac{1}{2} \left\| \boldsymbol{D}\left(\boldsymbol{B}\left(\vec{x}\right)\right) - \vec{y} \right\|_2^2 + \lambda \left\| \boldsymbol{W}\left(\vec{x}\right) \right\|_p^p + \iota_{C_1}\left(\vec{x}\right) + \iota_{C_2}\left(\boldsymbol{B}\right) \right) \tag{2.4}$$

where the operator $\boldsymbol{B}$ is the unknown blur operator and $\boldsymbol{D}$ is the known downsampling operator. The additional set constraint $\iota_{C_2}(\boldsymbol{B})$ is a prior that can be imposed on the recovered blurring operator (For ex. symmetric blur kernel).

For this type of blind deconvolution problem, IAN can be used within a standard frame-

work [61] to recover the unknown point spread function (blurring kernel) and the signal in question. We use a standard splitting framework to alternatively update each unknown. This type of alternating minimization is made possible by exploiting the commutativity of convolution (i.e. $\vec{y} = DBX = DXB$).

It must be noted that step 3 (Algorithm 6) can be skipped during the first iteration, provided a warm start is made available. In the case of single image super-resolution, this might take the form of an interpolation based warm start.

Blind deconvolution is presented here only as a proof of concept extension to demonstrate IAN's applicability even when the parameters of the forward model are not completely known. There are an entire suite of state of the art blind deconvolution methods that stand on firm mathematical footing within the convex framework [78, 61]. Exploring the non convex extension of IAN into the blind deconvolution realm presented an interesting academic exercise that is explored briefly as an outworking of scientific curiosity.

**Algorithm 5** IAN with TV: Parallel Dykstra ($y$, $p$, $\lambda_1$, $\lambda_2$, $\boldsymbol{W}$, $\boldsymbol{W}^*$, $\boldsymbol{A}$, $\boldsymbol{A}^*$, $k$, $m$, $tol$, $tol_d$, $t$)

$i \leftarrow 0$
**repeat**
  $x^{(i+0.5)} \leftarrow x^{(i)} - t\boldsymbol{A}^* \left(\boldsymbol{A}x^{(i)} - y\right)$
  $r \leftarrow \boldsymbol{W}\left(x^{(i+0.5)}\right)$, $\tilde{x}^{(0)} \leftarrow r$, $q_1^{(0)} \leftarrow \tilde{x}^{(0)}$, $q_2^{(0)} \leftarrow \tilde{x}^{(0)}$, $j \leftarrow 0$
  **repeat**
    $s_1^{(j)} \leftarrow \boldsymbol{P}_C\left(\boldsymbol{S}_{\lambda,p}\left(q_1^{(j)}\right)\right)$
    $s_2^{(j)} \leftarrow \boldsymbol{P}_C\left(\boldsymbol{W}\left(prox_{TV}\left(\boldsymbol{W}^*\left(q_2^{(j)}\right)\right)\right)\right)$
    $\tilde{x}^{(j+1)} \leftarrow \sum_i^2 \omega_i q_i$
    $q_1^{(j+1)} \leftarrow \tilde{x}^{(j+1)} + q_1^{(j)} - s_1^{(j)}$
    $q_2^{(j+1)} \leftarrow \tilde{x}^{(j+1)} + q_2^{(j)} - s_2^{(j)}$
    $j \leftarrow j + 1$
  **until** $j \geq m$ OR $||\tilde{x}^{(j)} - \tilde{x}^{(j-1)}||_2 \leq tol_d$
  **return** $x^{(i)} \leftarrow \boldsymbol{W}^*\left(\tilde{x}^{(j)}\right)$
  $i \leftarrow i + 1$
**until** $i \geq (k)$ **or** $||x^{(i)} - x^{(i-1)}||_2 \leq tol$
**return** $x^{(i)}$

**Algorithm 6** Blind Deconvolution Pseudocode ($D$)

$\tilde{A} \leftarrow D$
**repeat**
  $X \leftarrow$ IAN / IAN with TV ($\tilde{A}$)
  $B \leftarrow$ given $y = DXB$, solve for B
  $\tilde{A} \leftarrow DB$
**until** Convergence
**return** $X$, $B$

# CHAPTER 3
# THEORETICAL RESULTS

## 3.1 Summary and Goal

In this section, we demonstrate that successive IAN algorithmic iterates are guaranteed to converge to a local minimum when not initialized at a fixed point. In order to do this, we draw on theoretical work on operators defined over non convex sets [79] and utilize techniques from optimization transfer [80, 81, 20, 82]. The convergence results demonstrated in [79] apply to operators which are asymptotically nonexpansive (defined below) and are asymptotically regular (defined below). We demonstrate that the operators used in IAN have both these properties and are thus guaranteed to converge to a fixed point. Finally, we demonstrate that a fixed point for the system is a local minimum.

The work we present differs from the standard approaches employed in demonstrating convergence to fixed points for algorithms of this type. Standard approaches require the operators to be either strictly nonexpansive or nonexpansive (see [51, 83, 20, 82, 84, 85]). Convergence with asymptotically nonexpansive operator is more general and encompasses convergence of strictly nonexpansive or nonexpansive operators.

## 3.2 Notation, Operator Definitions and Important Lemmas

Before outlining the main theorem, we first introduce succinct notation in order to write successive iterations as the application of a single operator $\boldsymbol{Z}_{\lambda,p}(\cdot)$. It is the properties of this operator which in turn will be used to demonstrate convergence. Let successive iterations of IAN be written as

$$\vec{x}^{\,(n)} = \boldsymbol{Z}_{\lambda,p}^{n}\left(\vec{x}^{\,(0)}\right). \tag{3.1}$$

Expanding this operator, we can write

$$\boldsymbol{Z}_{\lambda,p}(\vec{x}) = \boldsymbol{D}_{\lambda,p}\left(\vec{x} - \left(\boldsymbol{A}^{*}\left(\boldsymbol{A}\left(\vec{x}\right) - \vec{y}\right)\right)\right) \tag{3.2}$$

where $\boldsymbol{D}_{\lambda,p}\left(\cdot\right)$ is the Dykstra like proximal projection which enforces the $L_p$ norm and projection onto the desired convex set $C$. We will assume $\|\boldsymbol{A}\|_2 \leq 1$. If this is not true, the singular values of $\boldsymbol{A}$ can be rescaled or the parameter $t$ in Algorithm 2 and 3 can be adjusted accordingly. Finally, on cursory examination of Algorithm 2, it becomes clear that a single iteration of the Dykstra like proximal projection operator $\boldsymbol{D}_{\lambda,p}\left(\cdot\right)$ is implemented through the use of the composition of operators listed below. Thus, the action of the operator $\boldsymbol{D}_{\lambda,p}\left(\cdot\right)$ can be succinctly written as

$$\boldsymbol{D}_{\lambda,p}\left(\vec{x}\right) = \boldsymbol{P}_{C}\left(\boldsymbol{S}_{\lambda,p}\left(\vec{x}\right)\right) \tag{3.3}$$

The operator $\boldsymbol{S}_{\lambda,p}(\cdot)$ is algorithmically defined in [2] and is summarized for each component $i$ in (5.4)

**Definition** : An operator $\boldsymbol{T}\left(\cdot\right)$ is defined to be a contraction over a Hilbert space $\mathbb{H}$, iff $\forall u \in \mathbb{H}$, $\|\boldsymbol{T}\left(\vec{u}\right)\| < \|u\|$.

**Definition** : An operator $\boldsymbol{T}\left(\cdot\right)$ is nonexpansive over a Hilbert space $\mathbb{H}$, iff $\forall u, v \in \mathbb{H}$, $\|\boldsymbol{T}\left(\vec{u}\right) - \boldsymbol{T}\left(\vec{v}\right)\| \leq \|\vec{u} - \vec{v}\|$. See [83] for more details.

**Definition** : An operator $\boldsymbol{T}\left(\cdot\right)$ is asymptotically nonexpansive over a subset $Q$ of a Hilbert space $\mathbb{H}$, iff $\forall u \in Q$, $\limsup_{n\to\infty} \sup_{v\in Q}(\|\boldsymbol{T}^{n}\left(\vec{u}\right) - \boldsymbol{T}^{n}\left(\vec{v}\right)\| - \|\vec{u} - \vec{v}\| \leq 0)$. See [79] for more details.

A cursory examination of the above definitions will demonstrate that a contraction mapping is a specific instantiation of a nonexpansive mapping where $\vec{v} = \vec{0}$. It is trivial to see that all nonexpansive operators are asymptotically nonexpansive. We will show in Lemma

3 that a contraction operator is asymptotically nonexpansive.

**Lemma 1.** *For vectors in a given Hilbert space $\mathbb{H}$, a projection onto a convex set $P_C(\cdot)$ is nonexpansive i.e. $\|\boldsymbol{P}_C(\vec{u}) - \boldsymbol{P}_C(\vec{v})\| \leq \|\vec{u} - \vec{v}\| \ \ \forall u, v \in \mathbb{H}$*

*Proof.* This is a well established fact in convex analysis. See proposition 4.8 in [85] □

**Lemma 2.** *Composition of an asymptotically nonexpansive operator with a nonexpansive operator results in an operator that is also asymptotically nonexpansive i.e. $\forall u, v \in Q$ $\limsup_{n\to\infty} \sup_{v\in Q} \left( \|\boldsymbol{P}_{1,2}^n(\vec{u}) - \boldsymbol{P}_{1,2}^n(\vec{v})\| - \|\vec{u} - \vec{v}\| \leq 0 \right)$ where $\boldsymbol{P}_{1,2}(\vec{u}) = \boldsymbol{P}_1(\boldsymbol{P}_2(\vec{u}))$, $\boldsymbol{P}_2(\cdot)$ is asymptotically nonexpansive and $\boldsymbol{P}_1(\cdot)$ is nonexpansive.*

*Proof.* It is sufficient to show

$$\|\boldsymbol{P}_{1,2}^n(\vec{u}) - \boldsymbol{P}_{1,2}^n(\vec{v})\| \leq \|u - v\| \ \ \forall u, v \in \mathbb{Q}, \ n \to \infty$$

where $\boldsymbol{P}_{1,2}(\vec{u}) = \boldsymbol{P}_1(\boldsymbol{P}_2(\vec{u}))$, $\boldsymbol{P}_1(\cdot)$ is nonexpansive and $\boldsymbol{P}_2(\cdot)$ is asymptotically nonexpansive.

$$\begin{aligned}
&\|\boldsymbol{P}_{1,2}^n(\vec{u}) - \boldsymbol{P}_{1,2}^n(\vec{v})\| \\
&\qquad = \|\boldsymbol{P}_{1,2}^{n-1}(\boldsymbol{P}_1(\boldsymbol{P}_2(\vec{u}))) - \boldsymbol{P}_{1,2}^{n-1}(\boldsymbol{P}_1(\boldsymbol{P}_2(\vec{v})))\| \\
&\qquad \leq \|\boldsymbol{P}_{1,2}^{n-2}\left(\boldsymbol{P}_2^2(\vec{u})\right) - \boldsymbol{P}_{1,2}^{n-2}\left(\boldsymbol{P}_2^2(\vec{v})\right)\| \\
&\qquad\qquad\qquad \vdots \\
&\qquad \leq \|\boldsymbol{P}_2^n(\vec{u}) - \boldsymbol{P}_2^n(\vec{v})\| \\
&\qquad \leq \|u - v\|
\end{aligned}$$

□

With these basic Lemmas, definition and notation, we can begin to examine convergence.

### 3.3 Establishing convergence using Bruck's theorem

**Theorem 3.3.1.** *[79] Let $\boldsymbol{T}(\cdot) : \mathbb{Q} \to \mathbb{Q}$ be a mapping where $\mathbb{Q} \subset \mathbb{H}$ and $\mathbb{H}$ is a Hilbert space. Let a series be defined as $\vec{u}^{\,(n)} = \boldsymbol{T}^n\left(\vec{u}^{(0)}\right)$ then if the mapping $\boldsymbol{T}(\cdot)$ is* [1]

- *Asymptotically nonexpansive i.e.* $\limsup_{n\to\infty} \sup_{v\in Q} \left(\|\boldsymbol{T}^n(\vec{u}) - \boldsymbol{T}^n(\vec{v})\| - \|\vec{u} - \vec{v}\| \leq 0\right) \ \forall \vec{u} \in \mathbb{Q}$
- *Asymptotically regular i.e.* $\|\boldsymbol{T}^{(n+1)}(\vec{u}) - \boldsymbol{T}^{(n)}(\vec{v})\| \to 0$ *as* $n \to \infty$

*then the series $\{u^{(n)}\}$ converges to a fixed point of $\boldsymbol{T}(\cdot)$ as $n \to \infty$.*

**Lemma 3.** *The shrinkage operator $(\boldsymbol{S}_{\lambda,p}(\cdot))$ defined in (5.4) is asymptotically nonexpansive.*

*Proof.* In order to demonstrate asymptotic convergence of the shrinkage operator $\boldsymbol{S}_{\lambda,p}(\cdot)$, it is sufficient to show that

$$\|\boldsymbol{S}^n(\vec{u}) - \boldsymbol{S}^n(\vec{v})\| \leq \|u - v\| \ \ \forall u, v \in \mathbb{Q}, \ n \to \infty$$

From the definition of the shrinkage operator shown in (5.4), it is evident that the operator $\boldsymbol{S}_{\lambda,p}(\cdot)$ is a contraction i.e. $\|\boldsymbol{S}_{\lambda,p}(\vec{u})\| < \|u\| \ \ \forall u$. Then we have $\|\boldsymbol{S}^n_{\lambda,p}(\vec{u})\| \to 0, \ n \to \infty$. From this, we have $\|\boldsymbol{S}^n(\vec{u}) - \boldsymbol{S}^n(\vec{v})\| \to 0, \ n \to \infty$ □

Alternatively, this can also be shown by bounding each term.

*Proof.* We need to demonstrate that the shrinkage operator $\boldsymbol{S}_{\lambda,p}(\cdot)$, satisfies

$$\limsup_{n\to\infty} \sup_{v\in Q} \left( \underbrace{\|\boldsymbol{S}^n(\vec{u}) - \boldsymbol{S}^n(\vec{v})\|}_{\boldsymbol{E}^n(\vec{u},\vec{v})} - \|\vec{u} - \vec{v}\| \leq 0 \right) \forall \vec{u} \in \mathbb{Q}$$

[1] This theorem requires that the operator be defined over a Banach space with the uniform Opial property where the topology is Hausdorff. Since these conditions are satisfied by the ambient space under consideration Ex. $\mathbb{R}^N$, it is not listed as part of the theorem for clarity of expression. See [79] for more details

We approach this by demonstrating that $\boldsymbol{E}^n(\vec{u},\vec{v}) \rightarrow 0$ as $n \rightarrow \infty$. This in turn establishes the shrinkage operator $\boldsymbol{S}_{\lambda,p}(\cdot)$ as asymptotically nonexpansive $\forall u, v \in \mathbb{Q}$. Since the shrinkage operator is component wise separable, it is sufficient to demonstrate that $\boldsymbol{E}^n(u_i, v_i) \rightarrow 0$ for an arbitrary vector index $i$ as $n \rightarrow \infty$. Consider the form of the shrinkage operator shown in (9): at each iteration the magnitude of a component is either reduced or thresholded to zero. Let $\tau^*$ to be the minimum non zero shrinkage experienced by either $u_i$ and $v_i$ for any two successive applications of the shrinkage operator upto $n$. Let us define the operator $\widehat{\boldsymbol{S}}^n(z) = \text{sign}(z)\Phi\left(|z| - n\tau^*\right)$ where

$$\Phi(z) = \begin{cases} z & z > 0 \\ 0 & else \end{cases}$$

Then it is easy to see that $|\widehat{\boldsymbol{S}}(u_i)| \geq |\boldsymbol{S}(u_i)|$ and $|\widehat{\boldsymbol{S}}(v_i)| \geq |\boldsymbol{S}(v_i)|$. Then if we define $\widehat{\boldsymbol{E}}^n(u_i, v_i) = |\widehat{\boldsymbol{S}}^n(u_i) - \widehat{\boldsymbol{S}}^n(v_i)|$, we have $\widehat{\boldsymbol{E}}^n(u_i, v_i) \geq \boldsymbol{E}^n(u_i, v_i) \geq 0$. From the definition of the operator $\widehat{\boldsymbol{S}}^n(z)$, it is trivial to see that $\widehat{\boldsymbol{S}}^n(z) \rightarrow 0$ as $n \rightarrow \infty$. Thus we have $\widehat{\boldsymbol{E}}^n(u_i, v_i) \rightarrow 0$ as $n \rightarrow \infty$. This establishes $\boldsymbol{E}^n(u_i, v_i) \rightarrow 0$ as $n \rightarrow 0$ thereby demonstrating that $\boldsymbol{S}^n(\cdot)$ is asymptotically non expansive. □

**Lemma 4.** *The Dykstra like proximal projection operator $(\boldsymbol{D}_{\lambda,p}(\cdot))$ defined in (3.3) is asymptotically nonexpansive.*

*Proof.* The Dykstra like proximal projection operator $(\boldsymbol{D}_{\lambda,p}(\cdot))$ is defined as the composition of a series of asymptotically nonexpansive and nonexpansive operators (3.3). By Lemma (2), the operator $(\boldsymbol{D}_{\lambda,p}(\cdot))$ is asymptotically nonexpansive. □

**Lemma 5.** *The composite operator $(\boldsymbol{Z}_{\lambda,p}(\cdot))$ defined in (3.2) is asymptotically nonexpansive.*

*Proof.* For asymptotic nonexpansiveness, it is sufficient to show that $\|\boldsymbol{Z}^n_{\lambda,p}(\vec{u}) - \boldsymbol{Z}^n_{\lambda,p}(\vec{v})\| \leq$

$\|\vec{u} - \vec{v}\|$ as $n \to \infty$.

$$
\begin{aligned}
&\|\boldsymbol{Z}^n_{\lambda,p}(\vec{u}) - \boldsymbol{Z}^n_{\lambda,p}(\vec{v})\| \\
&= \left\|\boldsymbol{D}^n_{\lambda,p}\left(\vec{u} - \boldsymbol{A}^*\left(\boldsymbol{A}\left(\vec{u}\right) - \vec{y}\right)\right) - \boldsymbol{D}^n_{\lambda,p}\left(\vec{v} - \boldsymbol{A}^*\left(\boldsymbol{A}\left(\vec{v}\right) - \vec{y}\right)\right)\right\| \\
&\leq \|\vec{u} - \boldsymbol{A}^*(\boldsymbol{A}\vec{u} - \vec{y}) - \vec{v} + \boldsymbol{A}^*(\boldsymbol{A}\vec{v} - \vec{y})\| \\
&= \|(\boldsymbol{I} - \boldsymbol{A}^*\boldsymbol{A})\vec{u} - (\boldsymbol{I} + \boldsymbol{A}^*\boldsymbol{A})\vec{v}\| \\
&\leq \|\boldsymbol{I} - \boldsymbol{A}^*\boldsymbol{A}\|\|\vec{u} - \vec{v}\| \\
&\leq \|\vec{u} - \vec{v}\|
\end{aligned}
$$

□

**Lemma 6.** *The composite operator* $\left(\boldsymbol{Z}_{\lambda,p}\left(\cdot\right)\right)$ *is asymptotically regular.*

*Proof.* The proof for this is nearly identical to that found in [80, 86, 20, 81, 82]. It is shown here for completeness only.

In order to establish this, we will utilize a technique from optimization transfer : the use of a surrogate functional [80, 86, 20, 81, 82]. The surrogate functional defined as $g(\vec{x}, \vec{v}) = f(\vec{x}) + \|\boldsymbol{A}(\vec{x} - \vec{v})\|_2^2 + \|\vec{x} - \vec{v}\|_2^2$ (where $f(\vec{x}) = \lambda\|\boldsymbol{W}\left(\vec{x}\right)\|_p^p + \frac{1}{2}\|\boldsymbol{A}\left(\vec{x}\right) - \vec{y}\|_2^2 + \iota_C(\vec{x})$ has the properties $f(\vec{x}) = g(\vec{x}, \vec{x})$ and $f(\vec{x}) \leq g(\vec{x}, \vec{v})\ \forall \vec{x}, \vec{v} \in \mathbb{H}$. The property $f(\vec{x}) \leq g(\vec{x}, \vec{v})$ is demonstrated below.

$$
\begin{aligned}
&g(\vec{x}, \vec{v}) \\
&= \lambda\|\boldsymbol{W}\left(\vec{x}\right)\|_p^p + \frac{1}{2}\|\boldsymbol{A}\left(\vec{x}\right) - \vec{y}\|_2^2 + \iota_C(\vec{x}) - \|\boldsymbol{A}\left(\vec{x}\right) - \boldsymbol{A}\left(\vec{v}\right)\|_2^2 + \|\vec{x} - \vec{v}\|_2^2 \\
&= \lambda\|\boldsymbol{W}\left(\vec{x}\right)\|_p^p + \frac{1}{2}\|\boldsymbol{A}\left(\vec{x}\right) - \vec{y}\|_2^2 + \iota_C(\vec{x}) - \|\boldsymbol{A}(\vec{x} - \vec{v})\|_2^2 + \|\vec{x} - \vec{v}\|_2^2 \\
&\geq \lambda\|\boldsymbol{W}\left(\vec{x}\right)\|_p^p + \frac{1}{2}\|\boldsymbol{A}\left(\vec{x}\right) - \vec{y}\|_2^2 + \iota_C(\vec{x}) - \|\boldsymbol{A}\|_2^2\|(\vec{x} - \vec{v})\|_2^2 + \|\vec{x} - \vec{v}\|_2^2 \\
&= \lambda\|\boldsymbol{W}\left(\vec{x}\right)\|_p + \frac{1}{2}\|\boldsymbol{A}\left(\vec{x}\right) - \vec{y}\|_2^2 + \iota_C(\vec{x}) + \|(\vec{x} - \vec{v})\|_2^2(1 - \|\boldsymbol{A}\|_2^2) \\
&\geq f(\vec{x})
\end{aligned}
$$

The algorithmic structure in (3.2) solves the optimization problem $\vec{x}^{\,(j+1)} = \min_{\vec{x}} g(\vec{x}, \vec{x}^{\,(j)})$ (see [81, 20, 82, 80]).

Next we show that the series $f\left(\vec{x}^{\,(j)}\right)$ and $g\left(\vec{x}^{\,(j+1)}, \vec{x}^{\,(j)}\right)$ are both non increasing. Let $\boldsymbol{Q} = \sqrt{I - \boldsymbol{A}^*\boldsymbol{A}}$. Then we can write

$$\begin{aligned}
& f\left(\vec{x}^{\,(j+1)}\right) + \left\|\boldsymbol{Q}\left(\vec{x}^{\,(j+1)} - \vec{x}^{\,(j)}\right)\right\|_2^2 \\
&= f\left(\vec{x}^{(j+1)}\right) - \left\|\boldsymbol{A}\vec{x}^{\,(j+1)} - \boldsymbol{A}\vec{x}^{\,(j)}\right\|_2^2 + \left\|\vec{x}^{\,(j+1)} - \vec{x}^{\,(j)}\right\|_2^2 \\
&= g\left(\vec{x}^{\,(j+1)}, \vec{x}^{\,(j)}\right) \\
&\leq g\left(\vec{x}^{\,(j)}, \vec{x}^{\,(j)}\right) = f\left(\vec{x}^{\,(j)}\right) \qquad (3.4)
\end{aligned}$$

This gives us $f\left(\vec{x}^{\,(j+1)}\right) \leq f\left(\vec{x}^{\,(j)}\right)$ which establishes the convergences of the series defined by $f\left(\vec{x}^{\,(j)}\right)$. We also have the relation

$$\begin{aligned}
g\left(\vec{x}^{\,(j+2)}, \vec{x}^{\,(j+1)}\right) &\leq f\left(\vec{x}^{\,(j+1)}\right) \\
&\leq \underbrace{f\left(\vec{x}^{\,(j+1)}\right) + \left\|\boldsymbol{Q}\left(\vec{x}^{\,(j+1)} - \vec{x}^{\,(j)}\right)\right\|_2^2}_{g\left(\vec{x}^{\,(j+1)}, \vec{x}^{\,(j)}\right)}
\end{aligned}$$

This gives us $g\left(\vec{x}^{\,(j+2)}, \vec{x}^{\,(j+1)}\right) \leq g\left(\vec{x}^{\,(j+1)}, \vec{x}^{\,(j)}\right)$ which establishes the convergences of the series defined by $g\left(\vec{x}^{\,(j+1)}, \vec{x}^{\,(j)}\right)$.

With this, we can now show that mapping $\boldsymbol{Z}_{\lambda,p}$ is asymptotically regular i.e $\|\boldsymbol{Z}_{\lambda,p}^{(n+1)}(\vec{x}) - \boldsymbol{Z}_{\lambda,p}^{(n)}(\vec{x})\| \to 0$ as $n \to \infty$ From (3.4) we know that $f\left(\vec{x}^{\,(j+1)}\right) + \left\|\boldsymbol{Q}\left(\vec{x}^{\,(j+1)} - \vec{x}^{\,(j)}\right)\right\|_2^2 = g\left(\vec{x}^{\,(j+1)}, \vec{x}^{\,(j)}\right)$. Since $\|\boldsymbol{A}\| < 1$, if we set $s \leq \|(\boldsymbol{Q}^*\boldsymbol{Q})^{-1}\|_2$ (lower bound on the smallest singular value of $\boldsymbol{Q}^*\boldsymbol{Q}$), then we can write

$$\sum_{j=0}^{n} \left\|\vec{x}^{\,(j+1)} - \vec{x}^{\,(j)}\right\|^2 \leq \frac{1}{s} \sum_{j=0}^{n} \left\|\boldsymbol{Q}\left(\vec{x}^{\,(j+1)} - \vec{x}^{\,(j)}\right)\right\|^2 \qquad (3.5)$$

By definition, we have $\vec{x}^{(j+1)} = \min_{\vec{x}} g(\vec{x}, \vec{x}^{\,(j)})$. We have already shown $g(\vec{x}^{\,(j+1)}, x^{\,(j)}) \leq g(\vec{x}^{\,(j)}, \vec{x}^{\,(j)}) = f(\vec{x}^{\,(j)})$. Then invoking (3.4) and the established proposition that the se-

ries $f\left(\vec{x}^{\,(j)}\right)$ and $g\left(\vec{x}^{\,(j+1)}, \vec{x}^{\,(j)}\right)$ are both non increasing, we can write $g(\vec{x}^{\,(j+1)}, x^{\,(j)}) = f(\vec{x}^{\,(j+1)}) + \boldsymbol{Q}\|\vec{x}^{\,(j+1)} - \vec{x}^{\,(j)}\|_2^2 \leq f(\vec{x}^{(j)})$. This then gives us the relation $\boldsymbol{Q}\|\vec{x}^{(j+1)} - \vec{x}^{(j)}\|_2^2 \leq f(\vec{x}^{(j)}) - f(\vec{x}^{(j+1)})$. Now summing across iterations, we get

$$\begin{aligned}\sum_{j=0}^{n} \boldsymbol{Q}\left\|\vec{x}^{\,(j+1)} - x^{\,(j)}\right\|_2^2 &\leq \sum_{j=0}^{n} f\left(\vec{x}^{\,(j)}\right) - f\left(\vec{x}^{\,(j+1)}\right) \\ &= f\left(\vec{x}^{\,(0)}\right) - f\left(\vec{x}^{\,(n)}\right) \\ &\leq f\left(\vec{x}^{\,(0)}\right) \end{aligned} \tag{3.6}$$

Now combining (3.5) and (3.6) we get

$$\sum_{j=0}^{n} \left\|\vec{x}^{\,(j+1)} - \vec{x}^{\,(j)}\right\|^2 \leq \left(\frac{1}{s}\right) f\left(\vec{x}^{\,(0)}\right)$$

This proves that the infinite sequence $\sum_{j=0}^{n} \left\|\vec{x}^{\,(j+1)} - \vec{x}^{\,(j)}\right\|^2$ is uniformly convergent. This implies that the mapping $\boldsymbol{Z}_{\lambda,p}(\cdot)$ is asymptotically regular i.e. $\|\boldsymbol{Z}_{\lambda,p}^{(n+1)}(\vec{x}) - \boldsymbol{Z}^{(n)}(\vec{x})\| \implies \|\vec{x}^{\,(n+1)} - \vec{x}^{\,(n)}\| \to 0$ as $n \to \infty$ □

**Lemma 7.** *The fixed points of $\boldsymbol{Z}_{\lambda,p}(\cdot)$ are also the stationary points of $\boldsymbol{Z}_{\lambda,p}(\cdot)$.*

*Proof.* Let $u^*$ be the fixed point that the algorithm converges to. Then we have

$$\begin{aligned} u^* &= \boldsymbol{Z}_{\lambda,p}(u^*) \\ &= \boldsymbol{D}_{\lambda,p}(\vec{u}^{\,*} - \underbrace{\boldsymbol{A}^*(\boldsymbol{A}\,(\vec{u}^{\,*}) - \vec{y})}_{\nabla f_2 = 0}) \\ &= \boldsymbol{D}_{\lambda,p}(u^*) \end{aligned}$$

Thus if $u^{\,*}$ is a fixed point, then $\nabla f_2(u^*) = 0$ and $u^* = \boldsymbol{D}_{\lambda,p}\,(u^*)$ which implies that first order optimality conditions hold and thus $x^*$ is a not only a fixed point but also a stationary point (local minimum). □

With Lemma 5 and 6, we can now invoke Bruck's theorem [79] which establishes that

successive iterates defined by $\vec{u}^{\,(n)} = \boldsymbol{Z}_{\lambda,p}(\vec{u}^{\,(0)})$ converges to a fixed point of $\boldsymbol{Z}_{\lambda,p}$ which by Lemma 7 is a local minimum.

# CHAPTER 4
# NUMERICAL RESULTS

In this section, we first use IAN to super-resolve clinically relevant features in MRI, CT and Fluroscopic images to augment diagnosis of pathological conditions. Secondly, we show that when IAN is used for undersampled reconstruction, the MRI and CT reconstructed images are free of the artifacts that are common to competing state of the art methods. Following this, we present IAN with TV for denoising and conclude with a proof of concept blind deconvolution result

## 4.1 Single Image Super-resolution

The margins of a tumor has significant clinical value as it helps determine tumor type and aggressiveness which subsequently informs treatment protocols and thus patient prognosis. In Fig 4.1 we use IAN to super-resolve a temporal glioma by an overall factor of 4 (2 in each dimension). We benchmark our results against the state of the art techniques (results summarized in Table 4.1) and demonstrate that IAN recovers the relevant features with the greatest fidelity. Visually, the residuals shown in Fig. 4.1 demonstrate that IAN recovers the image with the best tumor definition and detail. Super-resolution results for MR Angiography can be seen in greater detail in the Appendix.

We demonstrate IAN's generalizability to other medical imaging modalities by considering X-ray Fluroscopic images. The treatment outcomes of invasive interventional radiology procedures are directly tied the resolution of these types of images. Clinicians need a clear view of the inserted guidewire for appropriate maneuvering around biological barriers and direct treatment of pathologies. In Fig. 4.2 we demonstrate IAN's ability to super-resolve and thus reconstruct a high resolution image of a guidewire with the least error. A careful examination of the residuals in Fig. 4.2 reveals that IAN is able to capture

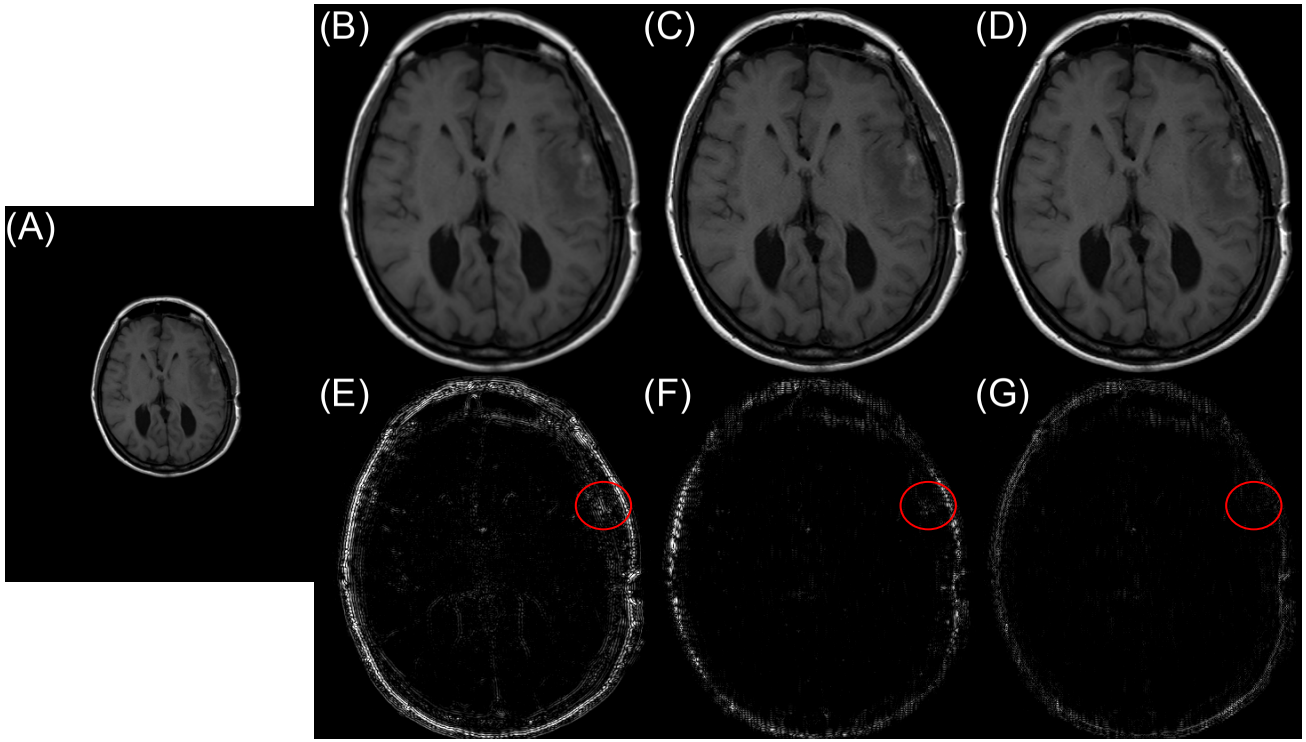


Figure 4.1: MRI tumor Superresolution results using IAN and state of the art super-resolution techniques. The tumor can be observed as the small area of bright intensity in the right temporal lobe (A) Observed low resolution image (B) Image recovered using the method of Sparse Mixing Estimators (SME) [71] (PSNR: 40.31 dB, SSIM: 0.987) [71] (C) Image recovered using SARA (PSNR : 45.05 dB, SSIM: 0.995) (D) Image recovered using IAN (PSNR : 47.02 dB, SSIM : 0.995) (E) SME residual relative to ground truth (F) SARA residual relative to ground truth (G) IAN residual relative to ground truth. (All residuals have been amplified by a factor of 10 to enhance visual observation of reconstruction differences). From the residuals and numerical reconstruction metrics, it is evident that IAN recovers the high resolution image with the highest fidelity. Of greater clinical interest is IAN's recovery of tumor details and margins with the least errors of all techniques.

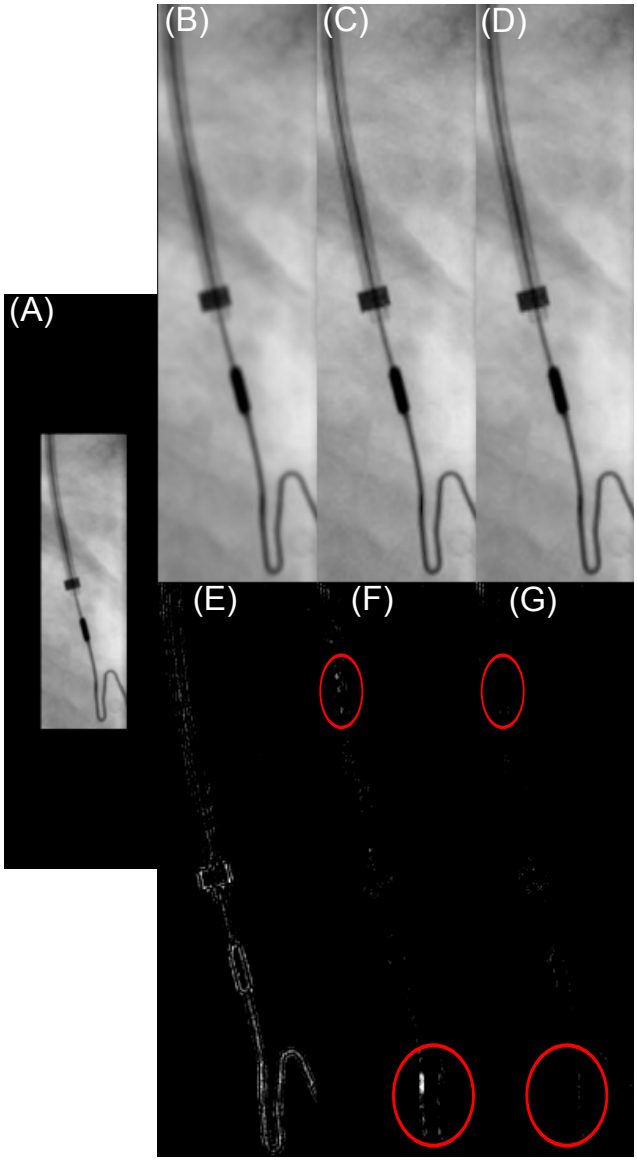


Figure 4.2: X-Ray Fluroscopic Image super-resolution. (A) Observed low resolution image (B) Image recovered using the method of sparse mixing estimators (PSNR : 41.36 dB, SSIM : 0.982) (C) Image recovered using SARA (PSNR : 45.02 dB, SSIM : 0.989) (D) Image recovered using IAN (PSNR : 46.48 dB, SSIM : 0.990) (E) SME residual relative to ground truth (F) SARA residual relative to ground truth (G) IAN residual relative to ground truth. Residuals were magnified by factor of 15 to aid in visualization. IAN reconstructs the general structure of the guidewire with the highest fidelity compared to competing methods.

Table 4.1: Summary of Super-resolution Reconstruction

| | | **Reconstruction Method Employed** | | | | | | | | | | |
|---|---|---|---|---|---|---|---|---|---|---|---|---|
| **Image** | **Metric** | Bilinear | Bicubic | Box | Lanczos 2 | Lanczos 3 | SME | NARM | SAIST | FISTA | SARA | IAN |
| Tumor | PSNR (dB) | 34.41 | 35.23 | 33.29 | 35.25 | 35.54 | 40.31 | 32.32 | 30.29 | 44.61 | 45.05 | **47.02** |
| | SSIM | 0.969 | 0.975 | 0.964 | 0.975 | 0.977 | 0.987 | 0.896 | 0.963 | 0.994 | **0.995** | **0.995** |
| Angiography | PSNR (dB) | 30.06 | 30.82 | 29.09 | 30.84 | 31.07 | 34.66 | 30.42 | 31.21 | 37.43 | 37.65 | **38.65** |
| | SSIM | 0.879 | 0.892 | 0.878 | 0.893 | 0.897 | 0.916 | 0.723 | 0.900 | 0.936 | 0.942 | **0.943** |
| Guidewire | PSNR (dB) | 35.94 | 36.84 | 34.77 | 36.87 | 37.14 | 41.36 | 39.96 | 43.21 | 43.07 | 45.02 | **46.48** |
| | SSIM | 0.965 | 0.971 | 0.954 | 0.971 | 0.971 | 0.982 | 0.974 | 0.977 | 0.977 | 0.989 | **0.990** |
| Scaphoid | PSNR (dB) | 25.27 | 25.50.82 | 25.08 | 25.51 | 25.60 | 26.45 | 26.04 | 24.86 | 26.88 | 27.32 | **27.80** |
| | SSIM | 0.519 | 0.550 | 0.539 | 0.552 | 0.564 | 0.597 | 0.549 | 0.613 | 0.684 | 0.700 | **0.732** |

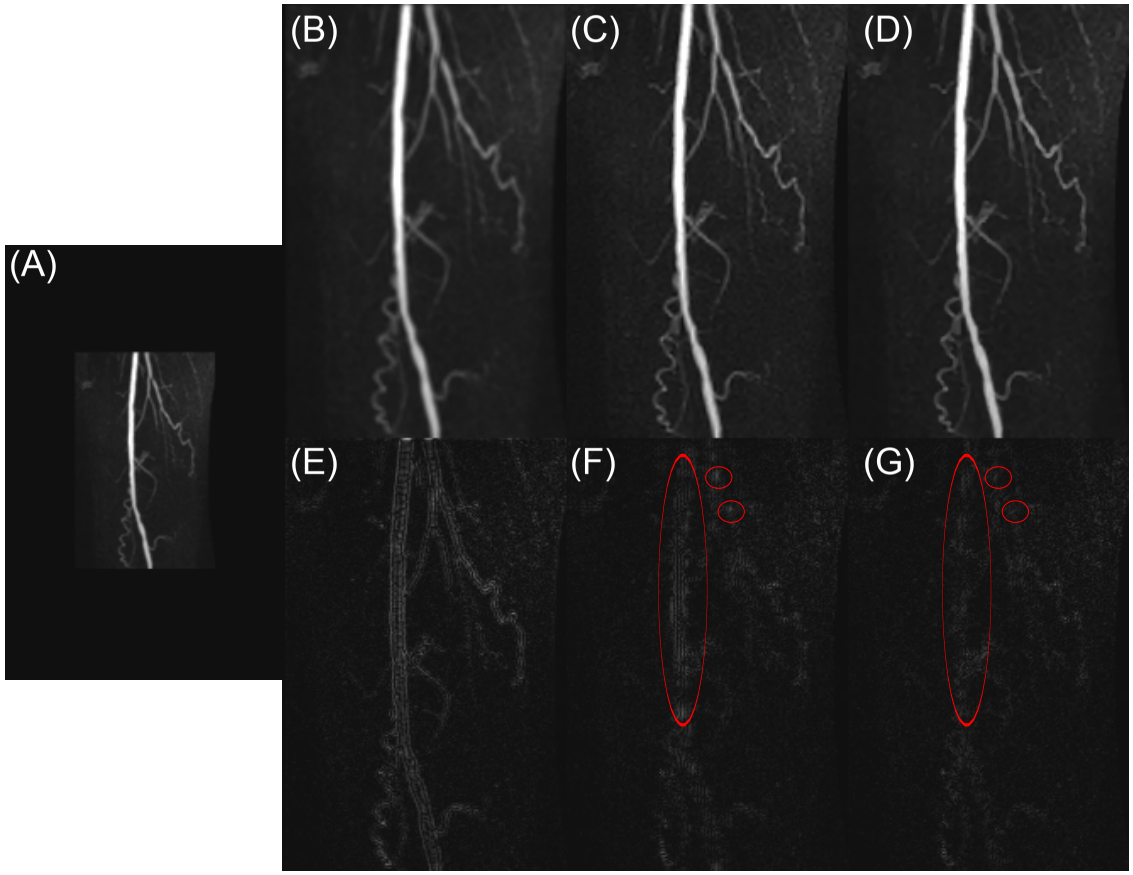


Figure 4.3: MRI Angiography Superresolution results using IAN and state of the art super-resolution techniques. (A) Observed low resolution image (B) Image recovered using the method of sparse mixing estimators [71] (PSNR: 34.67 dB, SSIM : 0.916 (C) Image recovered using SARA (PSNR : 37.64 dB, SSIM : 0.942) (D) Image recovered using IAN (PSNR : 38.03 dB, SSIM : 0.943) (E) SME residual relative to ground truth. (F) SARA residual relative to ground truth (G) IAN residual relative to ground truth. (All residual have been amplified by a factor of 2 to aid in visualization). The highlighted regions in the residual images draw attention to overall arterial structure and bifurcations that are super-resolved with highest fidelity using IAN relative to the next best reconstruction method : SARA. It are these regions that are of most interest to clinicians when dealing with potential embolic plaques / aneurysms.

both the structure and the undulations of the guidewire with almost no errors while the best competing method (SARA), does not.

In Fig. 4.3 we use demonstrate IAN's ability to super-resolve MRI angiographic images with high accuracy in regions of physiological interest. Numerous research studies have shown that blood flow reversal occurs at arterial / venule bifurcations [87]. These regions are prime locations for both build up for plaque (atherosclerosis)[87, 88, 89] and on the other hand, for aneurysms [90]. In Fig. 4.3 it is clear that IAN super-resolves these physiological vital regions with the greatest degree of fidelity when compared to other state of the art techniques. A cursory examination of the residual for the IAN super-resolved image in Fig. 4.3 reveals that the main arterial trunk has been recovered with the least error thereby aiding clinicians in examining arterial integrity.

One of the challenges associated with wavelet based sparse reconstruction is the generation of wavelet artifacts. These artifacts manifest as horizontal and vertical banding in the reconstructed image. SARA, unlike IAN, is prone to these type of artifacts. SARA's super-resolution of one of the test MRI Scaphoid images, whose quantitative results are shown in Table 4.1, suffers from this artifact (figure not shown). In our experimentation, this form of artifact was commonly observed in signals recovered using SARA (see Fig. 4.4). A quantitative summary of super-resolution recovery results can be found in Table 4.1. Despite the varied modality and drastic difference in image type, the analysis based non convex framework (IAN) outperforms competing state of the art methods (reweighted $L_1$: SARA, synthesis $L_1$: FISTA and dedicated super-resolution methods).

## 4.2 Undersampled Image Recovery

In this section, we use IAN to recover undersampled MRI and CT images. A summary of the results shown here can be found in Table 4.2. For the MRI images, an undersampling factor of $4$ was used while for CT images, 45 views / projections were used for the reconstruction. A cursory examination of Table 4.2 shows that IAN quantitatively outperforms

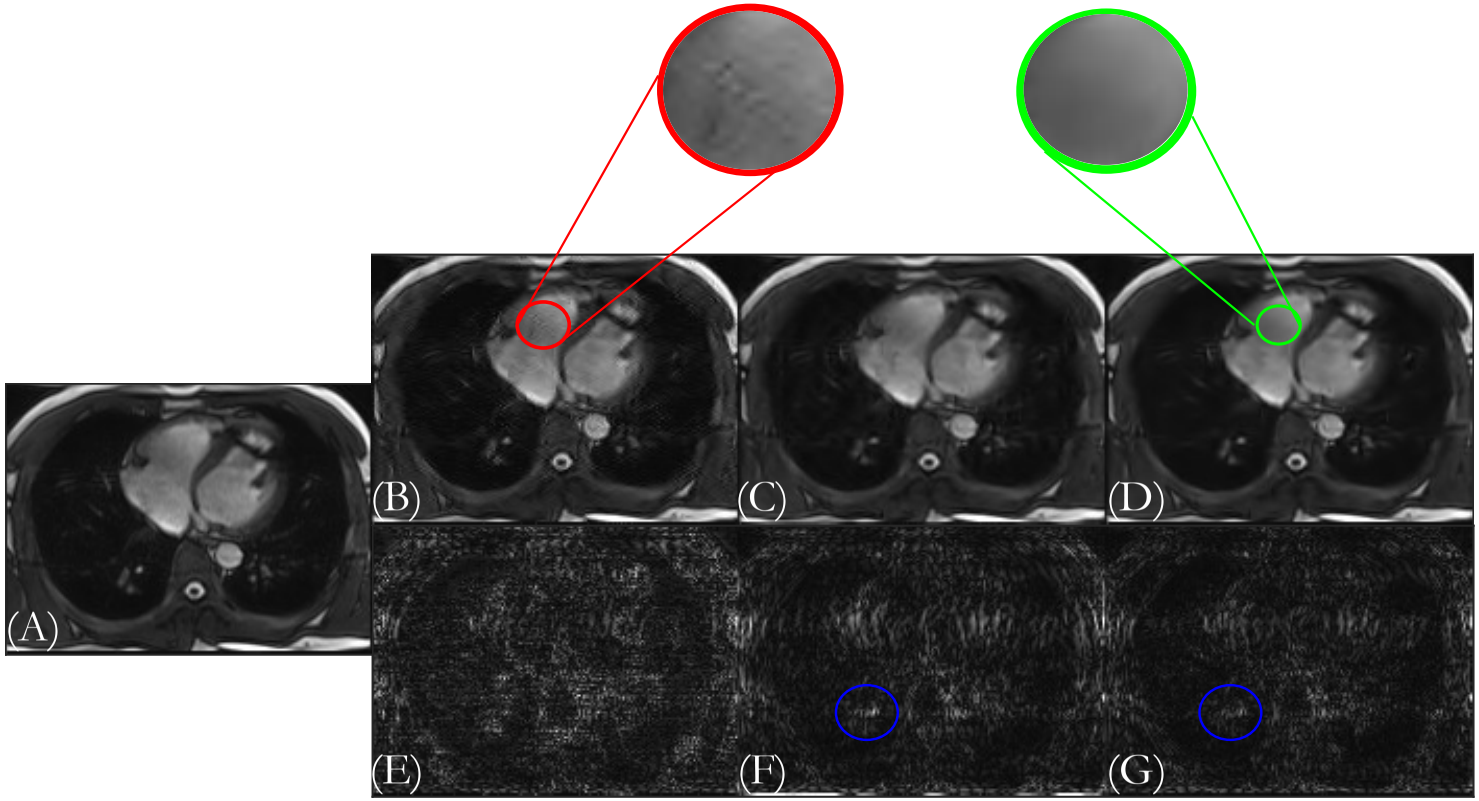


Figure 4.4: MRI undersampled reconstruction with $25\%$ sampling. (A) The ground truth image is shown on the right. (B) Reconstruction afforded by SARA (Reweighted $L_1$). (C) Chartrand's analysis $L_p$ algorithm based recovery. (D) Reconstruction using IAN. The residuals for SARA (E), Chartrand (F) and IAN (G) are depicted to highlight reconstruction errors relative to the ground truth. The blue insets highlight errors in regions of high frequency that can be seen when using Chartrand's reconstruction methodology relative to IAN. The red and green insets depict the lack of wavelet reconstruction artifact when using IAN. IAN reconstructs the underlying signal with $\approx 3$ dB gain relative to the closest state of the art.

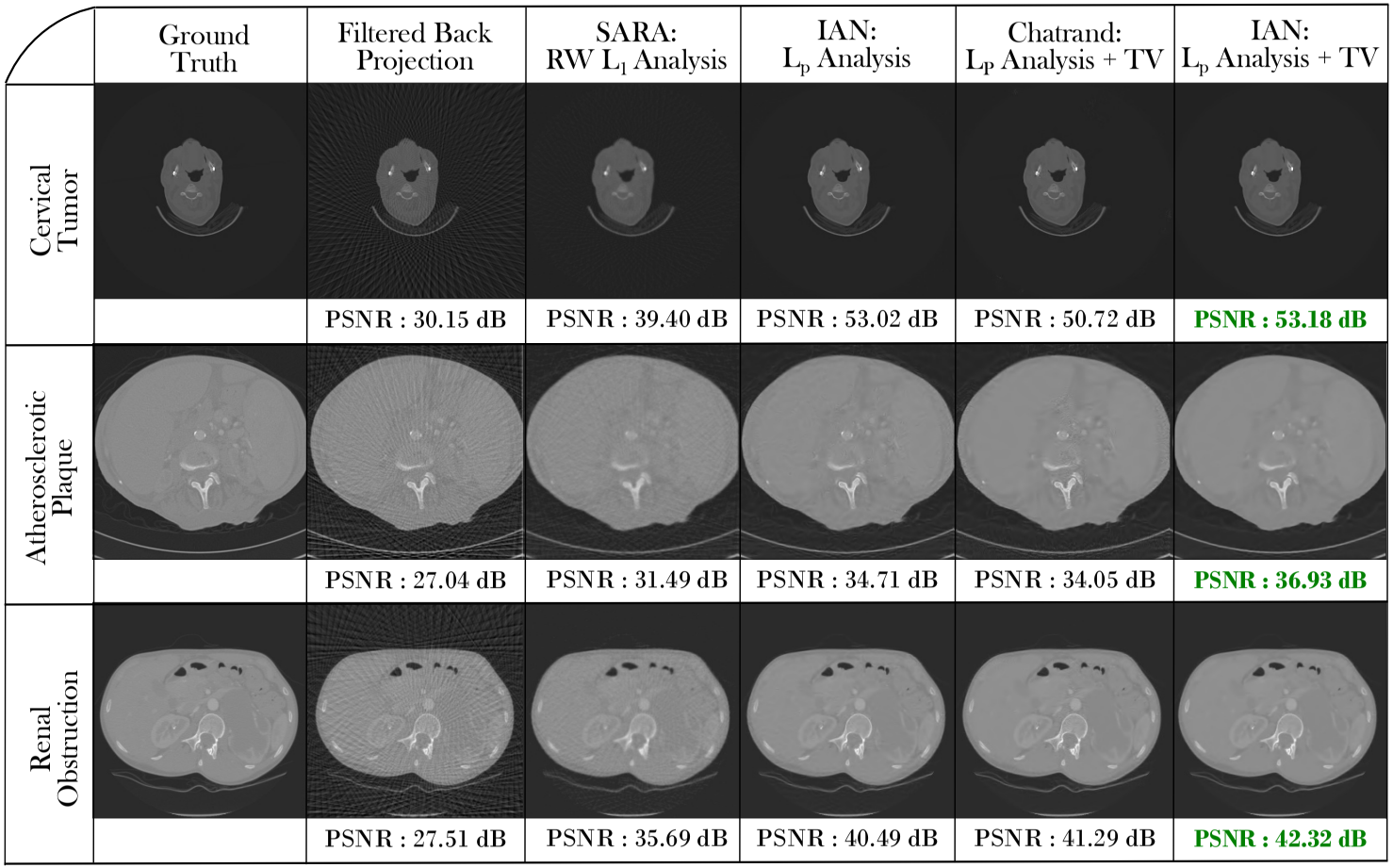


Figure 4.5: Recovery of undersampled (45 views) computed tomography images. The second column depicts the reconstruction afforded by standard filtered back projection method. Sparse non convex reconstruction using an analysis reweighted $L_1$ prior is shown in the third column while the fourth column contains the reconstruction afforded by analysis based non convex $L_p$ prior (IAN) . The fifth column shows the reconstruction obtained when using Chartrand's $L_p$ with TV algorithm Finally, in column six, the IAN with TV algorithm reconstruction is shown. The quantitative results for each recovery can be examined in Table 4.2. In each case, it is clear that the non convex $L_p$ and TV prior outperforms state of the art reweighted $L_1$ and other sparse regularization techniques.

Table 4.2: Summary of Undersampled Reconstruction Results

| | | **Reconstruction Method Employed** | | | | | | |
|---|---|---|---|---|---|---|---|---|
| **Image - MRI** | **Metric** | Sampling Percentage | Least Sq. $L_2$ | Syn. $L_1$ | Analy. $L_1$ | RW. $L_1$ (SARA) | Chartrand $L_p$ | $L_p$ (IAN) |
| Cardiac | PSNR (dB) | 25.00% | 29.82 | 33.82 | 35.53 | 34.20 | 34.88 | **37.69** |
| Lumbar | PSNR (dB) | 25.54% | 38.37 | 41.20 | 41.11 | 41.85 | 40.71 | **42.74** |
| Neuro | PSNR (dB) | 28.13% | 28.02 | 30.07 | 31.55 | 31.71 | 31.42 | **32.04** |
| | | **Reconstruction Method Employed** | | | | | | |
| **Image - CT** | **Metric** | Filtered BP. | Least Sq. $L_2$ | Syn. $L_1$ | RW. $L_1$ (SARA) | $L_p$ (IAN) | $L_p + TV$ [31] | $L_p + TV$ (IAN-TV) |
| Cervical Tumor | PSNR (dB) | 30.15 | 34.53 | 47.50 | 39.40 | 53.02 | 50.72 | **53.18** |
| Renal Obs. | PSNR (dB) | 27.51 | 29.91 | 36.05 | 35.69 | 40.49 | 41.29 | **42.32** |
| Atheroscelrosis | PSNR (dB) | 27.04 | 28.30 | 33.37 | 31.49 | 34.71 | 34.05 | **36.93** |

state of the art convex (Analysis and Synthesis $L_1$ and non convex (SARA and Chartrand's analysis $L_p$ [31]) recovery methods.

While the quantitative results might be promising, it is often the case that the qualitatively results do not follow in suite. In Fig. 4.4 we show that IAN reconstructs undersampled images with greater qualitative and quantitative accuracy relative to state of the art convex and non convex methods. A cursory examination of the insets in Fig. 4.4 show that IAN does not suffer from wavelet reconstruction artifacts that undersampled SARA reconstruction suffers from. Furthermore, the blue insets depict lower recovery error for high frequency regions for IAN relative to Chartrand's $L_p$ method.

In Fig. 4.5 undersampled CT recovery of multiple images are shown across a host of reconstruction methods. In each reconstruction method employed, both iterative and non iterative, the undersampling causes significant streaking artifacts. We plot the reconstruction afforded by IAN with TV in the last column of Fig .4.5 in order to demonstrate the elimination of any form of streaking artifacts. Furthermore, the regions of physiological interest (cervical tumor in the top row, left renal obstruction in the middle row and plaque deposition in the bottom row) are best reconstructed using IAN with TV. Even without the use of the total variation regularizer, IAN quantitatively outperforms the state of the art competing methods Table. 4.2. IAN with TV is also able to preserve image contrast which of significant interest to clinicians given the differential phenotyping that occurs based on contrast agent expression.

## 4.3 Image Denoising

In this section, we use IAN with a TV regularizer to denoise images. A summary of all denoising results can be found in Table 4.3. In Table 4.3 we provide the best numerical results obtained for IAN in the denoising images. The denoised figures for IAN were chosen for visual acuity.

One of the long standing challenges associated with using the TV regularizer is the

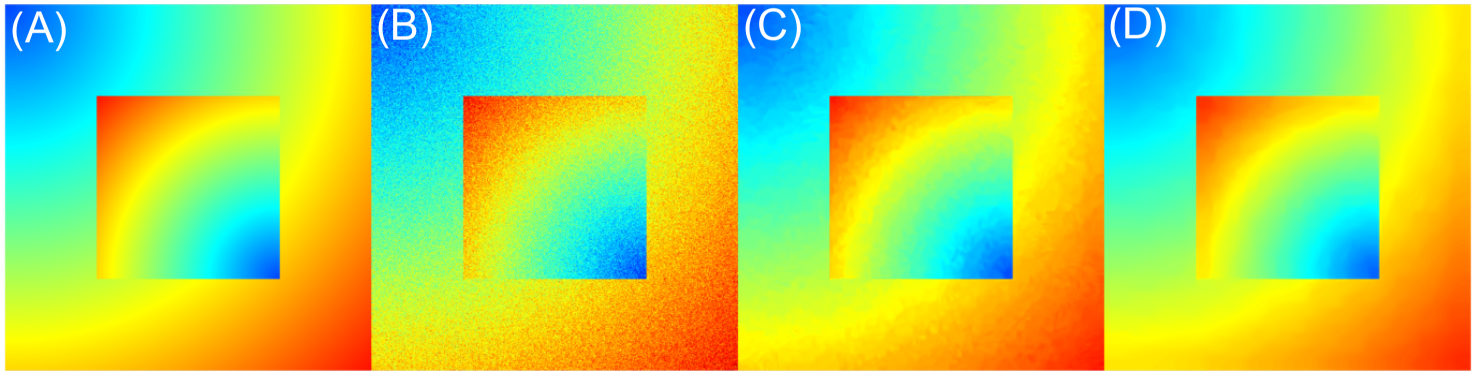


Figure 4.6: Phantom Denoising result using IAN with TV. (A) Original Phantom Image (B) Phantom with white gaussian noise (standard deviation : 20) (C) Denoised image recovered using BM3D with oracle standard deviation (PSNR : 41.92 dB, SSIM : 0.421, IQM :0.413 ) (D) Denoising image recovered using IAN with TV (PSNR : 43.93 dB, SSIM : 0.881, IQM : 0.667). IAN with TV denoises the phantom with least error and does not introduce stair casing artifacts that are common to total variation regularizers.

Table 4.3: Summary of Denosing Results

| | | Denoising Method Employed | | | | |
|---|---|---|---|---|---|---|
| **Image** | **Metric** | SARA | FGP | PLOW | BM3D | IAN (Best) |
| Phantom | PSNR (dB) | 22.15 | 6.09 | 42.43 | 41.92 | **43.93** |
| | SSIM | 0.022 | 0.003 | 0.515 | 0.421 | **0.881** |
| | IQM | -0.215 | -0.709 | 0.458 | 0.413 | **0.667** |
| Fluroscopic Denoising | IQM | -0.683 | 0.378 | 0.450 | 0.493 | **0.620** |
| Cerebral Aneurysm Denoising | IQM | -0.215 | 0.234 | 0.408 | 0.571 | **0.715** |
| MRI Knee Denoising | IQM | -0.276 | 0.487 | 0.374 | 0.438 | **0.543** |

generation of stair casing artifacts. To examine this, we developed the piecewise constant phantom seen in Fig 4.6. We simulate a noisy image by adding gaussian white noise with a standard deviation of 20 and recover the denoised image using state of the art denoising algorithms. While IAN performs better than BM3D in Fig 4.6, it must be noted that BM3D was not designed for non textured images.

In Fig 4.7, we use IAN to denoise a noisy X-ray fluroscopic image with no apriori knowledge about noise statistics. In fluroscopic images, contrast is of critical importance as physicians inject contrast agents continuously to determine catheter location relative to anatomical markers. Noise in such images reduces contrast and significantly increases the need for exposure to large quantities of contrast agents. From Table 3 it is clear that IAN denoises the input image with the greatest fidelity. In Fig 4.7 we demonstrate that IAN denoises the provided fluroscopic image better than state of the art methods. We also use Fig 4.7 to demonstrate the quantitative and qualitative discrepancy of the IQM metric. We show that IAN is both quantitatively and qualitatively better than the state of the art methods.

In Fig 4.8 we consider the challenging problem of denoising an image with non uniform noise (a MRI angiography scan). In this specific case, the patient suffers from a cerebral aneurysm which can be seen in the right hemisphere near the corpus callosum. Clear boundaries are of vital clinical importance as it used to determine clinical progrnosis and treatment paradigms. The arterial out pouching and its anatomical boundaries are clearest

in the image denoised by IAN.

In order to address parameter tuning in the absence of ground truth, the applicability of [91] (Stien's Unbiased Risk Estimator : SURE) was tested for IAN. In Fig 4.9 we demonstrate the SURE estimate of the mean square error relative to the true mean square error (MSE) as the parameters were varied across a large dynamic range. A cursory examination reveals that the SURE estimate of MSE tracks the ground truth MSE accurately. Thus, reference less parameter tuning (at the cost of computation) can be achieved thereby eliminating the need for manual parameter tuning. In non denoising applications where the Monte Carlo method might not apply, parameter tuning can be computationally expensive given the large parameter space that needs to be searched. For the result shown in Fig. 4.9, the Monte Carlo parameters that were used were $\epsilon = 10^{-12}$ and $\sigma = 0.1$ (see [91] for parameter details and explanation).

## 4.4 Blind Deconvolution

In Fig. 4.10 we present proof of concept results for blind deconvolution using IAN. A cursory examination of Fig. 4.10 reveals that despite the $L_1$ deconvolution kernel being recovered with greater accuracy relative to IAN's blind deconvolution kernel by 8dB, IAN's recovered image has significantly higher quality (quantitatively by 3 dB and qualitatively Fig. 4.10C vs D). This combined with the minor difference between the signal recovered for IAN with blind deconvolution (Fig. 4.10D) and IAN with oracle parameters (Fig. 4.10E) suggests that IAN is very robust to errors in the imaging model and is thus highly stable despite its inherent non convexity.

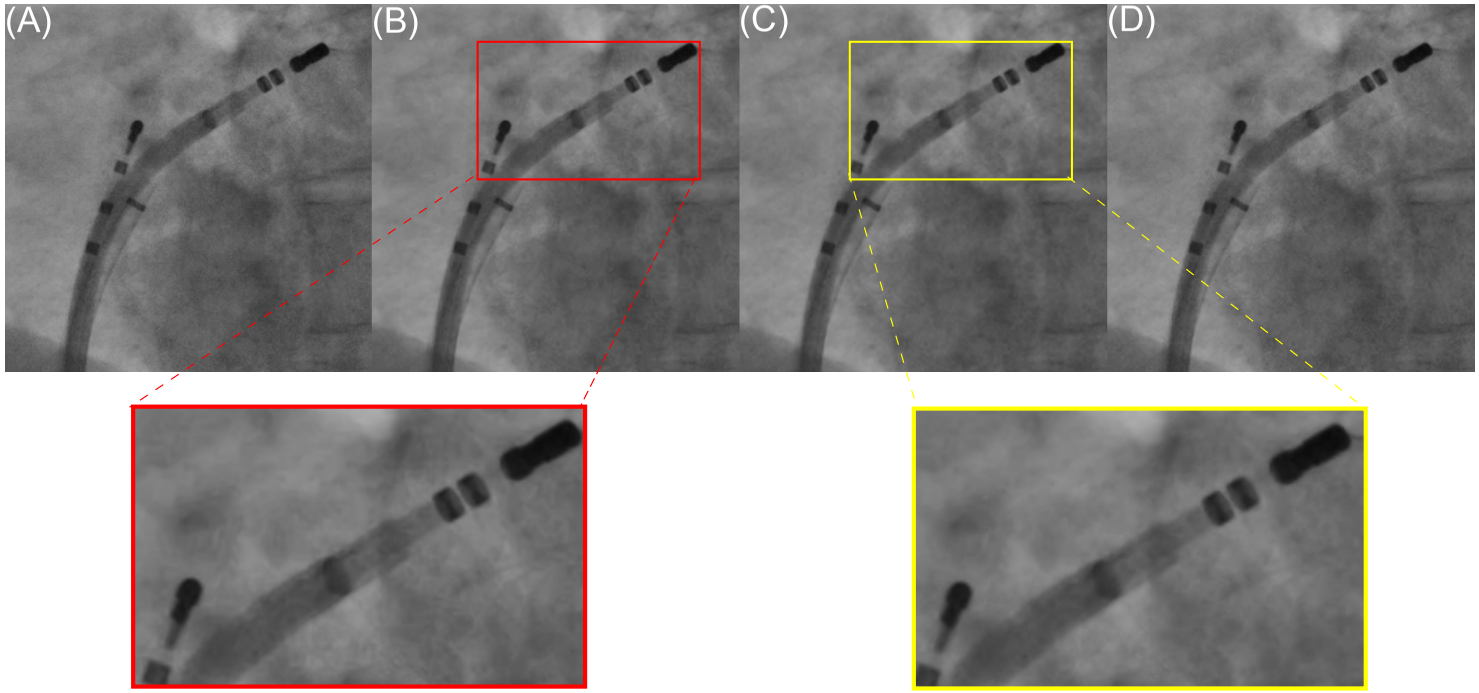


Figure 4.7: Fluroscopic CT image denoising. (A) Ground truth noisy image (B) Image denoised using BM3D (IQM : 0.493) (C) Image denoised using IAN (best visual reconstruction) (IQM : 0..423). (D)Image denoised using IAN (best IQM result) (IQM : 0.620). The insets show that IAN visually denoises relevant features better than BM3D does. Thus both quantitatively and qualitatively IAN performs better than the next best state of the art technique (BM3D)

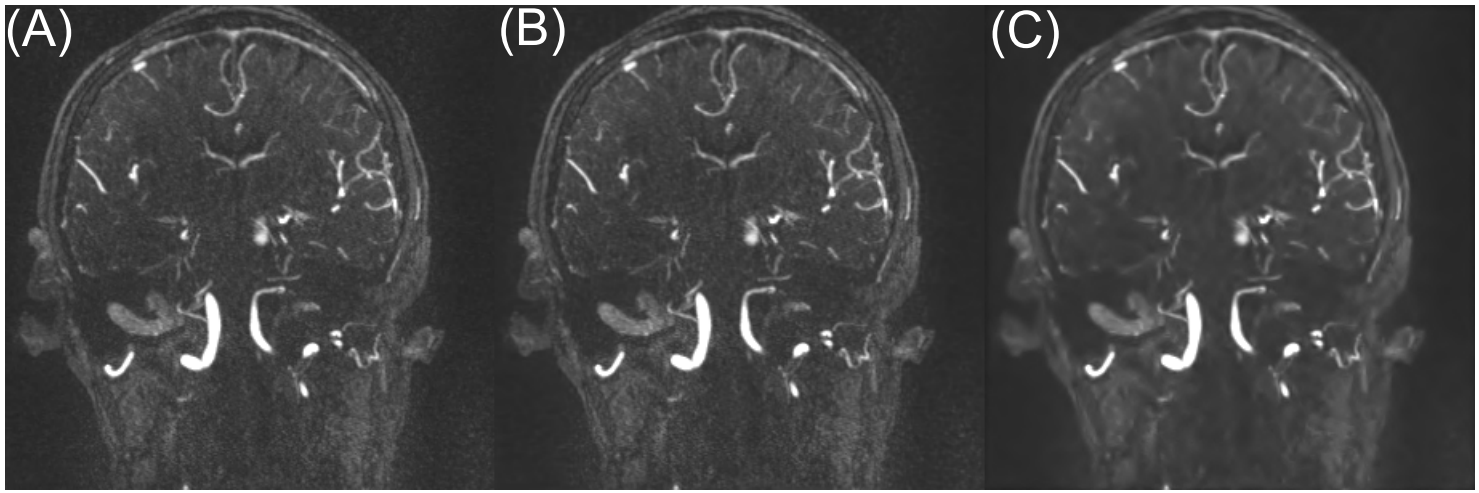


Figure 4.8: MRI angiographic image image denoising. (A) Ground truth noisy image (B) Image denoised using BM3D (C) Image denoised using IAN (best visual reconstruction). A cursory examination of the image reveals the superior visual denoising by IAN relative to BM3D.

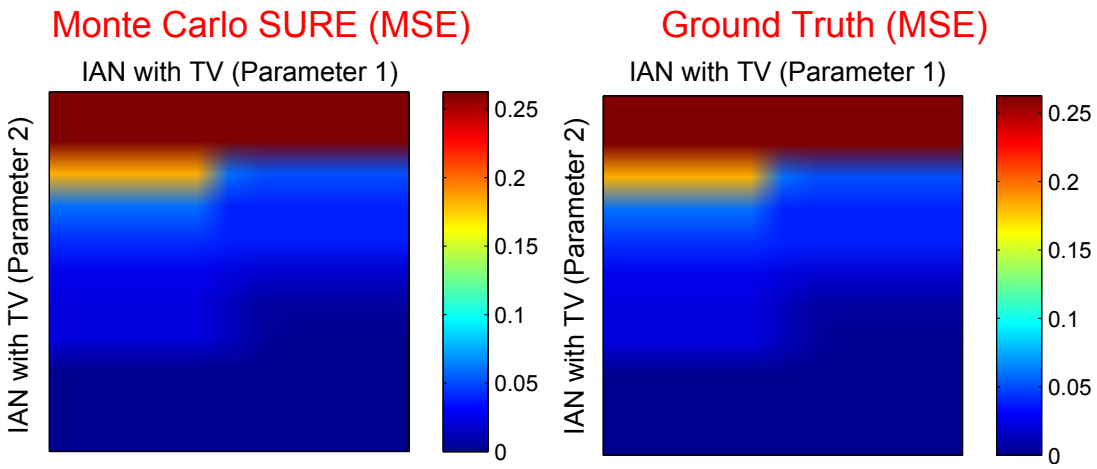


Figure 4.9: Mean square error estimate based on Monte Carlo Stein's Unbaised Risk Estimator (left) and ground truth mean square error. The 2 regularization parameters used in IAN with TV($L_p$ norm and the TV norm) form the two axis.

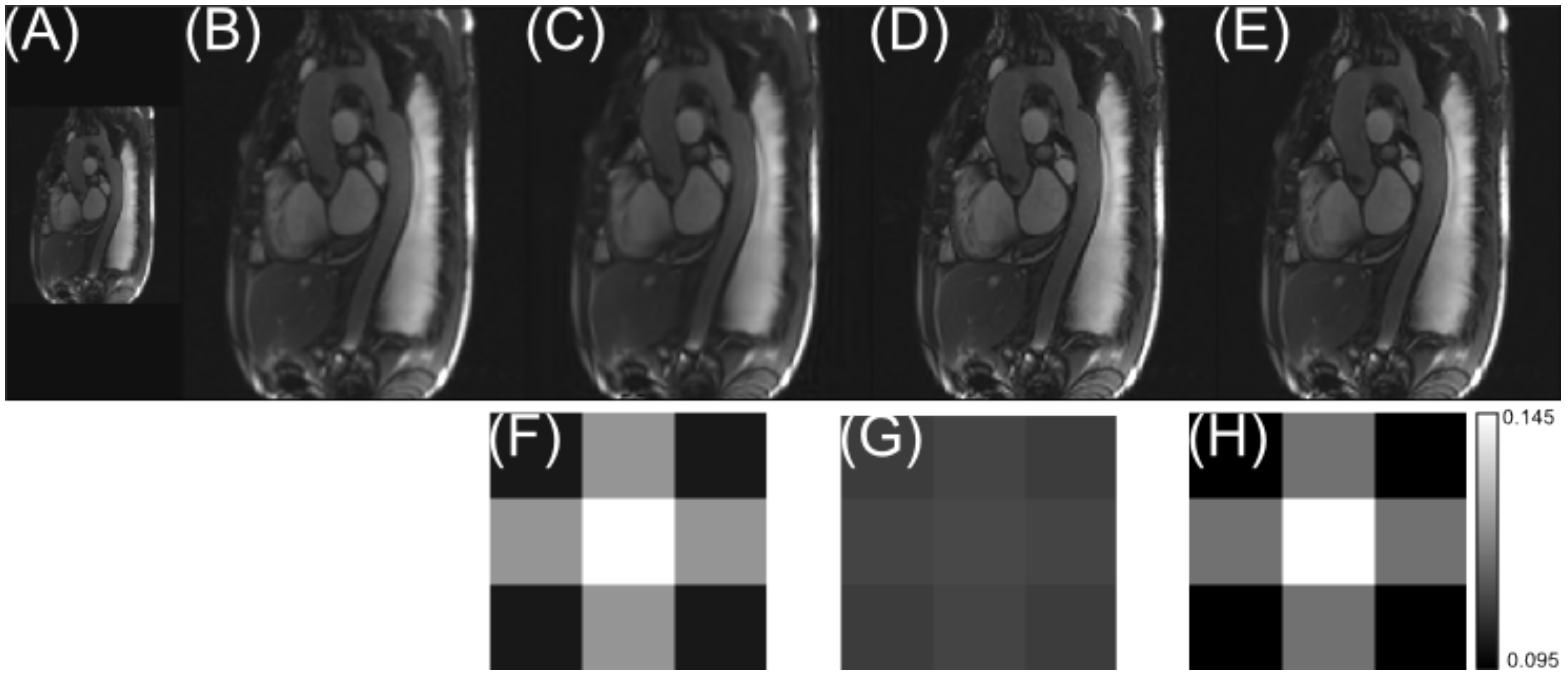


Figure 4.10: Blind Deconvolution Results. (A) Observed low resolution image (B) Lanczos Interpolation based image recovery (PSNR : 35.55 dB). This was used as a warm start for both FISTA and IAN shown in (C-E)(C) $L_1$ recovery (FISTA) with blind deconvolution (PSNR : 38.04 dB) (D) IAN recovery with blind deconvolution (PSNR : 41.26 dB) (E) IAN recovery with oracle knowledge of forward model blur kernel (PSNR : 41.65dB) (F) Kernel recovered with $L_1$ (FISTA) blind deconvolution (PSNR : 27.30 dB) (F) Kernel recovered with IAN blind deconvolution (PSNR : 19.08 dB) (G) Ground truth kernel. A support and radial symmetry prior was imposed on the kernel recovery. IAN with blind deconvolution recovers an image that has a PSNR value which is 3dB higher than $L_1$ (FISTA) with blind deconvolution despite the lower accuracy in kernel estimation. This combined with the 0.04 dB difference between IAN with and without the oracle blur kernel (D vs E), suggests that IAN is very robust to errors in the imaging model

# CHAPTER 5
# DISCUSSION

Thus far we have demonstrated IAN's ability to outperform quantitatively and qualitatively the state of the art algorithms for challenging image processing applications. Here were consider the computational load of IAN relative to other state of the art non convex algorithms for undersampled image recovery. All other factors remaining equal, the computational load for an algorithm can be quantified by examining the number of times that the forward and adjoint linear operator $(\boldsymbol{A}(\cdot), \boldsymbol{A}^*(\cdot))$ are applied. Equally important is the application of the forward and adjoint wavelet frame operators $(\boldsymbol{W}(\cdot), \boldsymbol{W}^*(\cdot))$. In Table 5.1 we compare IAN with other non convex algorithms such as SARA and Chartrand's non convex algorithm presented in [31] for the undersampled cardiac reconstruction presented in Fig. 4.4.

Given the same reconstruction goal of recovering an undersampled cardiac MRI image, we find that IAN is computationally cheaper by nearly a factor of 2 relative to [31] and a factor of 3 relative to [25]. Both SARA [25] and Chartrand's $L_p$ approach [31] utilize a highly nested iterative framework that necessitates large operator counts. Furthermore, it must be noted that Chartrand's algorithm does not converge unless the user inputs exact iteration limits. As the iteration limits are increased, we found that Chartrand's algorithm tends to diverge.

The generic framework that we have developed for IAN allows for the use of a range of wavelet regularization terms. Directional and rotational invariance can be achieved through the use of cycle spinned wavelet transforms, dual tree wavelet transforms, undecimated wavelet transforms and steerable pyramids. Furthermore, the proximal framework used in developing IAN with TV can be modified in a principled way for efficient parallel implementation on standard multi-core systems. A cursory examination of the framework used

Table 5.1: Summary of Approximate Computational Cost For State of Art Non Convex Algorithms: (Based on Fig. 4.4)

| **Non Convex Algorithm** | $\boldsymbol{A}(\cdot)$ | $\boldsymbol{A}^*(\cdot)$ | $\boldsymbol{W}(\cdot)$ | $\boldsymbol{W}^*(\cdot)$ | Total |
|---|---|---|---|---|---|
| SARA [25] | 5000 | 5000 | 4000 | 4000 | 19000 |
| Chartrand [31] | 2160 | 2025 | 2025 | 4050 | 10260 |
| IAN | 1000 | 1000 | 2200 | 2200 | **6400** |

for IAN reveals that algorithm can be trivially altered (change in a single line of code) to switch between an analysis / synthesis based recovery. This is particularly beneficial since there are no theoretical guarantees around which recovery method is superior [46].

Despite these advantages, IAN, like all other non convex algorithms suffer from sensitivity to initialization. For all the results presented in this paper, we initialized super-resolution recovery with extremely fast interpolation based methods. For undersampled recovery, we initialized IAN with an analysis /synthesis based $L_1$ start. For all the undersampled results presented, IAN and SARA were provided the exact same warm start.

Parameter selection is often key component to the success or failure of an optimization algorithm. A cursory examination of Fig. 5.1 shows that IAN is not very sensitive to parameter selection. Within the appropriate regularization window, an alteration in the parameter choice by an order of magnitude, only alters the reconstruction accuracy by 0.1 dB (Fig. 5.1, 5.2). Since parameter choice might be a function of imaging modality, Fig. 5.1 plots the change in reconstructed PSNR based on regularization parameter. A regularization parameter between $10^{-5}$ and $10^{-4}$ seems to work well for a range of super-resolution images across imaging modality. For image denoising applications where the noiseless ground truth is not available, we show that Monte Carlo based Steins Unbiased Risk Estimator (SURE)[91, 92] can be used in order to achieve reference less parameter tuning for IAN with TV (shown in results).

In order to disambiguate the contribution afforded by algorithm structure versus the use of tight analysis frames, we examined reconstruction accuracy with and without these two factors (Fig. 5.3). This was done by comparing the results obtained using a forward

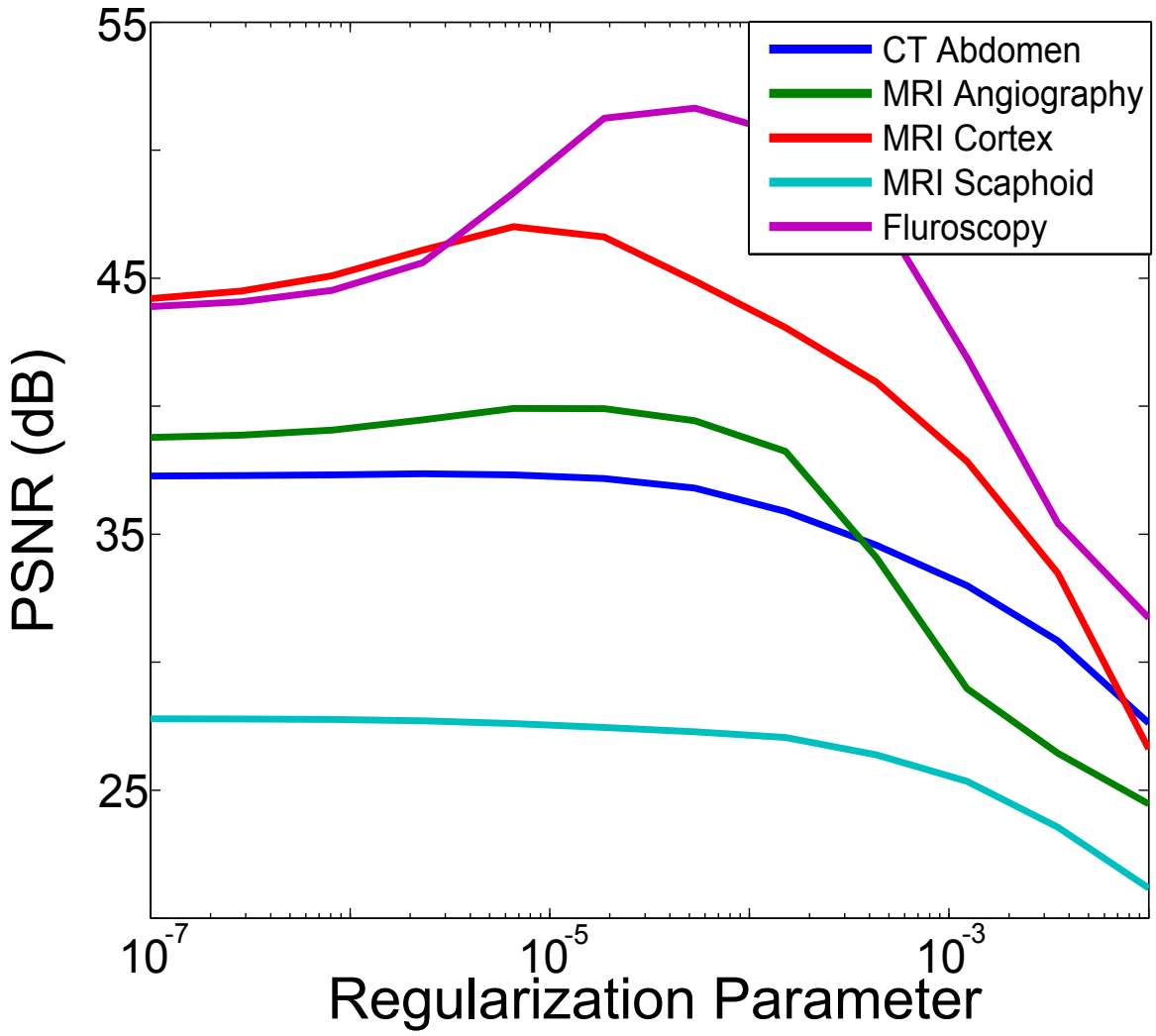


Figure 5.1: Effect of regularization parameter for single image super-resolution using IAN across multiple imaging modalities. The optimal parameter range across modalities lies between $10^{-4}$ and $10^{-5}$.

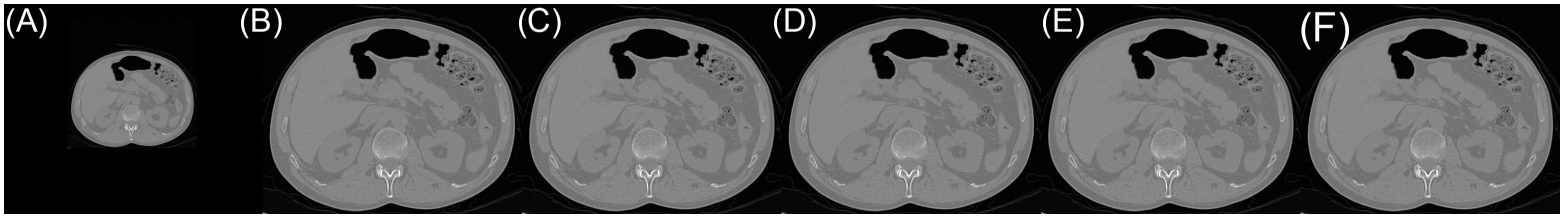


Figure 5.2: Effect of regularization parameter for Computed Tomography single image super-resolution in the image domain using IAN. (A) Observed low resolution image (B) Image reconstructed using IAN $\lambda = 6.6 \times 10^{-6}$, PSNR : $37.32$ dB (C) Image reconstructed using IAN $\lambda = 2.3 \times 10^{-6}$, PSNR : $37.36$ dB (D) Image reconstructed using IAN $\lambda = 8.1 \times 10^{-7}$, PSNR : $37.32$ dB (E) Image reconstructed using IAN $\lambda = 2.85 \times 10^{-7}$, PSNR : $37.29$ dB (F) Image reconstructed using IAN $\lambda = 1.0 \times 10^{-7}$, PSNR : $37.27$ dB. An order of magnitude difference in regularization parameter only changes the PSNR of the reconstructed image by $0.1$ dB.

backward splitting approach (Algorithm 3) versus IAN with and without frames. On examination of Fig. 5.3, it is clear that both the algorithmic framework and the use of frames both play pivotal roles in the superior reconstruction afforded by IAN.

When solving the $L_p$ problem for $p < 1$, we can externally validate the shrinkage operator used in IAN versus the analytical closed form shrinkage operator that exists for specific values of $p < 1$ (Ex. $p = 0.5$ [93]). In Fig. 5.4, we plot the objective function

$$\min_{x \in \mathbb{R}} \frac{1}{2}\|y - x\|_2^2 + \lambda \|x\|_p^p$$

for $y = 1.3$ and $\lambda = 1$. We also plot the result obtained using the shrinkage operator developed by Chartrand [60]. A cursory examination of Fig. 5.4 reveals that the shrinkage operator used in IAN [2] converges to the exact minimum as would be predicted by the closed form analytic shrinkage operator for $p = 0.5$ [93]. Fig. 5.4 demonstrates the fidelity afforded by using a shrinkage operator that is iteratively estimated in place of a closed form operator [60] that sacrifices accuracy for minor gain in computational efficiency. Furthermore, IAN's ability to outperform competing non convex algorithms can be attributed to the increased accuracy afforded by the iteratively estimated shrinkage operator.

When the parameters of the forward model are unknown, we demonstrate proof of concept results for IAN with a standard blind deconvolution splitting approach Fig. 4.10 in appendix. Tangentially, Fig. 4.10 also demonstrates that IAN is more robust to errors in the forward model relative to $L_1$ methods. This in and of itself warrants future exploration.

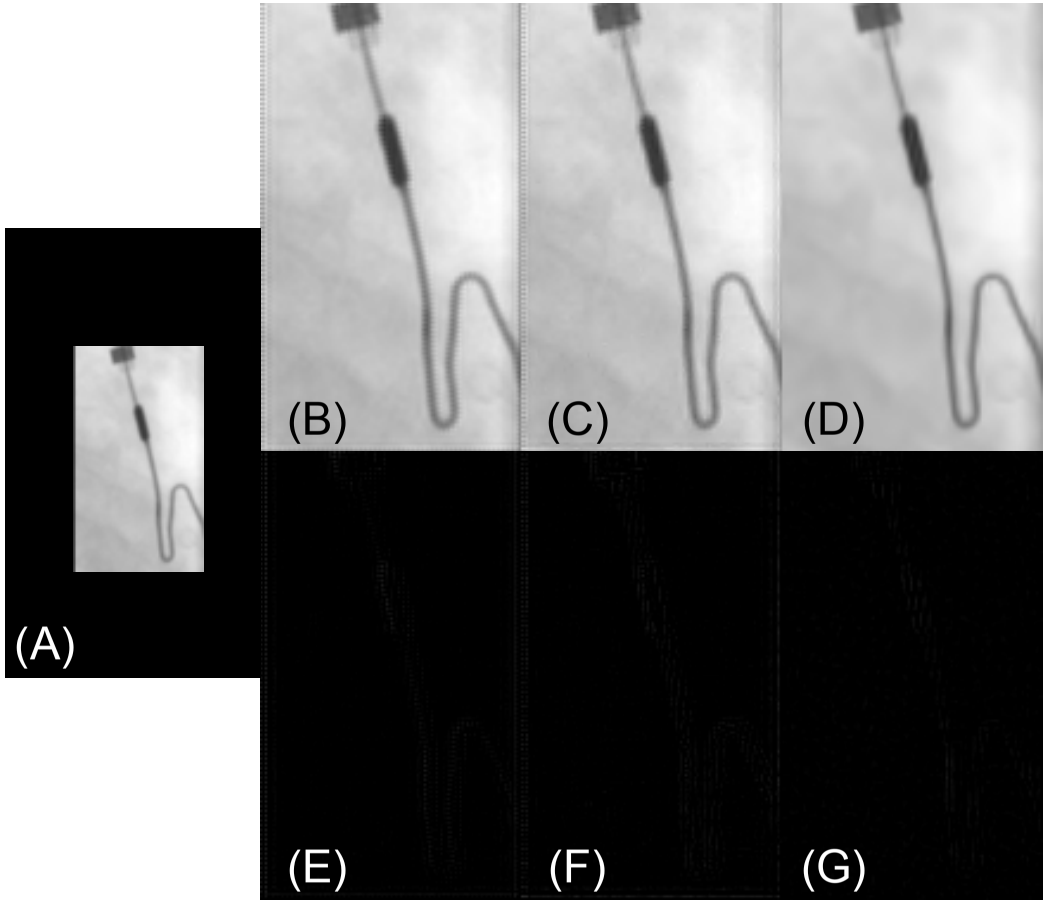


Figure 5.3: Reconstructions which test the benefits afforded by IAN's algorithmic formulation relative to the use of tight frames. (A) Observed low resolution image (B) Recovered image using a forward-backward splitting algorithm with the same shrinkage operator as IAN (PSNR : 38.45 dB). (C) Recovered image using IAN but with a single basis (PSNR : 45.02 dB) (D) Recovered image using IAN with a tight frame (PSNR : 51.64 dB). Residual of each reconstruction is shown in (E) (G). Notice the lack of reconstruction artifacts along the edges of the image in (D,G) and the increased definition along the guidewire. Both components of IAN (algorithmic formulation) and the use of tight frames contribute to enhanced recovery

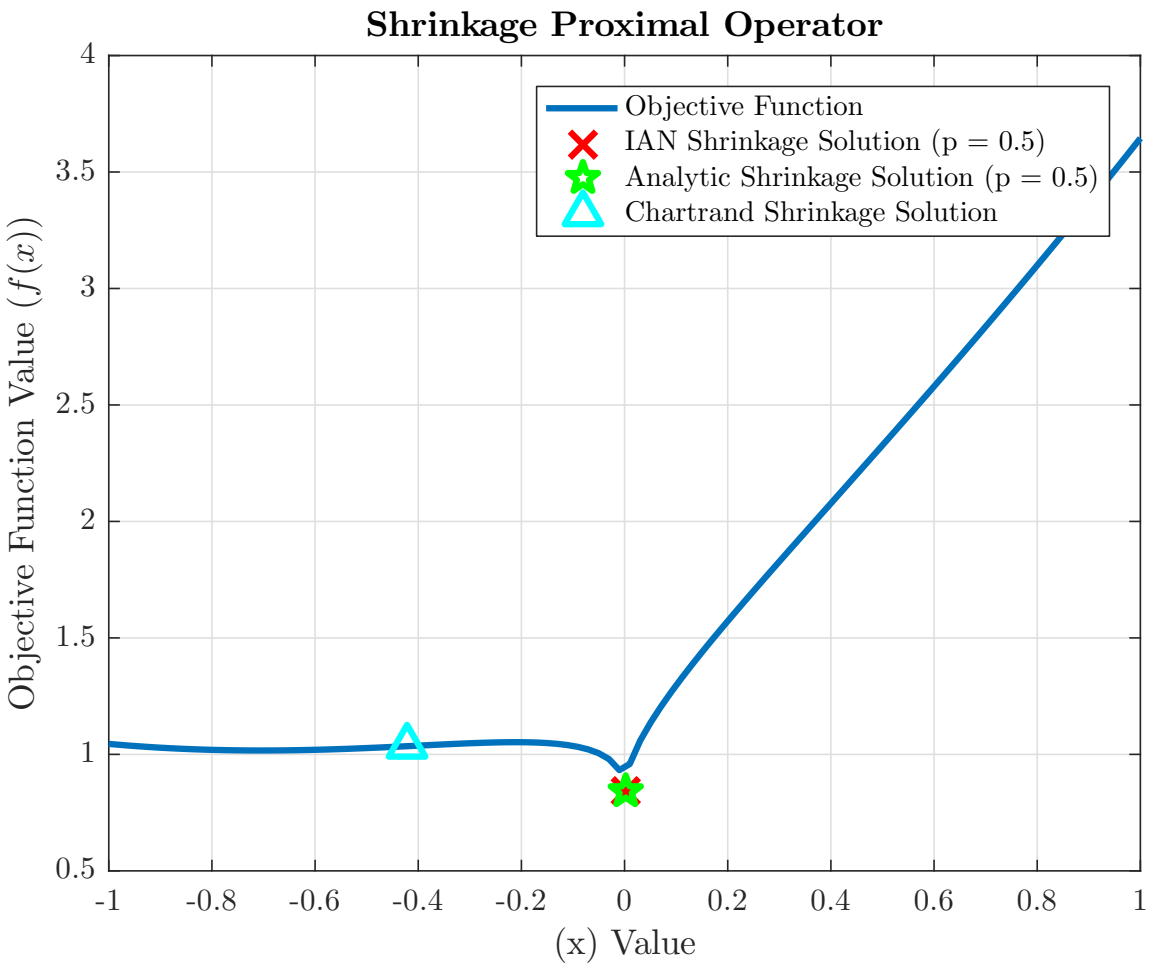


Figure 5.4: Comparison of sparse recovery for the objective function $\min_{x\in\mathbb{R}} \frac{1}{2}\|y-x\|_2^2 + \lambda\|x\|_p^p$ when $p = 0.5$. The three methods plotted are the analytic closed for thresholding operator for $p = 0.5$, Chartrand's $L_p$ shrinkage function and the shrinkage function used in IAN.

# CHAPTER 6
# SUMMARY AND FUTURE WORK

In this work, we have developed a novel algorithm (IAN) for ill posed inverse problems that out performs the current state of the art in signal recovery. We provide the first convergence guarantees of any published analysis $L_p$ algorithm and demonstrate the practical utility of the algorithm for a range of medical applications. Furthermore, we demonstrate that the computational cost of our algorithm is significantly lower than that of competing methods.

Our numerical tests focused on three challenging inverse problems : single image super-resolution, undersampled medical image reconstruction and image denoising. For single image super-resolution and for image denoising we demonstrate IAN's ability to outperform state of the art non-convex, convex ($L_1$) and gold standard algorithms both quantitatively and qualitatively. In each of the provided examples, IAN was used to enhance a clinically relevant pathological feature that can aid physicians in disease diagnosis and prognosis. We also demonstrate IAN's ability to recover undersampled MRI and CT images with greater quantitative and qualitative fidelity than competing non convex and convex methods. In doing so, we showcased IAN with TV's ability to circumvent the streaking artifacts common to undersampled CT reconstruction without sacrificing resolution. We also demonstrate that despite its non convexity, IAN can be used with well established methods for blind deconvolution. Finally, IAN's flexible algorithmic framework allows for examination of either the analysis or synthesis recovery problem. As such IAN's recovery can be tailored to the specific application under examination.

IAN as a methodology can be extended to a range of applications such as image inpainting, motion estimation and motion compensation. The use of complex dual tree double density wavelets as one of the components of a tight frame provides a natural framework within which motion estimation can be incorporated [57]. Image in-painting in its native

form, can be less ill-posed of an inverse problem than single image super-resolution which in turn makes IAN a viable solution framework. It is our contention that the generic formulation of the non-convex inverse problem which IAN solves ensures its generalizability to a wide variety of non medical applications (see Appendix).

Within the super-resolution context, temporal super-resolution provides an interesting avenue for future exploration. In video processing, it might provide for an avenue for artificially increasing the frame rate for higher perceptual video quality. In this application, the temporal dimension becomes dimension along which all operations are performed thereby freeing up spatial dimensions for independent and thus rapid parallel computation. IAN's flexibility with the choice of the $p$ norm, will allow for generation of spatially varying regions of high and low sparsity based on the tuning of the parameter $p$. This combined with the TV operator might provide for promising temporal super-resolution results in video processing.

In our numerical experiments with denoising spatially non uniform noise, we noticed the challenges with a global image denoising approach that IAN utilizes. IAN however can be trivially modified to handle large patch based denoising which in turn will allow for greater flexibility in compensating for spatially non uniform noise. Edge artifacts that occur with patch based processing can be overcome by using overlapping patches that can then be appropriately stitched at the boundary.

An alternative approach that might improve reconstruction accuracy at the cost of computational time is to asymptotically decrease the norm iteratively. Since IAN allows for the exact specification of the pseudo-norm, an iterative norm decrement from the standard $L_1$ norm to the desired $L_0$ norm might overcome the sensitivity to and result in a sparser solution. The challenge with this type of approach is the need to carefully quantify the relationship between the regularization parameter as a function of decreasing norm. This is necessary as a single regularization parameter might not prove to be optimal across all pseudo-norms.

Finally, while we were able to theoretically guarantee convergence, bounds on the number of iterations as a function of the warm start, the redundancy of the tight frame and the conditioning of the system are ideal avenues for future theoretical exploration.

# Part II

# Prospective Retooling

# CHAPTER 7
# INTRODUCTION

## 7.1 Overview and Innovation

Accelerated acquisition has long been a desirable goal in magnetic resonance imaging (MRI). Faster imaging directly translates to fewer motion artifacts, higher patient throughput and increased temporal / diffusion direction resolution for constrained imaging (fMRI, cardiac imaging, DTI). The current state of the art in hardware based accelerated imaging, Multiband Imaging (MB), seeks to deconvolve simultaneously excited slices by leveraging the diversity present in the encoding coils. However, the number of simultaneous slices that can be successfully deconvolved is limited by the intrinsic coil correlations along the slice direction. In this work, we develop a novel acceleration scheme (Advanced Pseudo Fourier Imaging: API) that is able to significantly reduce the inter coil dependencies and reconstruct the underlying signal with higher fidelity ($10-40\%$ lower reconstruction error) relative to MB. In addition, API is able to function at a much lower SNR regime for a fixed reconstruction accuracy as MB. Unlike MB, API is not dependent on non overlapping slice excitation. Finally, the API reconstruction framework is general and allows for seamless transition between 2D and 3D MR imaging.

## 7.2 Background

### 7.2.1 Whirlwind Review of Magnetic Resonance Signal Acquisition

When atoms with unpaired spins are placed in the presence of a magnetic field, these spins align either along or against the magnetic field. The difference in the population of spins in the lower energy (parallel) state versus the higher energy (anti-parallel) state is described

by

$$\frac{S_{high}}{S_{low}} \propto \frac{Nh\omega}{4\pi kT}$$

where $S_{high}$ is spins in the high energy state, $S_{low}$ is the spins in the low energy state, $N$ is the total number of spins in the sample, $h$ is Plank's constant, $k$ is Boltzman's constant, $T$ is the absolute temperature and $\omega$ is the larmor frequency [94, 95]. It is this spin excess that is of interest in MR(since any perturbation of the balanced spin population cancel each other out). Surprisingly, this spin excess is very small (on the order of $1$ in $1000000$ for a magnetic field strength of $0.3$T) [94].

These spins (both excess and otherwise), precess around their axes. This precession frequency is described by

$$\omega = \gamma B$$

where $\gamma$ is the gyromagnetic ratio, $B$ is the strength of the applied magnetic field in Tesla and $\omega$ is the Larmor frequency. Thus, with a population of spins to work with and a precession frequency that is a function of the applied magnetic field, we have the beginnings of an imaging framework. By utilizing spatially varying magnetic fields (gradients) that vary in all three dimensions, spatially coded spins can be generated(i.e. $\omega(x, y, z) = \gamma B(x, y, z)$. While these magnetic spins can be designed to be spatially varying, the system still does not have a measurable signal. A signal is generated by invoking the principle of resonance and Faraday's law of induction. By applying an electromagnetic wave with the same frequency as the precessing spins (which happens to fall with the radio-frequency spectrum), these spins can be tipped away from their natural equilibrium state. When this RF wave is removed, these spins now relax back to their equilibrium state. In the process of relaxation, an electro-motive force is generated in a receiver coil. It are these principles that form the bed rock of magnetic resonance imaging.

Integral to any discussion on MR, is the expression which governs the longitudinal and transverse magnetization. Post perturbation by an external RF pulse, the longitudinal magnetization ($M_z$) regains its equilibrium magnetization $(M_0)$ in the form of a decaying exponential

$$M_z(t) = M_0 \left(1 - e^{\frac{-t}{T_1}}\right)$$

where $t$ is time in seconds, $T_1$ is a constant that is determined based on the tissue being examined. It is a parameter that is heuristically determined for different tissues as the time instant at which the longitudinal magnetization has regained $63\%$ of its original magnetization. The transverse magnetization behaves in the exact opposite manner as the longitudinal magnetization and decays after the application of the RF pulse. The evolution of the transverse magnetization is described by

$$M_{x,y}(t) = M_0 e^{\frac{-t}{T2}}$$

where $T_2$ is also a tissue dependent constant. The observed signal (in the 3D case) can be written as

$$s(k_x, k_y, k_z) = \int\int\int \rho(x, y, z) e^{-(j2\pi k_x + j2\pi k_y + j2\pi k_z)} \text{ dx dy dz}$$

where $s$ is the observed signal with spatial frequency $k_x$, $k_y$, $k_z$ and $\rho(x, y, z)$ is the underlying spin density [94, 95]. Thus the signal obtained from an MR acquisition can be described as 3D fourier measurements of an unknown object $\rho(x, y, z)$. While $k_x, k_y, k_z$ are spatial frequencies, in the MR literature, they are known as points in k-space. These 3D spatial frequencies / k-space locations are described by the integral of the magnetic field

variations (gradients) applied along each dimension.

$$k_x(t) = \int_0^t \gamma G_x(\psi)\ \mathrm{d}\psi$$
$$k_y(t) = \int_0^t \gamma G_y(\psi)\ \mathrm{d}\psi$$
$$k_z(t) = \int_0^t \gamma G_z(\psi)\ \mathrm{d}\psi$$

where $G_x$, $G_y$, $G_z$ are magnetic field gradients applied along the $x$, $y$ and $z$ directions respectively [94, 95].

### 7.2.2 MR Acceleration Techniques

Acceleration techniques in MRI can broadly be categorized into methods that are data driven, assumption driven or hardware driven. Data driven methodologies, seek to fill in unacquired lines of k-space by learning the parameters of a data driven model from calibration scans. Assumption driven methods on the other hand, function by filling in unacquired lines of k-space based on broad assumptions about the underlying signal. Finally, hardware driven methods exploit advances in hardware design for accelerated acquisition. Each of these three categories along with representative methodological examples for each category are briefly summarized below for completeness.

Data driven methods such as GRAPPA [96] utilize calibration scans to determine the least squares optimal spatially invariant kernel to fill in the unacquired portions of k-space. At high acceleration factors (when large portions of k-space are undersampled), the assumption of a spatially invariant kernel fails resulting in artifact ridden recovery. Other data driven methods such as AUTO-SMASH and VD-AUTO-SMASH [97, 98] use calibration scans to determine model parameters for coil based pseudo-phase encoding. AUTO-SMASH and VD-AUTO-SMASH can achieve limited acceleration as they are intrinsically limited by a systems implicit coil phase [99].

Assumption driven methods restrict the underlying signal to a specific model / class

to reduce the amount of sampling required. Early work in this area began by exploiting the conjugate symmetry seen in the fourier transform of purely real signals. The method known as half fourier imaging acquires half of k-space and fills in the remaining half with the conjugate of the observed part of k-space [100]. This method was further improved upon by correcting for phase discrepancies and accounting for sampling pattern of k-space in [101]. Homodyne imaging, made further improvements by modifying the phase correction approach to included linear reweighting in k-space for improved reconstruction [102]. The reconstruction afforded by these methods are shown in Fig. 7.1. Modern assumption driven methods such as compressed sensing / low rank recovery [15, 103, 104, 105, 106, 107] make less restrictive assumptions. These modern methods assume that the underlying signal lives within a certain subspace that is known / can be reasonably assumed apriori. This assumption combined with randomized sampling provides a mathematical framework which can guarantee exact recovery of un-acquired k-space samples [5, 7, 6]. While theoretically sound, the practical constraints of randomized gradient switching reduces the acceleration factors that can be practically achieved with these methods.

The arena of hardware driven acceleration is most general. Acquisition strategies such as radial and spiral acquisitions [108, 109, 110] fall within this category. In radial and spiral acquisition, the phase encoding and readout gradients are continuously cycled to cover k-space in a non-cartesian trajectory (non uniform Fourier transform). While these types of k-space trajectories can be acquired in a shorter time relative to standard gradient echo cartesian sampling, the reconstruction process is more nuanced. The higher sampling density near the center of k-space must be accounted and compensated for in the reconstruction process to prevent the generation of sampling density artifacts. The most popular rapid acquisition methodology is that of Echo Planar Imaging (EPI) (originally introduced in [111]). EPI acquires all of 2D k-space in a single RF excitation at the cost of imaging resolution. On the hardware side, the gradient slew rate (the rate at which the magnetic field in each dimension can be altered) was a critical development for EPI. Hardware driven ac-

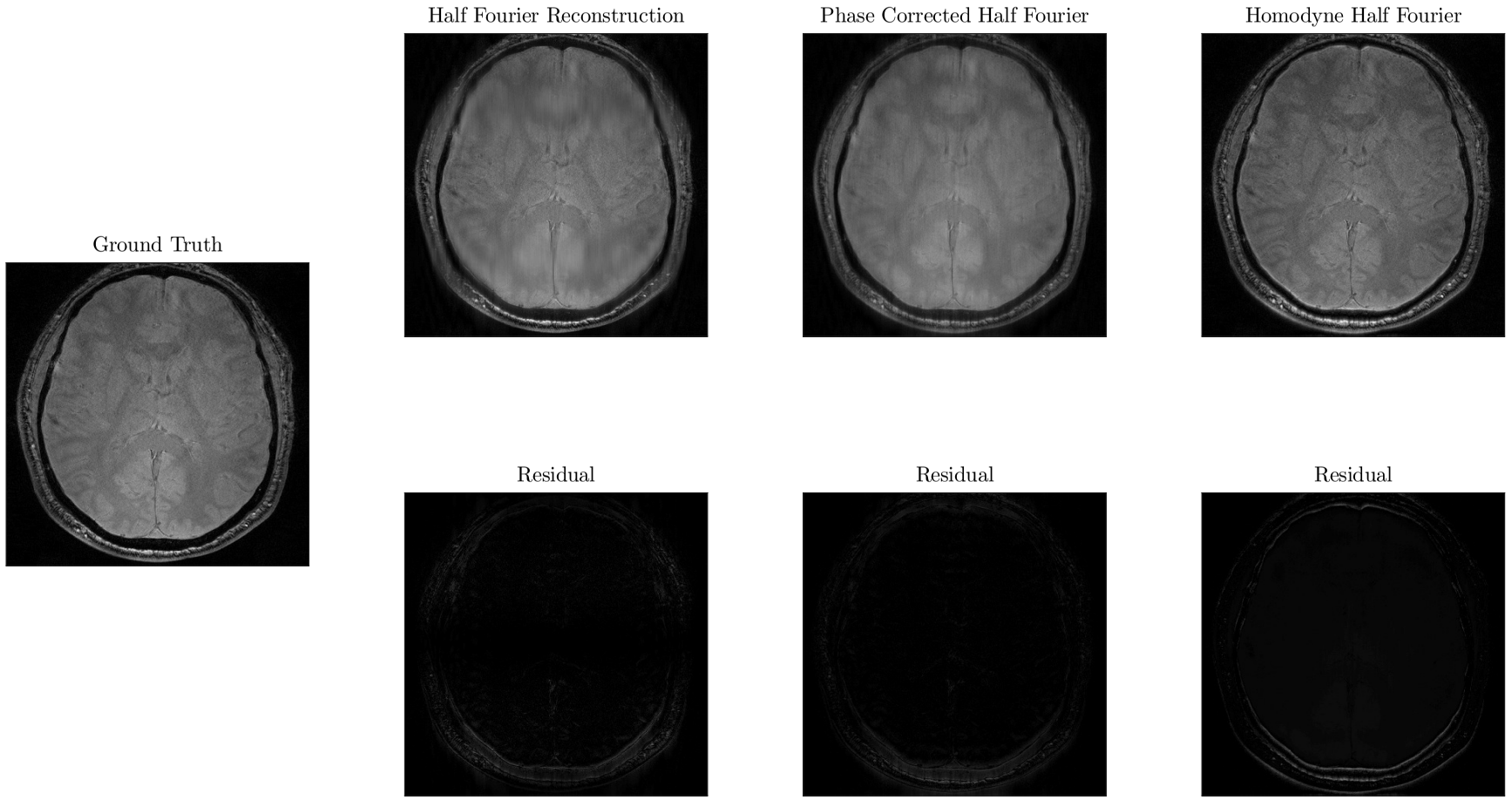


Figure 7.1: Exemplar reconstruction afforded by the half Fourier method methods in relation to the underlying ground truth. The half Fourier method with symmetric / antisymmetric weights is shown in the first column. The augmented half Fourier method with phase correction is shown in the middle column. The right column depicts the reconstruction afforded by the homodyne modification of the half Fourier method. It is clear that the residual error decreases from left to right an that the homodyne half Fourier reconstruction affords the best recovery of the half Fourier methods.

celeration methods gained the most attention in the literature with the advent of multiple receiver coils. Initial forrays into acquistion acceleration revolved around exploiting multiple coils to deconvolve periodic aliasing that occurs when undersampling is uniform [112]. This method termed SENSE, functions in the image domain where each observed pixel can be written as a linear combination of a few aliased pixels (provided the undersampling pattern in k-space is uniform). SENSE relies on having an over-determined system where the number of aliased pixels do not exceed the number of coils present in the system. A Shepp Logan phantom SENSE example is provided in Fig. 7.2. In practice, this methodology, while widely implemented, provides a maximum acceleration factor of $2-4$ on most MRI system. Furthermore SENSE is utilized as an in-plane acceleration technique and not a through-plane methodology.

*Simultaneous Multislice Excitation*

Recent advances in coil design and RF amplifiers have allowed for rapid simultaneous multislice excitation and subsequent deconvolution [113] : Multiband Imaging (MB). MB is the state of the art for accelerated imaging along the slice direction. Standard multiband imaging can be written as

$$B_k(x,y)_{(i)} = \int_z \hat{W}_k(x,y,z) c_i(x,y,z) f(x,y,z)\ \mathrm{dz}$$

where $\hat{W}_k(x,y,z)$ is the $k$th Excitation window, $c_i(x,y,z)$ is the $i$th coil and $f(x,y,z)$ is the function of interest. Consider $(f(x,y,z))$ fixed in space (i.e. fix $(x,y)$) then then each reconstruction block will have $I$ measurements (one for each coil). Multiband imaging suffers from intrinsic modeling error where $\hat{W}_k(x,y,z)$ is assumed to be a rectangular excitational pulse. This erroneous modeling decouples the reconstruction into a series of local deconvolutions which fails to consider slice overlap. Furthermore, such modeling, generates reconstructed profiles that are higher in signal magnitude than the true underly-

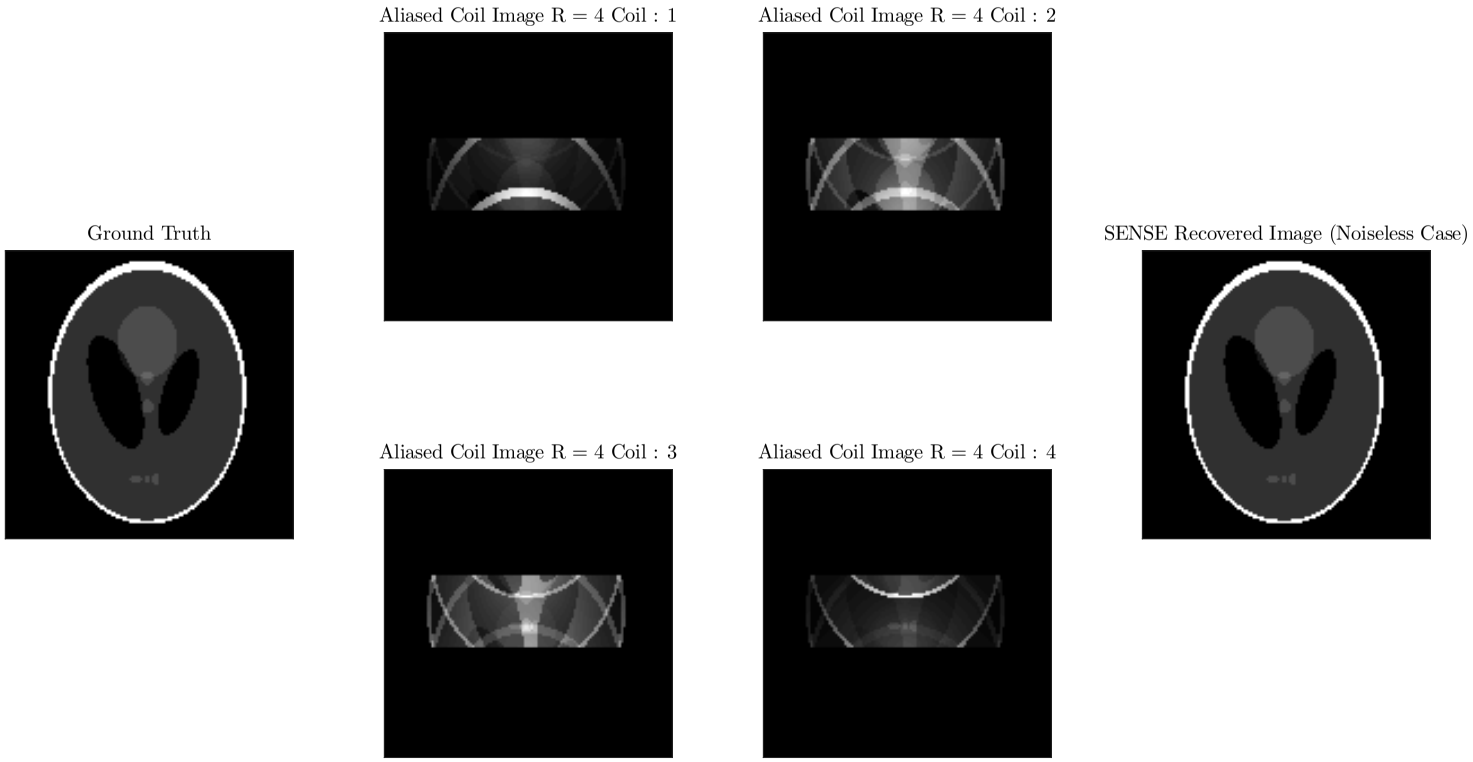


Figure 7.2: Exemplar reconstruction of a Shepp Logan phantom when uniformly undersampled by a factor of 4. The aliased signal seen at each coil is shown in the middle columns while the reconstruction afforded by SENSE is shown on the right. In the noiseless case and when the coil sensitivity profiles are known exactly, SENSE is able to recover the underlying signal perfectly.

ing signal. The multiband deconvolutional process begins to fail at high acceleration factors given the high dependence present between the coil elements [114, 115]. In the original pioneering multiband work [113] the authors were able to achieve successful deconvolution of 4 simultaneous excited slices at 7T. Recent advances [115] have allowed for the successful deconvolution of 8 simultaneous excited slices at 3T with a 32 channel coil.

In order to achieve these elusive higher acceleration factors, various methods have been employed to ensure successful deconvolution at higher acceleration factors. In [116] the authors propose a method titled controlled aliasing in parallel imaging results in higher acceleration (CAIPIRINHA). This method induces phase difference between the phase encoding lines in the frequency encoding - phase encoding plane (in plane) to ensure that overlapping slices exploit different portions of the in plane coil sensitivity profile. This phase difference was applied by inducing a constant phase on an applied RF pulse from one phase encode line to the next thereby restricting its application to non gradient recalled echo sequences. Furthermore, this method is predicated on high in plane coil variability. In [117], the authors use through plane gradient blips to introduce phase variations in plane. This method called blipped-CAIPI allows for the generalization of CAIPIRINHA to echo planar imaging sequences. However at high acceleration factors this method begins to trade off in plane and through plane acceleration thereby limiting how fast the system can be accelerated [117]. In [118] the authors focus on augmenting standard GRAPPA reconstruction for multiband imaging by altering the optimization strategy used to determine GRAPPA weights. They demonstrate that the augmented methodology reduces inter slice leakage artifacts. This method while useful in ensuring higher fidelity reconstructions does not improve multiband acceleration factors.

An interesting technique (which we generalize and extend in this work) is that of Pseudo Fourier Imaging [119]. This technique, originally built for a single coil (channel) systems, focused on developing smooth boundaries between adjacent slices to enhance signal recovery in applications which required smooth boundaries. This form of smooth transition

between slices was achieved using a though plane phase encode that is commonly utilized in volumetric imaging. As such, PFI can be thought of as a hybrid imaging technique that analytically varies on a continuum between 2D and 3D imaging. This technique while elegant, was not formulated to tackle the multislice deconvolution problem nor to handle the multiple receiver coils. Furthermore, the reconstruction method employed invoked inverting the spectral profile of the windowing kernel which can prove to be unstable when dealing with spectral singularities.

In this work, we draw inspiration from PFI to generate a new metholology API. API, unlike PFI, is designed to handle multiple receiver coils and function in the multislice deconvolution case. The reconstruction approach forms a generalized framework for seamless transition from 2D-3D imaging without inversion challenges common to PFI. API by construction, decorrelates the reciever coils. This allows for robust / higher acceleration recovery relative to multiband imaging while also overcoming the challenges that MB imaging has with non overlapping excitation. We demonstrate the viability of the API method with both 1D simulations (along the slice direction) and with retrospective reconstruction of data acquired on a 3T Prisma scanner. In both instances, we are able to definitively demonstrate a $10 - 50\%$ decrease in reconstruction error relative to MB imaging.

# CHAPTER 8

# METHODS

Multiband imaging [120, 115, 118, 114, 113], the current state of the art in accelerated MR imaging, excites multiple slices (in place of a single slice excitation) and subsequently deconvolves these slices to recover the object being imaged. This deconvolution leverages the sensitivity profiles of the coils used to acquire the data. Our method, API also invokes multislice excitation but provides for additional degrees of freedom in the form of phase variations along the slice direction. These phase variations are practically introduced by controlled magnetic field fluctuations along the slice direction. By doing so, we move away from the static phase variations present in multiband imaging and introduce dynamic phase modulations. This provides an additional layer of control in the design of the encoding operator. The added benefit of this framework is in its ability to smoothly transition from 2D - 3D thereby forming a generalized reconstruction and excitation approach.

## 8.1 1D and 3D Mathematical Framework

Mathematically, we can write multiband imaging as

$$B(x,y)_{(k,i)} = \int_z \hat{W}_k(x,y,z) c_i(x,y,z) f(x,y,z) \text{ dz}$$

where $\hat{W}_k(x,y,z)$ is the $k$th Excitation window, $c_i(x,y,z)$ is the $i$th coil, $f(x,y,z)$ is the function of interest and $B(x,y)_{(k,i)}$ is the observed signal at location $(x,y)$ at the $k$th excitation for the $i$th coil. Here the multislice excitation is obfuscated in the term $\hat{W}_k(x,y,z)$. To explicitly include the acceleration factor $R$ (number of simultaneous excitations), we

can decompose the windowing function into a linear sum of each excitation band.

$$\hat{W}_k(x, y, z) = \sum_{r=1}^{R} \hat{W}(x, y, z - \delta_{k,r})$$

where $\delta_{k,r}$ are shifts indexed based on the excitation and $\hat{W}(x, y, z)$ is the excitation window primitive. Then the multiband model becomes

$$B(x, y)_{(k,i)} = \int_z \left( \sum_{r=1}^{R} \hat{W}(x, y, z - \delta_{k,r}) \right) c_i(x, y, z) f(x, y, z) \, \mathrm{dz}. \tag{8.1}$$

The API model on the other hand can be written as

$$b(x, y)_{(k,i)} = \int_z w_k(x, y, z) c_i(x, y, z) f(x, y, z) e^{-j\omega_k z} \, \mathrm{dz},$$

where $w_k(x, y, z)$ is the $k$th Excitation window, $c_i(x, y, z)$ is the $i$th coil, $f(x, y, z)$ is the function of interest and $b(x, y)_{(k,i)}$ is the observed signal at location $(x, y)$ at the $k$th excitation for the $i$th coil. Incorporating a similar breakdown of the $k$th excitation window into shifts of a primative, we can write

$$b(x, y)_{(k,i)} = \int_z \left( \sum_{r=1}^{R_p R} w(x, y, z - \zeta_{k,r}) \right) c_i(x, y, z) f(x, y, z) e^{-j\omega_k z} \, \mathrm{dz}, \tag{8.2}$$

where $\zeta_{k,r}$ are shifts indexed based on the excitation and $R_p$ is the repeat factor (number of times a single location is seen). The additional degrees of freedom arise in the picking of $K$ phase encodes $\omega_k$ and the setting of the repeat factor $R_p$. The differences between the multiband model and the proposed model (API) are easy to see when Eq. 8.1 and 8.2 are compared. The number of excitation bands $R_p R$ versus $R$, the utilization of excitation windows which are closer to the underlying physics $\hat{W}(x, y, z)$ versus $w(x, y, z)$ and the application of phase variations $\omega_k$ are the differences that set the proposed method (API) and multiband apart. The use of $\hat{W}(x, y, z)$ is the source of multiband's seperable recon-

struction (since excitation profiles have no overlaps i.e. $\langle \hat{W}_p(x,y,z), \hat{W}_q(x,y,z) \rangle_z = 0$ for $p \neq q, p, q \in 1, 2, \ldots, K$). This non overlap assumption lies in opposition to the physics of excitation. Notice that as the repeat factor is increased, the number of simultaneous excitations also increase. This was done to ensure that API was given the same measurement budget as multiband. A schematic of multiband imaging [113] versus our method (API) is shown in Fig.8.1.

Since the acceleration for both methods is along the slice direction, a 1D simulation along the slice direction is an indispensible first step. All operators used in our simulation had analytic closed forms to stay true to the analog to discrete conversion that occurs during data acquisition on an MR scanner. The operators were carefully designed to stay true to the underlying physics of excitation profiles and expected electromagnetic variations in coil sensitivities. We begin by considering any orthobasis $\{\psi_n(x,y,z)\}_{n=1}^{\infty}$ that spans the space of interest. Then we can write the function of interest $(f(x,y,z))$ as

$$\begin{aligned} f(x,y,z) &= \sum_{n=1}^{\infty} \underbrace{\langle f(x,y,z), \psi_n(x,y,z) \rangle}_{\alpha_n} \psi_n(x,y,z) \\ &= \sum_{n=1}^{\infty} \alpha_n \psi_n(x,y,z). \end{aligned}$$

Using this in the API framework (Eq. 8.2) we get

$$\begin{aligned} b(x,y)_{(k,i)} &= \int_z w_k(x,y,z) c_i(x,y,z) \sum_{n=1}^{\infty} \alpha_n \psi_n(x,y,z) e^{-j\omega_k z} \, \mathrm{dz} \\ &= \sum_{n=1}^{\infty} \int_z w_k(x,y,z) c_i(x,y,z) \psi_n(x,y,z) e^{-j\omega_k z} \alpha_n \, \mathrm{dz}. \end{aligned}$$

When the basis are not orthogonal (but are linearly independent), the same argument holds except that the basis coefficients $\alpha_n$ must be computed differently. In this instance, the fact that the basis matrix $(\Psi)$ has a left inverse can be utilized to show that $\alpha_n = \langle f(x,y,z), \hat{\psi}_n \rangle$ where $\hat{\psi}_n$ is the $n$th row of the matrix $\hat{\Psi} = \left(\Psi^T \Psi\right)^{-1} \Psi^T$. For the 1D

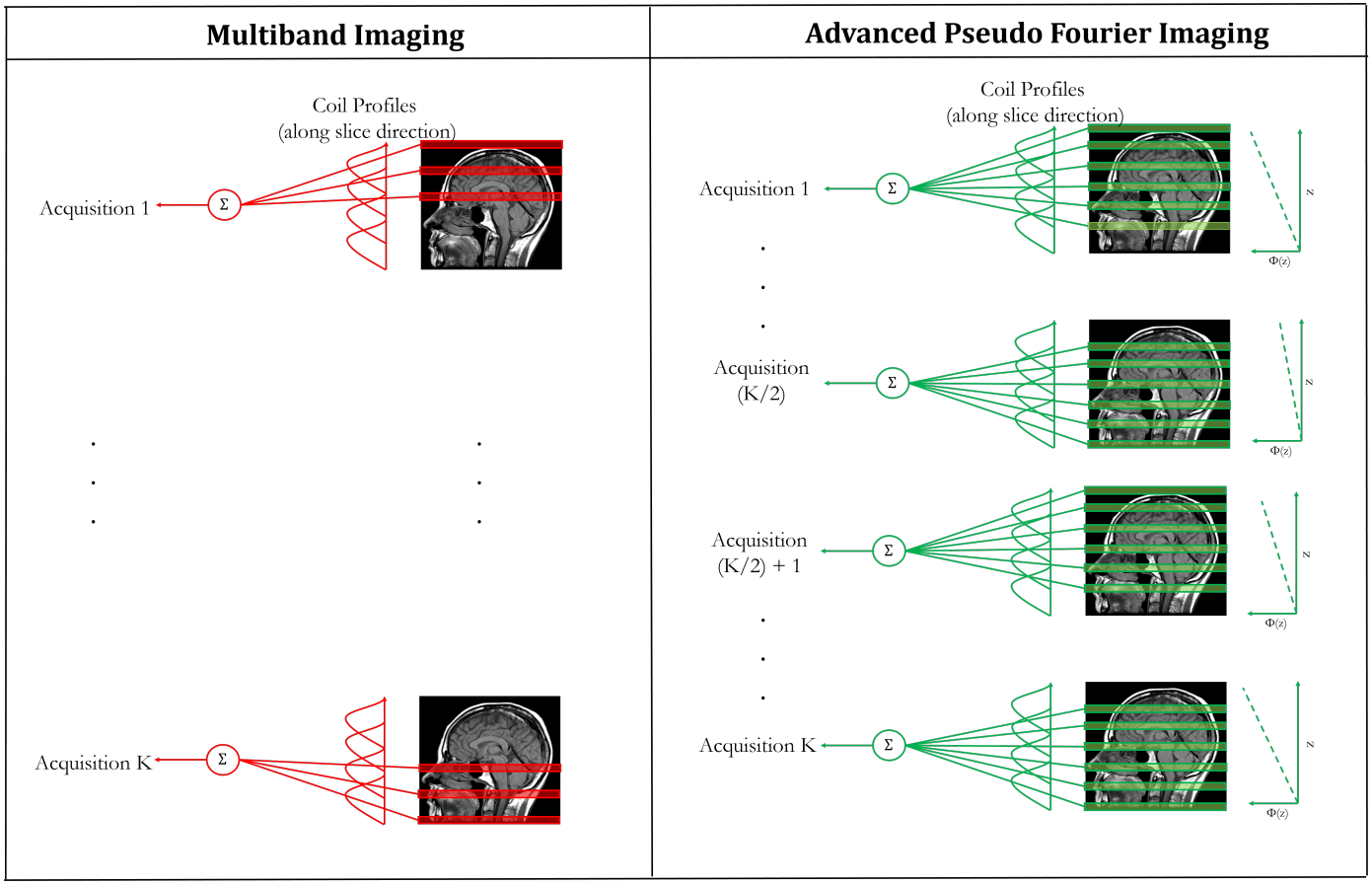


Figure 8.1: Schematic of multiband imaging versus the proposed advanced pseudo-Fourier imaging (API). Both techniques utilize a budget of K excitations but in this example, API simultaneously excites twice the number of slices thereby allowing for two views of each slice with different phase encodes. Furthermore, individual API windows can be flexibly designed to be twice as large as their MB counterparts. The phase encoding is changed per excitation to allow for greater control over the spectral behavior of the forward measurement operator.

simulation results shown here, a b-spline basis was used.

Without loss of generality, we can consider the one dimensional case along the $z$ direction. This gives us

$$b_{(k,i)} = \sum_{n=1}^{\infty} \int_z w_k(z) c_i(z) \psi_n(z) e^{-j\omega_k z} \alpha_n \, \mathrm{dz}.$$

Let $m$ be the index which defines the ordered pairs of $(k, i)$. Then if we have a finite $N$ term basis decomposition we can write the encoding matrix elements as

$$a[m, n] = \int_z w_k(z) c_i(z) \psi_n(z) e^{-j\omega_k z} \, \mathrm{dz},$$

where $M = KI$. The resulting encoding operator: $\boldsymbol{A} \in \mathbb{C}^{(M \times N)}$, coefficient vector: $\vec{x} \in \mathbb{C}^{(N \times 1)}$ and observed signal: $\vec{b} \in \mathbb{C}^{M \times 1}$ form a linear inverse system. This form of formulation where $b$ is computed using the entire basis expansion / analytic function while $a[m, n]$ is computed using the finite number of basis is vital to avoid the inverse crime [121]. To further clarify the difference between multiband and API determination where the total number of excitation $K$ are kept constant, we can define

$$K = \left( \frac{S}{R} \right) R_p,$$

where $S$ is the number of desired slices, $R$ is the number of simultaneous excitations and $R_p$ is repeat factor (number of times a slice is seen). For multiband imaging by definition $R_p = 1$

### 8.1.1 Slice Direction : Excitation Windows

The RF excitation pulses used for slice excitation are apodized sinc pulses (sinc pulses convolved with hamming windows to prevent gibbs ringing artifacts). This modeled by a

Tukey window has the form

$$w(z) = \begin{cases} \frac{1}{2}\left(1 + \cos\left(\frac{2\pi}{\alpha}(z - \frac{\alpha}{2})\right)\right) & 0 \leq z < \frac{\alpha}{2} \\ 1 & \frac{\alpha}{2} \leq z < 1 - \frac{\alpha}{2} \\ \frac{1}{2}\left(1 + \cos\left(\frac{2\pi}{\alpha}(z - 1 + \frac{\alpha}{2})\right)\right) & 1 - \frac{\alpha}{2} \leq z < 1 \end{cases}$$

This gives rise to slice excitation which mimic true MR RF excitation with some adjacent slice excitation. Then for $R$ simultaneous excitations with a total of $K$ windows, each $w_k(z)$ can be easily defined to be the sum of $R$ shifted and scaled version of $(z)$. Overlap between windows can be controlled by placing window centers either closer or further apart. In order to better understand the differences between the two methodologies, we plot the composite windows (i.e. windows + phase encodes) for a single excitation as utilized in MB and API. The composite windows used for the first multiband excitation is shown in Fig.8.2 while the windows used for the first API excitation is shown in Fig.8.3. A trivial comparison of Fig. 8.3 and Fig. 8.2 reveals the additional diversity injected into the encoding process by API composite windows. The phase encoding used in the API method can be viewed from two different but equally valid perspectives. First, the phase encodes can be thought of as coil recalibration. In this view, the phase encodes take these static coil profiles (intrinsic to an MR system) and provides an avenue to control how correlated these coils remain relative to the their native state. Viewed from a different perspective, the phase encodes can be seen as adding diversity to the measurement operator (i.e. the excitation windows). This is clearly seen in composite window plots of Fig .8.3 and Fig. 8.2.

### 8.1.2 Slice Direction : Coil Sensitivities

Next, we model the coil sensitivity profiles using the Biot Savart law,

$$B(z) = \frac{\mu_0}{4\pi} \int_C \frac{IdL \times \vec{m}}{\|m\|^2},$$

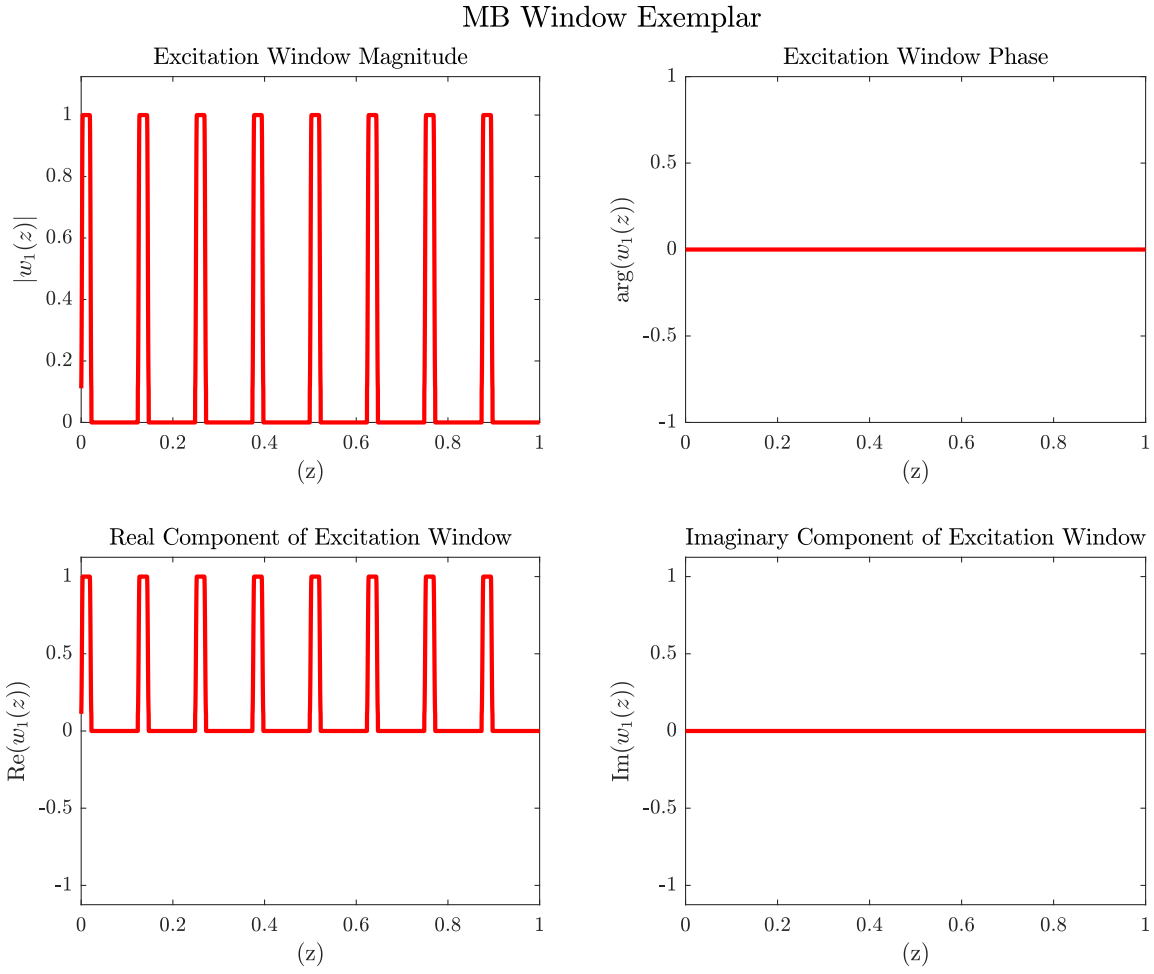


Figure 8.2: Composite windows (windows + phase encoding) used for multiband excitation $k = 1$. The magnitude, phase, real and imaginary parts of these composite windows are plotted for an acceleration factor of 8. The composite excitation windows are purely real with no phase and no imaginary component since MB does not utilize phase encoding along the slice direction.

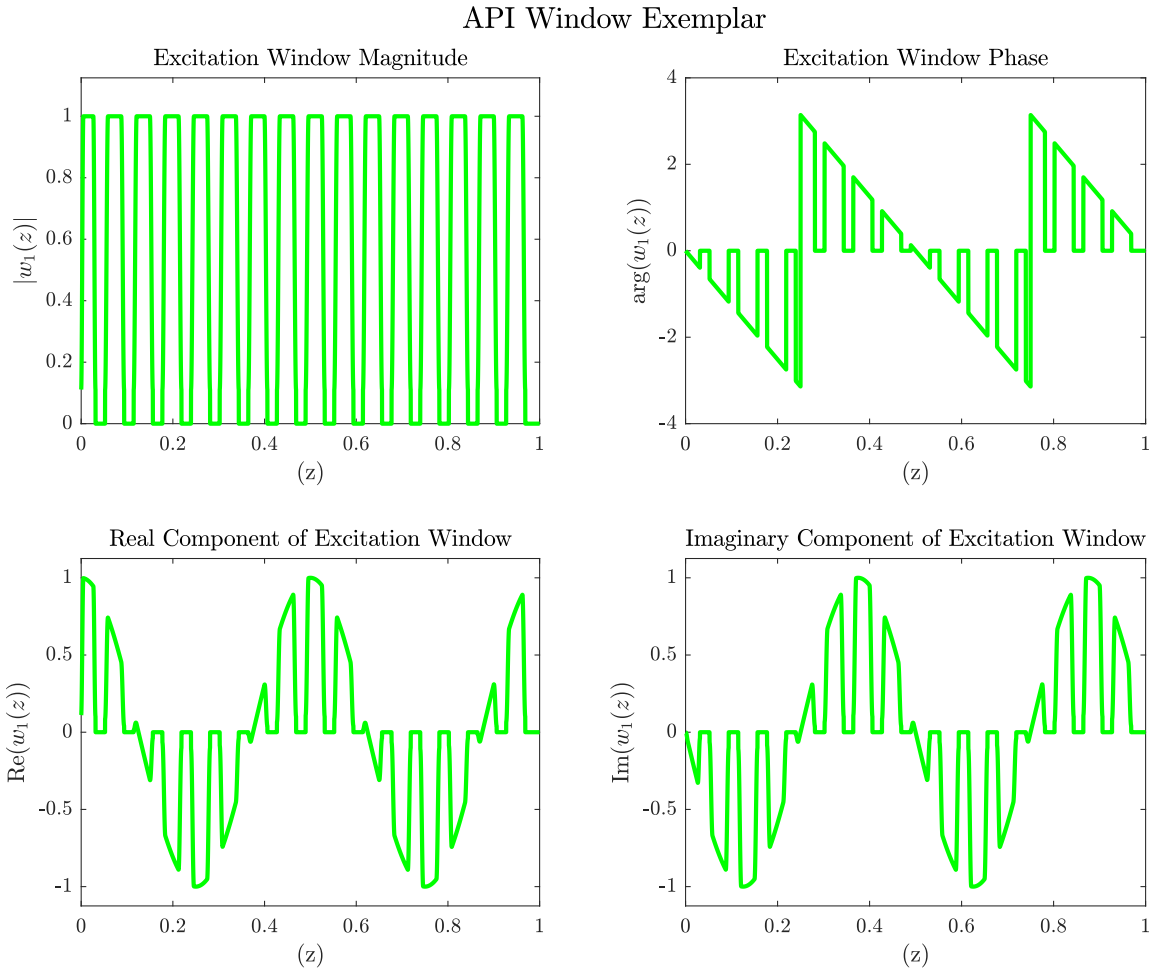


Figure 8.3: Composite windows (windows + phase encoding) used for API excitation ($k = 1$).The magnitude, phase, real and imaginary parts of these composite windows are plotted for an acceleration factor of 8. Notice that API has 16 active support regions to compensate for the utilization of an extra phase encode. The real and imaginary components of the API windows are windowed versions of modulated sinusoids.

where $\mu_0$ is the permitivity of free space, $dL$ is the vector pointing from one coil element discretization to the next, $\vec{m}$ is the vector pointing from the point of computation $z$ to $dL$. The computation of these coil sensitivities for an exemplar circular coil is shown in Fig. 8.4. The magnitude and phase of each of the 12 coils is shown in Fig. 8.5.

### 8.1.3 Slice Direction: Analytic Functional Form

The analytic function had the following form

$$f(z) = \left( \sum_t a_t e^{\frac{(z-\mu_t)^2}{b_t^2}} + \sum_q \delta(z - z_q) \right) e^{-j\pi z},$$

where $a_t$, $\mu_t$, $b_t$ and $z_q$ are constants. $\delta(z)$ is the impulse function. This formulation gives $f(z)$ spatial discontinuities which result in a spectral profile that has both low and high frequency content. The level high frequency perturbations can be controlled by setting $t$ and $q$ to the desired levels. The function used for the 1D simulations is shown in Fig. 8.6

## 8.2 Phase Encodes

Critical to the success of the API methodology is the picking of appropriate phase encodes. When dealing with a least squares framework, the success of the recovery is dictated by the spread of the singular values. The singular values can be visualized as a metric which depicts how much of the range space is truly reachable. Thus an ideal spectrum would be completely flat. While minimizing the nuclear norm (sum of the singular values) is a convex problem [122], maximizing the nuclear norm is not.

The strategy utilized for picking phase encodes for the 1D case was to run a monte carlo simulation. At each iteration, a random set of phase encodes was picked and the nuclear norm was computed. This was repeated for a fixed number of iterations and the phase encodes which resulted in the largest nuclear norm was picked. It must be noted that to add structure to the problem, two constraints were added. First, the set of all possible phase

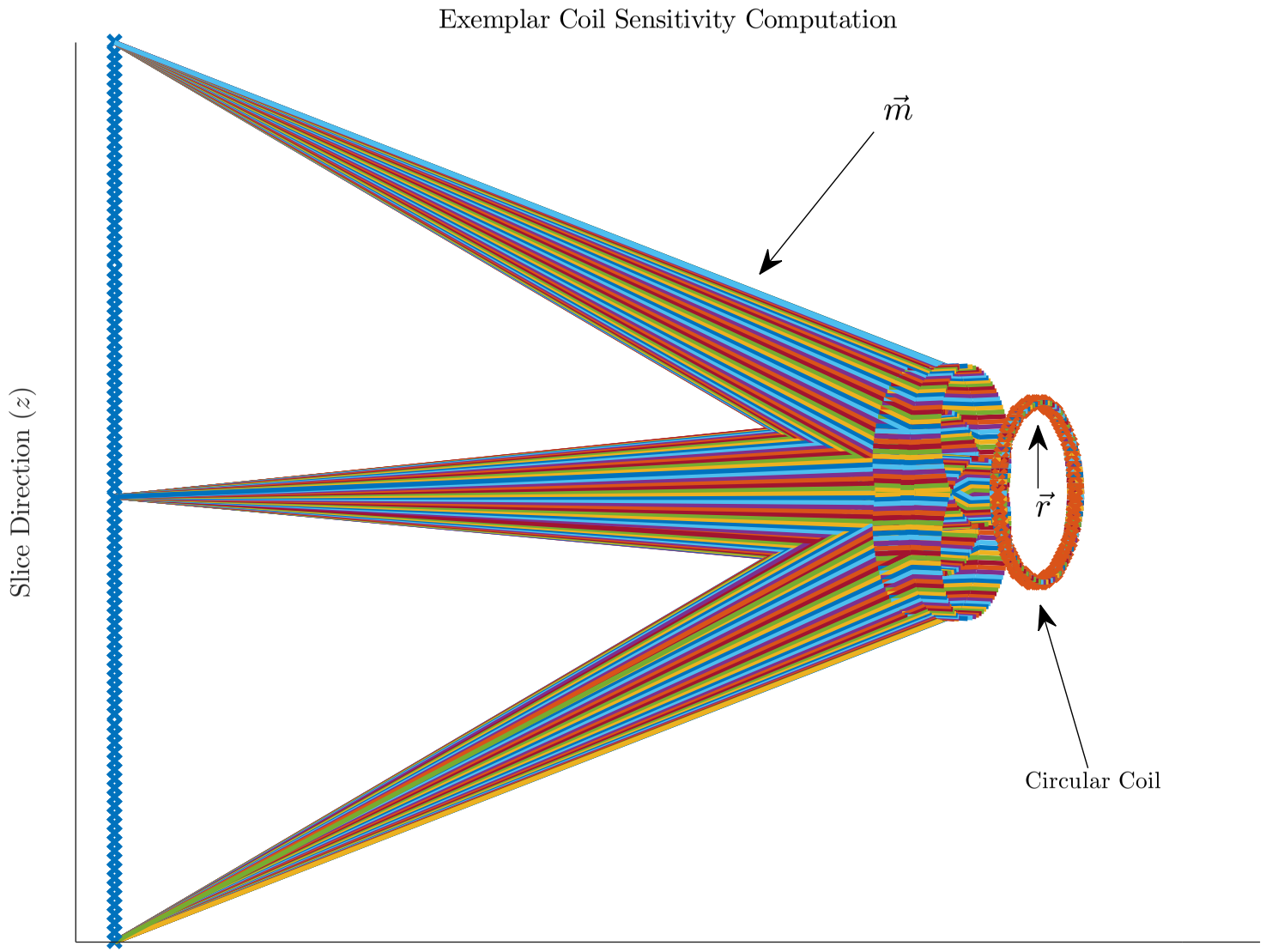


Figure 8.4: Exemplar computation of coil sensitivities for a single circular coil along the slice direction. The vector element $dL$ points from one coil discretization to the next. The vector $\vec{m}$ points from each location in the slice direction to each coil element. The coil has radius $r$.

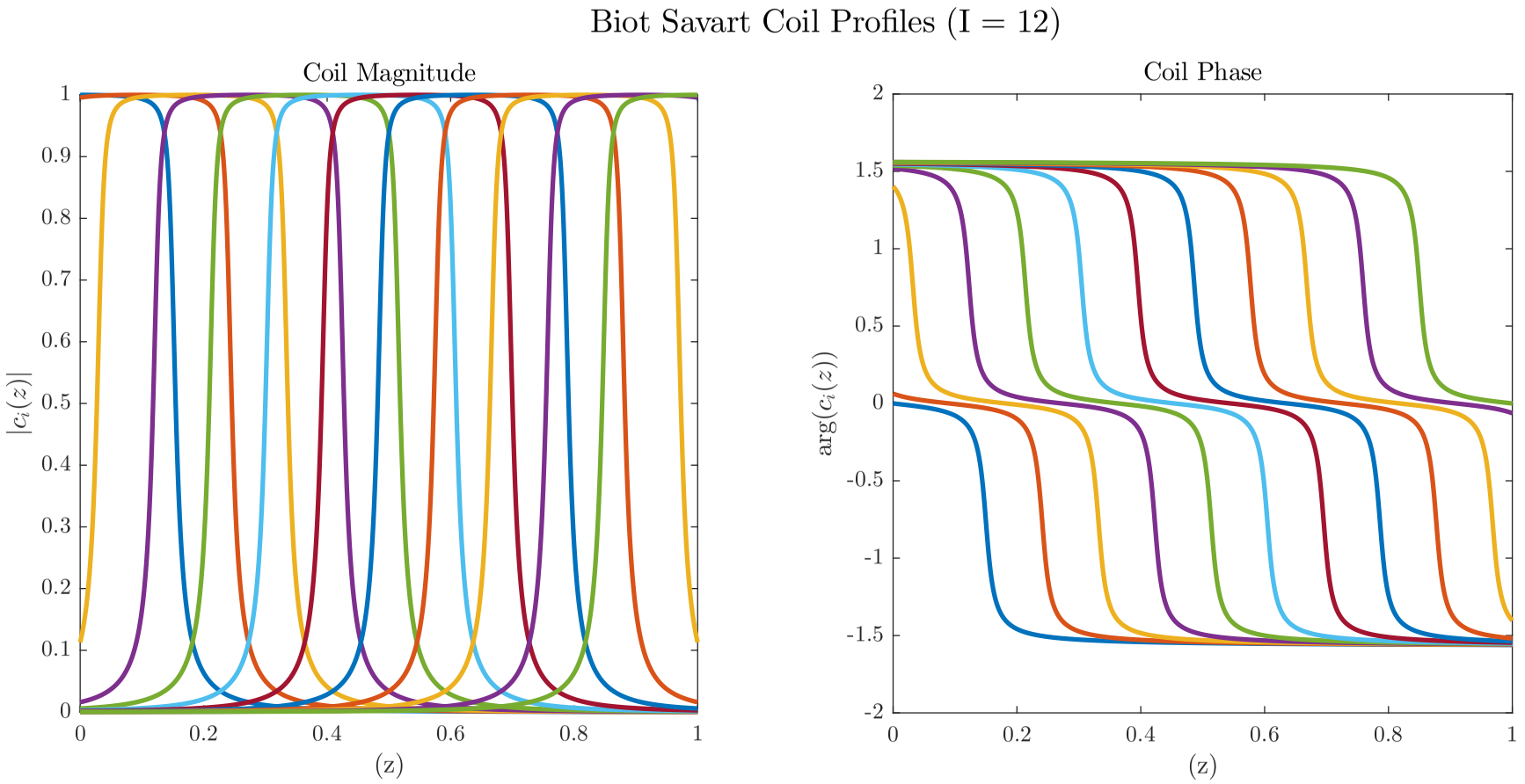


Figure 8.5: Magnitude and phase of $I = 12$ coils computed using the Biot-Savart law. Each coil has a localized region of active support along the slice direction with significant overlap between the sensitivities of each coil.

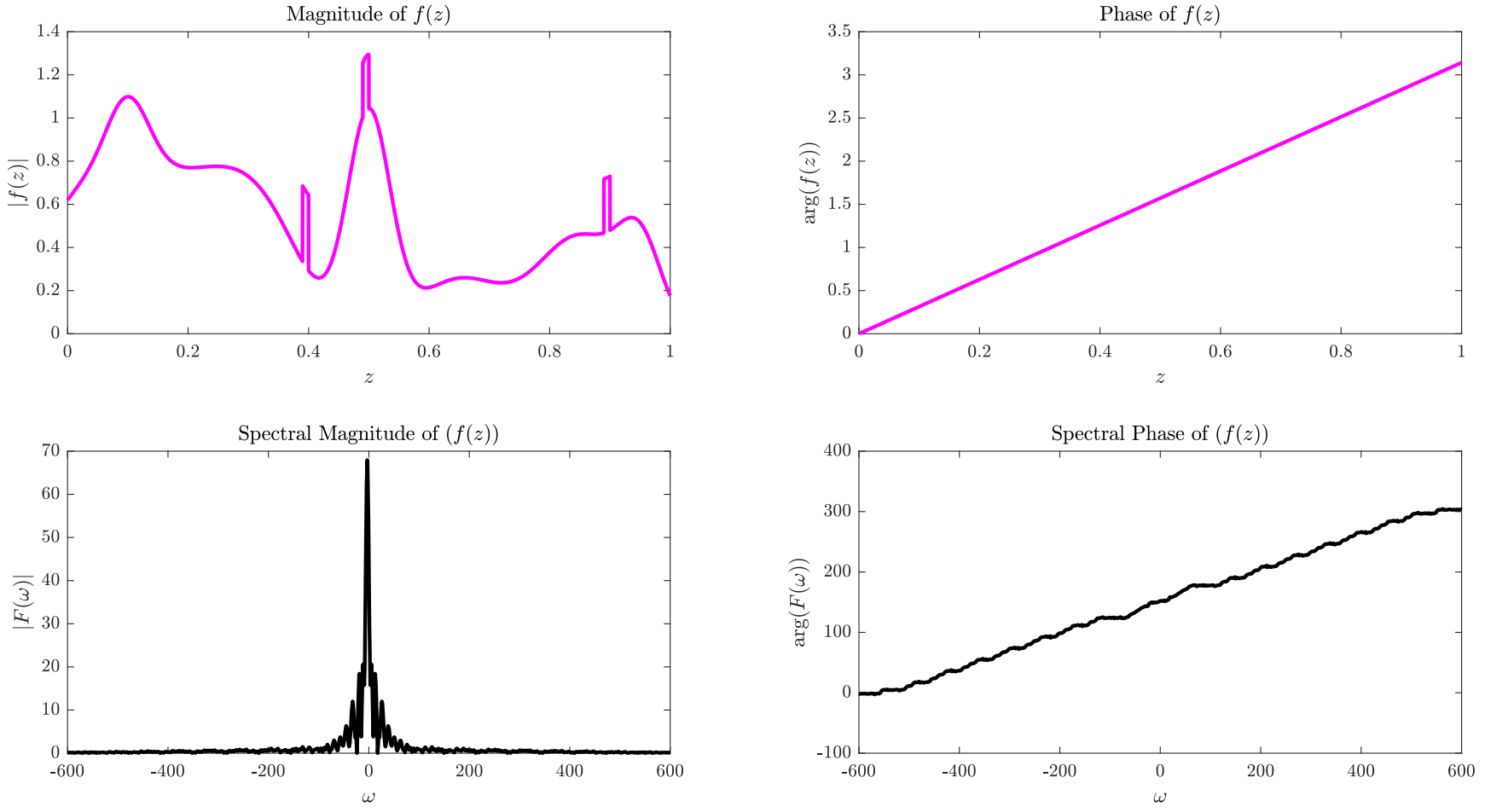


Figure 8.6: Spatial and spectral profile of the analytic function used in our 1D simulations. The spatial discontinuities control the level of high frequency content.

encodes was restricted to low frequency values. An alternate way to view the API problem is to consider that we are attempting to deconvolve the sum of a series of windowed fourier transforms. Since a majority of the signal's energy is concentrated in the low frequency region, sampling these regions provide us with the most amount of information. Second, when each location is sampled the second time (for repeat factors of 2), the phase encodes from the previous sampling of the same location were sign flipped. Doing so ensures two looks at the real (even) part of the signal with opposite sign examinations of the imaginary (odd) part of the signal.

In the 3D case, the same process was repeated but instead of examining the nuclear norm of the operator for every in-plane location, a randomized set of 2 in-plane locations were selected. One location was randomly selected from the periphery (where the coil profiles are sharp) while the second location was randomly chosen from the interior (where the coil profiles are broad). The same low frequency and sign flip constraints were applied in the 3D case as well.

### 8.3 3D Signal Recovery

For the 3D simulations, data from a head phantom was acquired on a Siemens $3$T Prisma Fit (Malvern, PA) using a gradient echo sequence with a flip angle of $30^{\circ}$, pixel bandwidth of $30$ Hz, TE of $18.5$ msec, TR of $38$ msec, FOV of $158 \times 390 \times 198$mm and resolution of $1 \times 1 \times 2$mm. The 3T Prisma scanner coil profiles were extracted for the acquired data. The excitation windows were used also as the recovery basis for these 3D simulations. Phase gradient and multi-slice excitations were implemented retrospectively for ground truth comparisons with the final reconstruction. The excitation windows for API and multiband were identical in the recovery framework unlike the 1D case.

## 8.4 Signal Recovery Optimization

In order to ensure a fair comparison, multiband was augmented using the same forward model as API (no modeling error), joint recovery in place of localized recovery and Tikhonov regularization. The intrinsic optimization framework then is the well know $L_2$ regularized recovery

$$\hat{\alpha} = \min_{\alpha \in \mathbb{C}^N} \|\boldsymbol{A}(\vec{\alpha}) - \vec{b}\|_2^2 + \lambda \|\vec{\alpha}\|_2^2. \tag{8.3}$$

The recovery accuracy was quantified using normalized error:

$$e(\vec{x}, \hat{x}) = \frac{\|\vec{x} - \hat{x}\|_2^2}{\|\vec{x}\|_2^2}$$

where $\vec{\alpha}$ is the basis expansion coefficients of $f(z)$ in the basis of choice, $\hat{\alpha}$ is the recovered basis coefficients and $\vec{x}$ is the underlying ground truth signal as represented in the basis of choice. The recovered signal can be trivially computed as $\hat{\vec{x}} = \sum_{i=1}^{N} \hat{\alpha}_i \psi_i$. In the 3D case, the same $L_2$ recovery framework presented in Eq. 8.3 was used. Since the recovery is separable across each in-plane location, the optimization problem in Eq. 8.3 was parallelized for rapid computation.

### 8.4.1 Regularized Conjugate Gradient

It must be noted however, that if more sophisticated models are developed which account for in-plane signal leakage, then the problem will no longer be separable across each in-plane location. This lack of separability combined with the large dimensionality of the problem (3D volume of size $256 \times 256 \times 128$ for an acceleration factor of $16$ with $50$ coils will have an encoding matrix with dimension $\boldsymbol{A} \in \mathbb{C}^{26214400 \times 8388608}$) will render analytic solutions inpractical to compute. Instead, scalable methods such as conjugate gradients [123] must be utilized to handle the increased dimensionality of the problem (for

an excellent introduction to conjugate gradients see [124]). Since the method of conjugate gradients was original designed for the $L_2$ case, the optimization problem presented in (8.3) must be trivially modified to handle the Tikhonov regularizer. The new optimization problem becomes

$$\hat{x} = \min_{x \in \mathbb{C}^n} \left\| \begin{bmatrix} \boldsymbol{A} \\ \lambda \boldsymbol{I} \end{bmatrix} \vec{x} - \begin{bmatrix} \vec{y} \\ \vec{0} \end{bmatrix} \right\|_2^2 \tag{8.4}$$

.

This allows us to solve the Tikhanov regularized recovery using conjugate gradients at the cost of increasing the dimensionality of the encoding operator $\boldsymbol{A}$ and the measurement vector $\vec{y}$.

# CHAPTER 9

# RESULTS

In this chapter, in order to demonstrate the viability of the API methodology, we present signal recovery in three scenarios. First, we examine the recovery afforded in the $R = 8$ for the 1D simulation that was discussed earlier. Next, we examine the recovery in the 1D case when the acceleration factor is increased to its theoretical limit ($R = I = 12$). Finally, we consider the API methodology in the 3D case where the underlying data and coil profiles are scanner based.

## 9.1 Acceleration Factor $R = 8$

In Fig. 9.1, relative recovery error is plotted for MB and API across a range of noise profiles (R = 8). If a relative recovery error threshold of 0.2 is set, then it becomes clear that API is able to recover the underlying signal when SNR is $> 5$dB while multiband requires an SNR of $> 17$dB. This factor of 3 difference in SNR requirement for a fixed recovery error is a reflection of the robustness that is afforded by the API methodology. While Fig. 9.1 depicts recovery seen across multiple noise instantiations, a single representative example is shown in Fig. 9.2. The magnitude and phase recovery for MB and API for matched SNR ($23.51$ dB) is shown in Fig. 9.2. API recovers the underlying signal with nearly $50\%$ less error relative to MB. API, unlike MB is not handicapped in its choice of windows. For the recovery shown in Fig. 9.1-9.2, the API windows were twice as large as their MB counterparts. Visually, the differences between the reconstruction afforded by each method is trivial to observe. The benefits afforded by API span both the magnitude and phase of the recovered signal. The difference in recovery afforded by the two methods in the 1D simulation case can be better understood by examination of Fig. 9.3. The 1D API encoding operator has a larger area under the curve relative to the MB encoding operator.

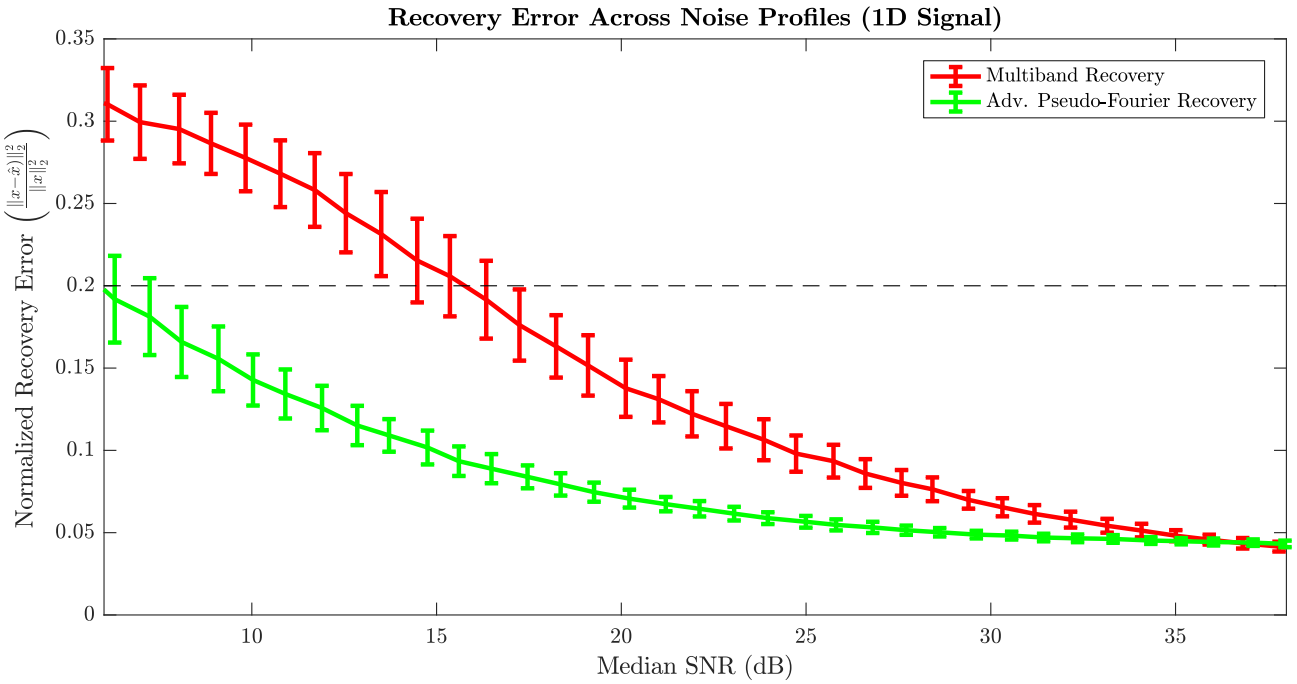


Figure 9.1: Recovery error for API and MB when $R = 8$ using biot-savart coil sensitivities across a range of noise profiles for signal recovery along the slice direction for a fixed location. It becomes clear that API is able to recover the underlying signal with greater fidelity relative to MB fair. The improvement in recovery error is on the order of $10\% - 50\%$. If a relative error of 0.2 is set as the threshold for acceptable recovery, it is clear that API recover the underlying signal with an SNR as low as 5dB. MB on the other hand can only meet the acceptable recovery standard at an SNR that is a factor of 3 higher than that of API at approximately 17 dB. The error bars depict one standard deviation away from the median recovery error.

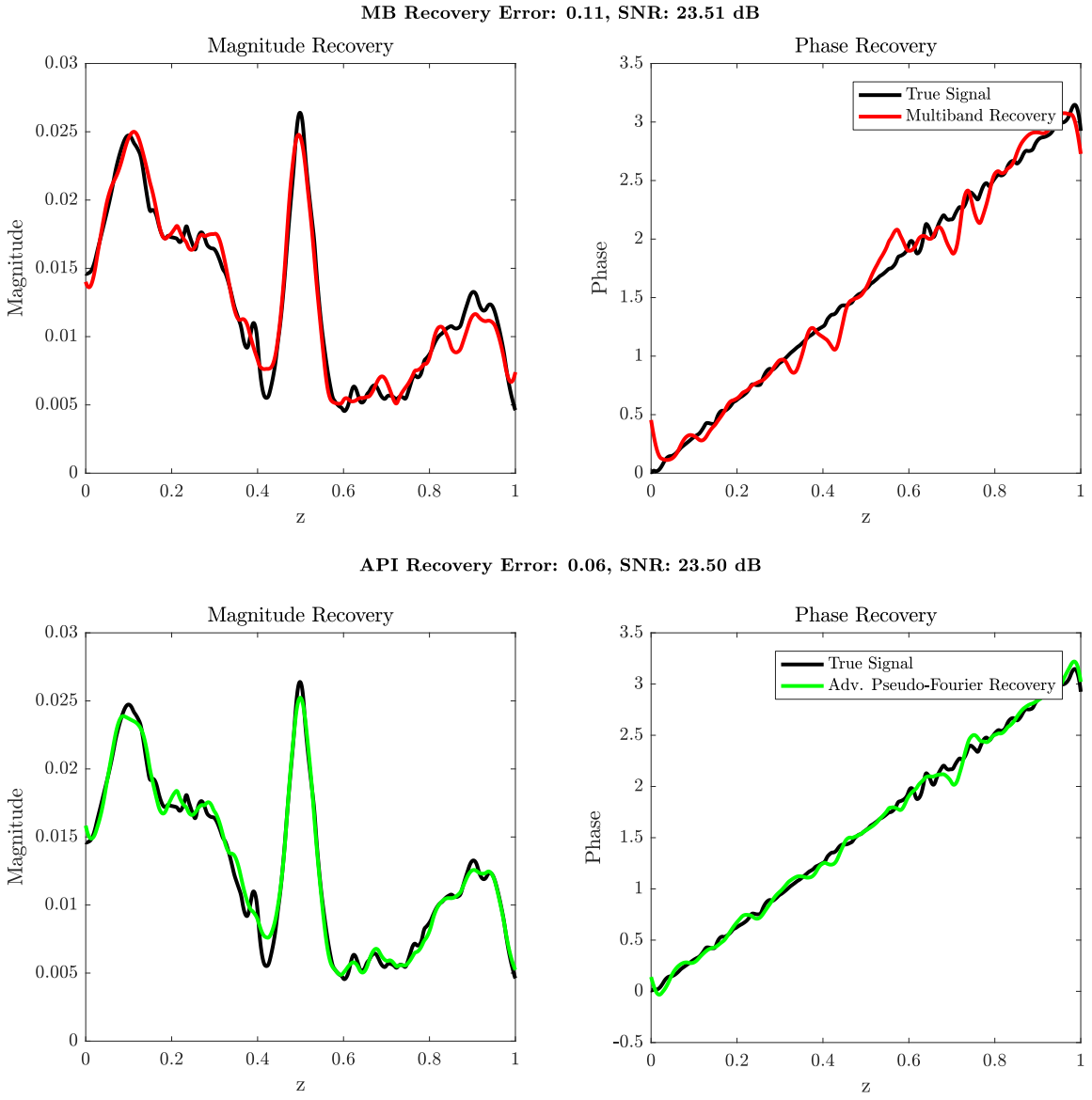


Figure 9.2: Exemplar magnitude and phase recovery for Multiband (top row) and API (bottom row). The true signal is shown in black, the signal recovered by multiband in shown in red and the signal recovered by API is shown in green. For R = 8 and I = 12, a SNR matched recovery exemplar is shown. In the plotted example, at an SNR of 23.51dB, API has nearly a $50\%$ reduction in recovery error. In this example, while API and MB operated on the same measurement budget, API utilized excitation windows that were twice as large as the windows used for MB.

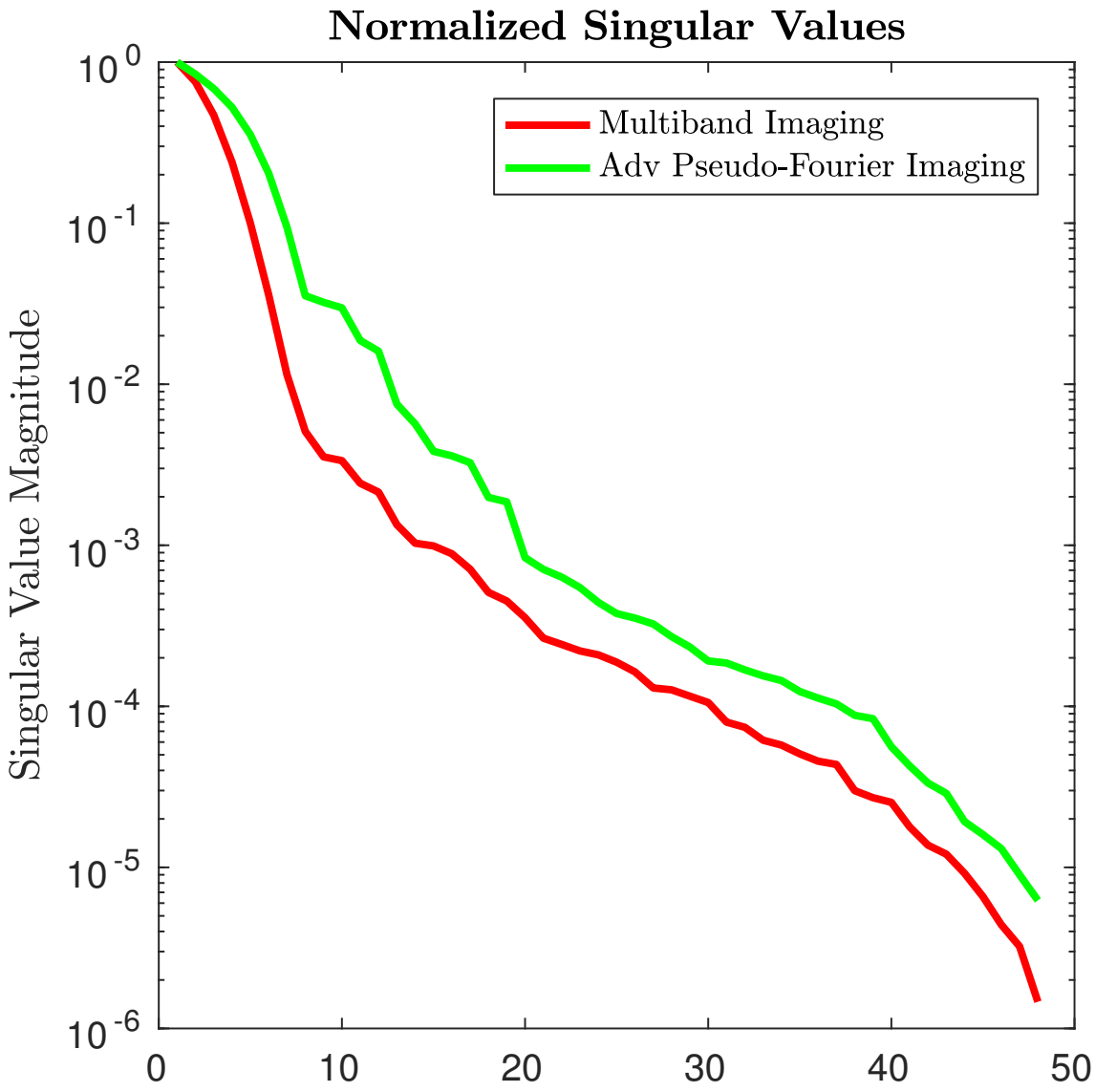


Figure 9.3: Normalized spectral distribution of 1D MB and API operators for $R = 8$. The API operator spectrum has a larger area under the curve relative to the MB operator spectrum.

## 9.2 Acceleration Factor $R = 12$

In Fig. 9.4, relative recovery error is plotted for MB and API across a range of noise profiles for a higher acceleration factor than the previous section (R = 12). If the same recovery error threshold of 0.2 is set for acceptable recovery, then it becomes clear that API is able to recover the underlying signal when SNR is $>$ 7dB while multiband requires an SNR of $>$ 23dB. Even at this higher acceleration, the same factor of 3 difference in SNR requirement for a fixed recovery error is seen as in the $R = 8$ case. A single representative recovery example is shown in Fig. 9.5. The magnitude and phase recovery for MB and API for matched SNR ($34$ dB) is shown in Fig. 9.5. API recovers the underlying signal with nearly $40\%$ less error relative to MB. As in the $R = 8$ case, the API windows were twice as large as their MB counterparts. Visually, the differences between the reconstruction afforded by each method is trivial to observe. The benefits afforded by API span both the magnitude and phase of the recovered signal. The difference in recovery is to be expected when the spectral profile of the encoding matrices are examinated (see Fig. 9.6). The API encoding operator has a larger area under the curve relative to the MB encoding operator.

## 9.3 3D Recovery $R = 8$

In the 3D case, Fig. 9.7, API recovers the underlying signal with approximately $40\%$ lower error relative to MB despite operating under a lower SNR ($30.26$ dB versus $31.52$ dB) for an acceleration factor of 8. A cursory examination of the recovery reveals sparser residuals for each API recovered slice relative to MB recovered slices. The entire 3D reconstruction set for all 112 slices is provided for completeness in Appendix B. As in the 1D case, the API encoding operator for the examined locations (Fig. 9.8) has a spectral distribution with a greater area under the curve relative to the MB encoding operator.

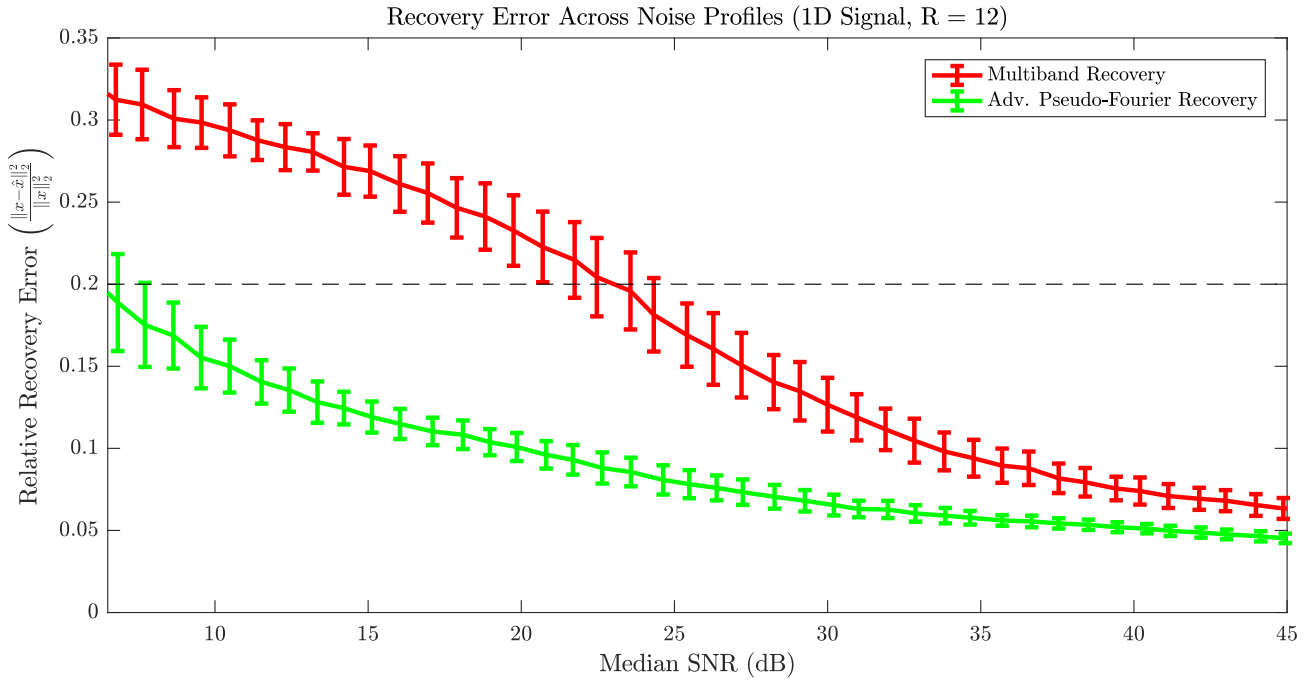


Figure 9.4: Recovery error for API and MB when R = 12 across a range of noise profiles for signal recovery along the slice direction. It becomes clear that API is able to recover the underlying signal with greater fidelity relative to MB fair. The improvement in recovery error is on the order of $10\% - 50\%$. If a relative error of 0.2 is set as the threshold for acceptable recovery, it is clear that API recover the underlying signal with an SNR as low as 7dB. MB on the other hand can only meet the acceptable recovery standard at an SNR that is a factor of 3 higher than that of API at approximately 23 dB. The error bars depict one standard deviation away from the median recovery error.

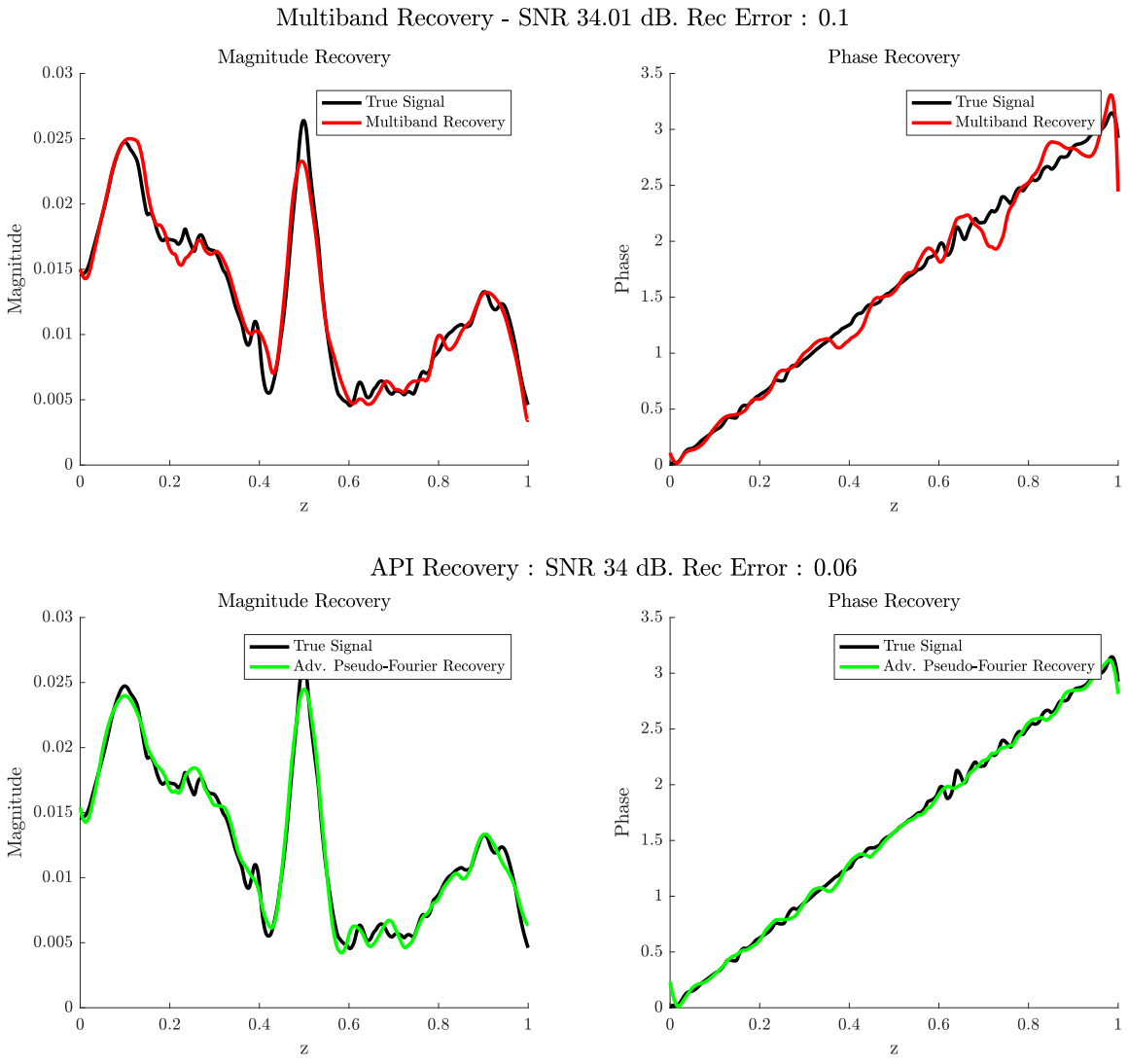


Figure 9.5: Exemplar magnitude and phase recovery for Multiband (top row) and API (bottom row). The true signal is shown in black, the signal recovered by multiband in shown in red and the signal recovered by API is shown in green. For R = 12 and I = 12, a SNR matched recovery exemplar is shown. In the plotted example, at an SNR of 34dB, API has nearly a $40\%$ reduction in recovery error. In this example, while API and MB operated on the same measurement budget, API utilized excitation windows that were twice as large as the windows used for MB.

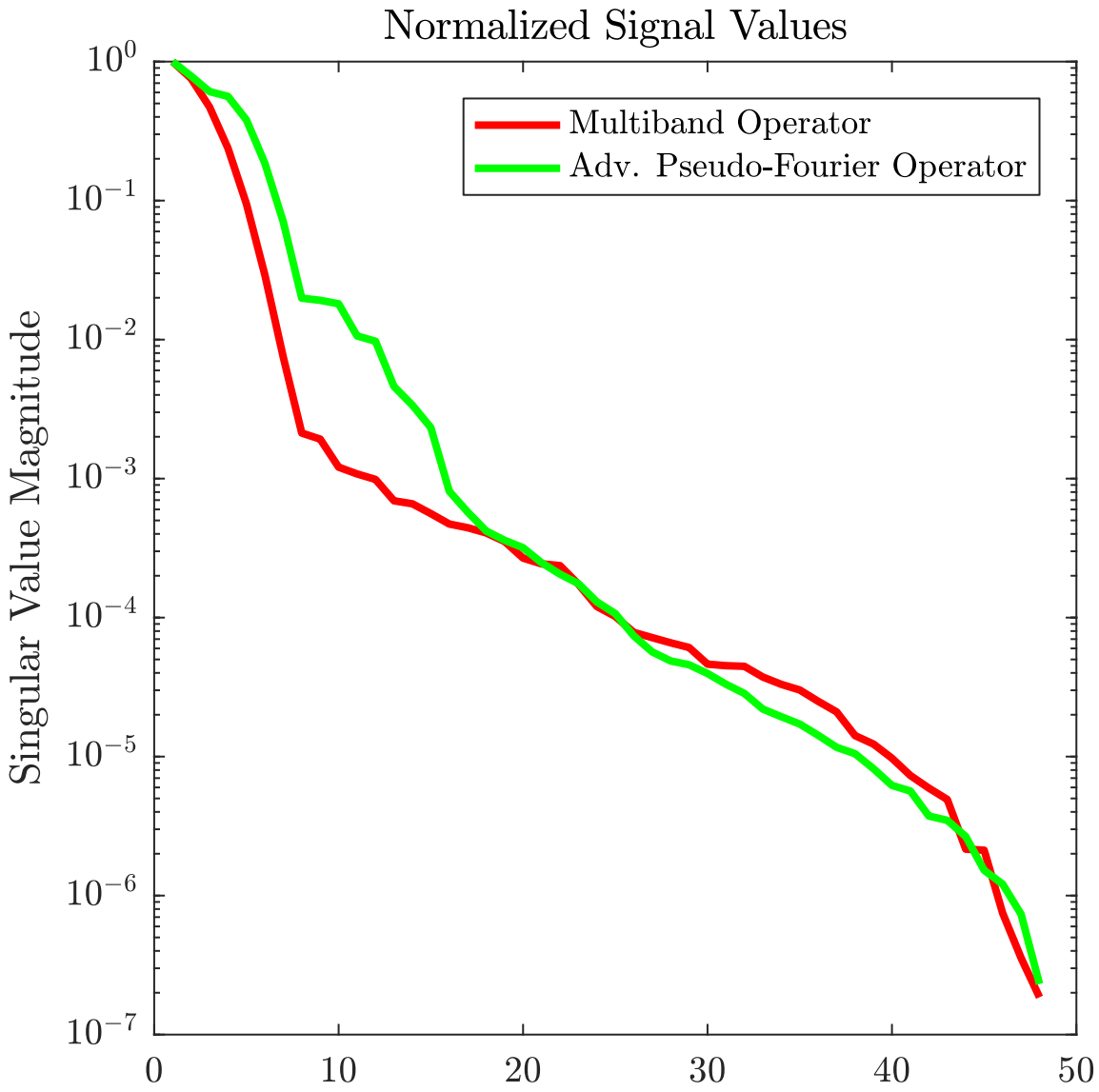


Figure 9.6: Normalized spectral distribution of 1D MB and API operators for $R = 12$. The API operator spectrum has a larger area under the curve relative to the MB operator spectrum.

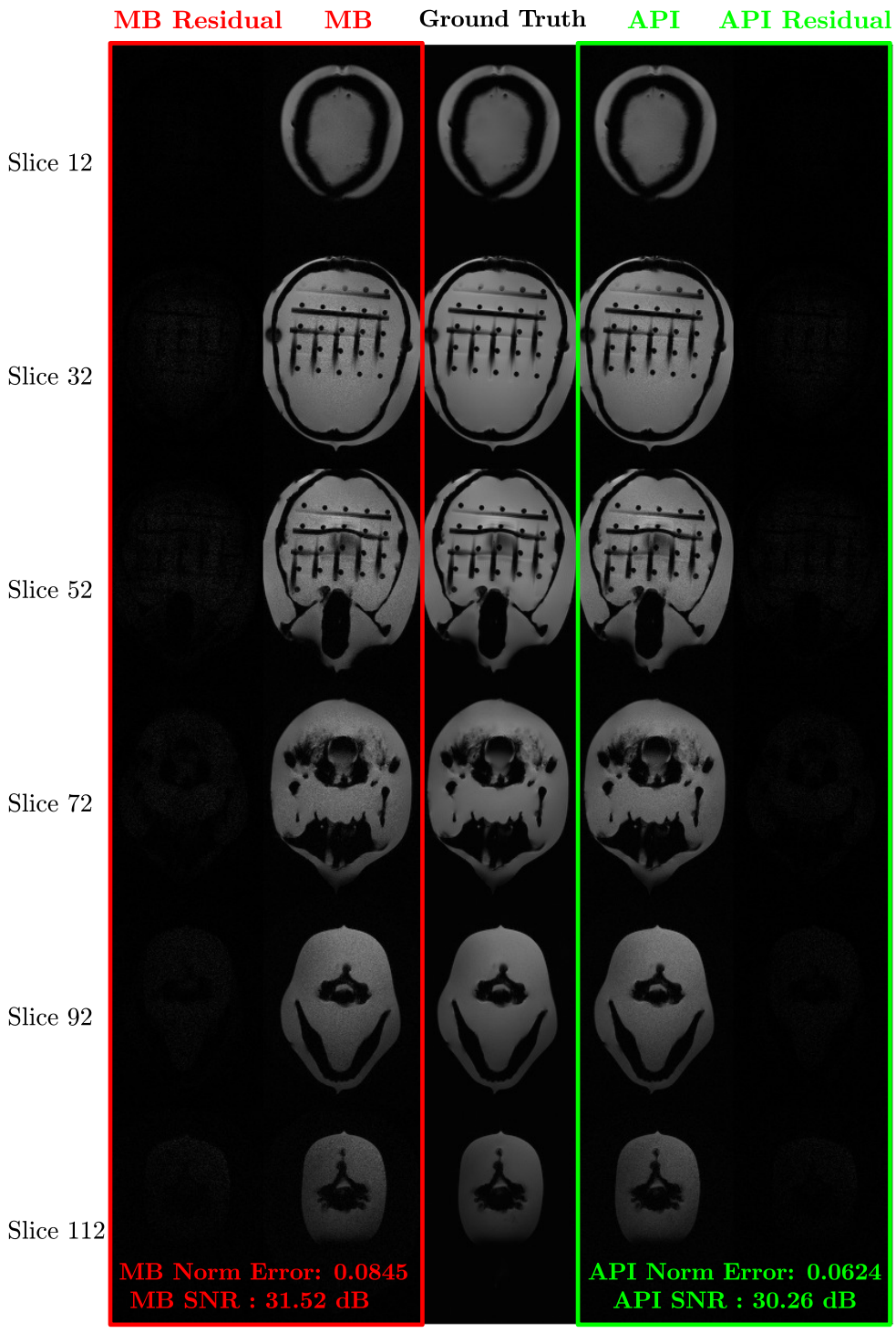


Figure 9.7: 3D Recovery exemplar for MB (red box) and API (green box) for single noise instantiation (R = 8). 6 slices are plotted along with the underlying ground truth and residuals for each method. For the example shown, the SNR for MB was $31.52$ dB while that for API was $30.26$ dB. Despite the lower SNR, API reconstructs the underlying signal with approximately $37\%$ lower error $(0.0624)$ versus MB's $(0.0845)$.

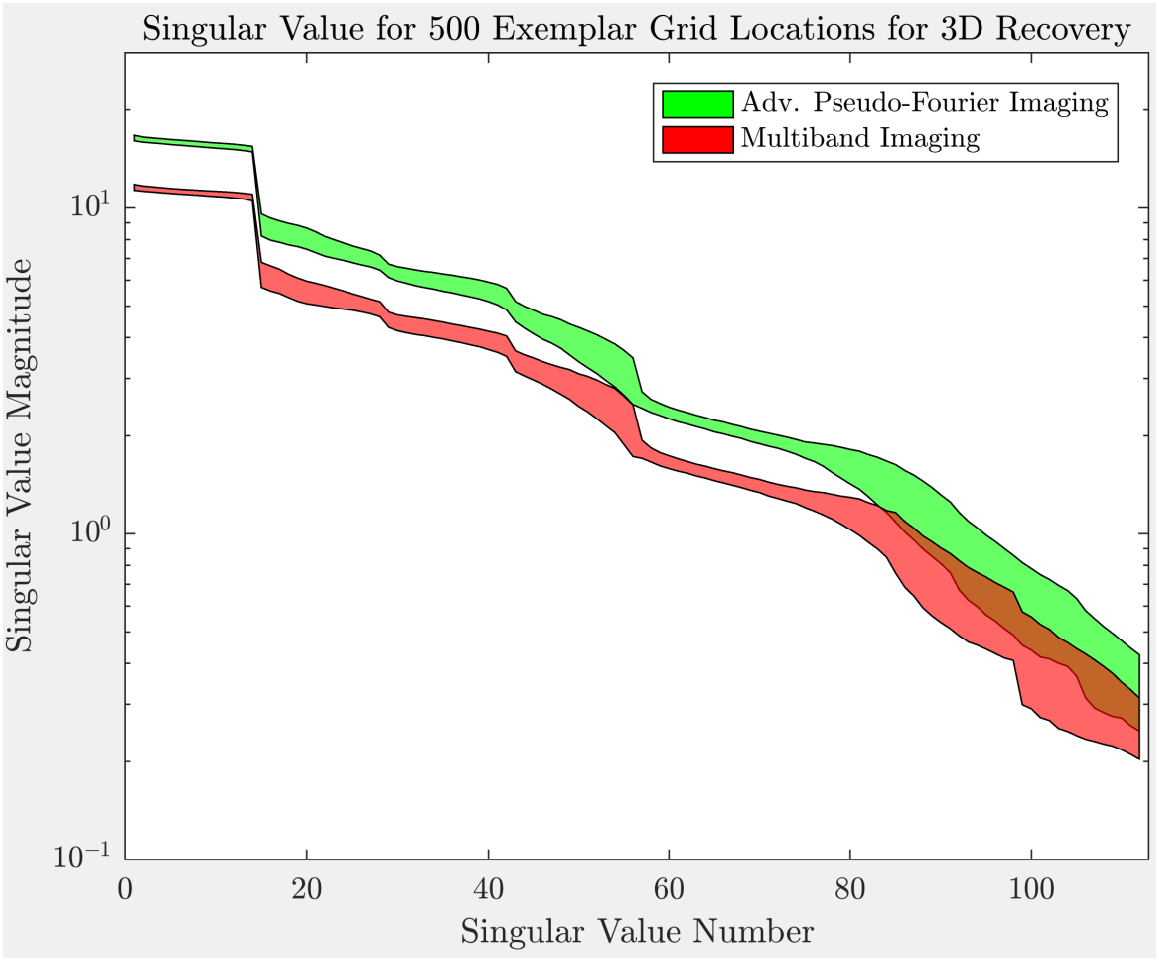


Figure 9.8: Spectral distribution for 500 exemplar in plane locations for 3D MB and API operators. The spectrum plotted for each operator is the median $+/-$ 1 standard deviation from the median. The API operator spectrum has a larger area under the curve relative to the MB operator spectrum as in the 1D case.

# CHAPTER 10

# DISCUSSION

From the results presented, it becomes clear that API outperforms MB across a range of noise profiles at an acceleration factor at which MB traditionally fails ($R = 8$). More intriguing however is the performance of both methods when acceleration is increased to the theoretical limit ($R = I = 12$). A cursory comparison of Fig. 9.1 and Fig. 9.4 demonstrates that API recovery error does increase at the higher acceleration factor but the increase is minimal relative to multiband's increase in recovery error. This is best examined by considering the median recovery at a fixed signal to noise ratio for $R = 8$ and $R = 12$. If we consider an SNR of $25$dB, API's median recovery error is $\approx 0.06$ for $R = 8$ and $\approx 0.0725$ for $R = 12$. For MB recovery at the same SNR, the median recovery error is $\approx 0.1$ for $R = 8$ and $0.175$ for $R = 12$. For an increase in acceleration by $4$, API's recovery error only increases by $21\%$. MB's recovery error on the other hand, increases by $75\%$. In short, API is able to robustly recover the underlying signal at high acceleration factors. The higher the acceleration factor, the further apart API and MB grow.

API's ability to accurately recover the signal at $R = I = 12$ is of perticular interest given that the acceleration factor is at its theoretical limit (i.e. the number of coils). A cursory examination of Fig. 8.5 demonstrates that the $12$ coils used in the simulation had significant spatial overlap. In fact, a single coil's spatial support can be seen to intersect with the spatial support of $3$ other coils (i.e. a single coil overlapped with as much as $25\%$ of all the coils in the system). This form of coil overlap is at the core of why MB fails at high acceleration factors. Thus API's success at this high acceleration factor is a reflection of the ability of the API methodology to increase the diversity of the measurement operator for robust recovery. This is addressed in the next section.

The robustness of the API methodology is further demonstrated by the success of the 3D

recovery shown in Fig. 9.7. The chasm between the 1D simulation and 3D results is deep. Consider that in the 1D case, when looking at the coil profile for a single in-plane location $(x^*, y^*)$ it is conceivable that $K$ linear phase encodes can be chosen such that the coils are more decorrelated than their native state. However, in the 3D case, we consider $29400$ in-plane locations while still being able to select only $K$ linear phase encodes. Given that each in plane location has a varying coil profile, the 1D and 3D recovery problems while similar in principle, are drastically different in complexity and practice. In short, the ability of API to recover the underlying signal with greater fidelity than MB in the 3D case, is a testament to the robustness of the methodology.

### 10.1 Source of Improvements

The improvement in reconstruction is afforded by the phase encodes used in API which provide an avenue for decorrelating the underlying coil profiles. Mathematically, this is best explained by the spectral profiles of the encoding operators as seen in Fig. 9.3 and 9.8. For $L_2$ regularized recovery, $\lambda$ controls the tradeoff between data fidelity and the impact of noise. The approximation error of the $L_2$ regularized recovery process (relative to the un-regularlized system) can be written as

$$\sum_{r=1}^{R} \frac{\lambda^2}{\left(\sigma_r^2 + \lambda\right)^2} |\langle x_0, v_r \rangle|^2$$

where the encoding operator has $R$ singular values $\sigma_r$ with right singular vectors $v_r$ and ground truth signal $x_0$. For a fixed signal to noise ratio / fixed $\lambda$ is it trivial to observe that a larger $\sigma_r$ results in lower approximation error. This can also be examined from the perspective of dampening. $\lambda$ can also be interpretted as the scalar value that controls the effective recovery rank of the encoding operator. The larger $\sigma$ is, the larger $\lambda$ needs to be to reduce the effective recovery rank of the system. In both Fig. 9.3 and Fig. 9.8, we see that API has a better spectral profile relative to MB. It is this spectral profile that undergirds the

robust recovery seen in both the 1D (Fig. 9.2) and 3D case (Fig. 9.7). It must be noted that examining the spectral spread of the measurement operator is the best predictor of recovery accuracy relative to assumption based metrics that have been previously published such as the L-factor [125] and G-factor [126]. The L-factor methodology was designed for EPI based sequences and is computed by assuming a sinusoidal time series (i.e. computed using a single sinusoid of known frequency). Furthermore, the methodology relies on setting a user defined masking threshold which can result in drastically different L-factors for the same data set. The G-factor metric on the other hand is designed for in-plane acceleration techniques and does not generalize to through-plane acceleration. Furthermore, the computation of g-factor maps are not analytic for a given measurement system but are instead Monte Carlo based [126]. The spectral distribution of the measurement operator on the other hand can be trivially used to examine signal recovery in the noisy and noiseless case.

### 10.2 Flexibility in API Design

API also affords the flexibility of expanding windows and incorporating overlap which MB is not designed to do. In Fig. 9.2, the API windows were twice as large as their MB counterparts and thus had $50\%$ overlap between successive excitations. However, larger windows with overlap are not critical to the success of the API methology. For the proof of concept 3D recovery shown in Fig.9.7 API windows were kept only as large as their MB counterparts and had no overlap. Larger windows intrinsically result in larger SNRs given the greater volume of excitation (see section below). Thus, the principle of using larger windows with overlap might prove to quite useful in practice.

In addition to window flexibility, API invokes an excitation model that is true to the underlying physics. Given the slice separable reconstruction afforded by multiband methods implemented on clinical and research scanners, it is clear that MB does not account for inter-slice excitation leakage [120]. In all the results and simulations presented in this work, multiband was given an accurate forward model to prevent model inaccuracies from

obscuring the improvement seen using the API methodology. In practice, MB will perform poorer than has been shown here given its intrinsic modeling inaccuracies.

API also offers flexibility in the choice of phase encodes. Given the methodology utilized to pick phase encodes (see methods section), it is clear that there is not a single set of perfect phase encodes. The encodes can be chosen flexibly from a set of low frequency values such that the underlying spectral profile is "well" behaved. In practice, this sort of flexibility is desired given the mismatch that invariably occurs between theory and hardware implementation.

### 10.3 Signal to Noise Ratio

Examining SNR from a theoretical perspective provides intruiging insights. Unlike SENSE / GRAPPA, simultaneous multi slice imaging does not suffer from the $\sqrt{R}$ decrease in SNR [117]. Acceleration along the slice dimension is not diminished by the well known geometry factor $g$ factor [127, 126, 117]. API unlike MB, with its repeat factor (albeit with different encodes), can be thought of as having multiple averages (or more phase encodes in a traditional sense). Thus the SNR factor will increase by $\sqrt{N_{avg}} = \sqrt{R_p}$ where $R_p$ is the repeat factor that was defined earlier. Furthermore, if thicker slices are utilized, the SNR will increase proportionally to the thickness of the slice.

In this work, we gave multiband the benefit of a least squares regularized recovery to disambiguate methodological versus optimization improvements. In the literature, mutliband does not utilize tikhonov regularization [114, 113, 115, 118]. As such, in practice MB will perform significantly worse than what has been presented in our work.

### 10.4 Implementation Nuances and Generalizability

A common concern that arises when dealing with multi-slice excitation is that of SAR (Specific Absorption Rate). As the number of slices increases, the radio frequency energy deposited into a subject exceeds safety limits. If SAR limits are not reached, the radio fre-

quency amplifiers used on some MR scanners might not be able to successfully output the required waveform when multiple slices are being simultaneously excited. The same radio frequency hardware amplification challenges are seen at high field strength (7 T scanners). Since API requires multislice excitation that is a factor of atleast 2 or higher than multiband, radio frequency power amplification challenges must be addressed. In [128], the authors describe a methodology which allows for simultaneous multislice excitation while controlling overall RF power deposition (PINS : power independent number of slices). PINS operates by modulating apodized sinc functions with a dirac comb. In practice, this is done by utilizing a train of triangular slice gradient blips during the application of the RF pulse [128]. In principle, there is nothing in the API methodology which cannot be combined with PINS for practical reduction in RF power deposition. Alternatively, well known existing methods such as VERSE [129] (which can reduce power deposition by a factor of 4) can also be combined with API.

API can be viewed through several lenses. API can be interpreted as a methodology for decorrelating what are otherwise static coil profiles. In that regard, API transforms a static measurement operator into a dynamic one in which the user has some control over the coil profiles. API can alternatively be viewed as the deconvolution of windowed incomplete Fourier measurements(where the windows are applied in the spatial domain). In an equally valid point of view, API can be seen as the multi-coil and reconstruction generalization of the pseudo fourier methdology presented in [119].

API can also be thought of as a sister methodology to both blipped CAIPI [117] and CAIPIRINHA [116] (which in turn was the multi-coil implimentation of [130]). In API, the focus is on the through plane dimension instead of the in-plane dimension. Each of the phase encodes used in API along the slice direction exploits different regions of the coil sensitivity along the slice dimension (instead of the in-plane dimension in blipped CAIPI [117]/ CAIPIRINHA [116]).

On a larger scale, API can be viewed as generalized MR imaging. API's reconstruction

framework (Eq. 8.2) is one that encompasses 1D to 3D imaging and everything in between. Even multiband imaging can be seen through the lens of API recovery. If we set $\omega_k = 0$ and $R_p = 1$ in API's formulation, the resulting method would be multiband imaging. Atypical acquisition schemes that utilize slice overlap, 2D-3D hybrid imaging, partial phase encoding, varied coil geometries and sophisticated bases can all be captured under the generalized reconstruction framework presented in this work.

# CHAPTER 11
# SUMMARY AND FUTURE DIRECTIONS

In this work, we have been able to demonstrate that API is able to robustly recover the underlying signal ($10 - 40\%$ reduction in recovery error) relative to MB imaging. For a fixed recovery error, API is able to function at $> 10$dB lower SNR than MB. Unlike MB, API is not restricted to a rectangular non overlapping excitation profile and can therefore offer significantly greater flexbility in signal acquisition and reconstruction. The recovery framework we develop is generalizable to all forms of magnetic resonance imaging that lies on the 1D to 3D continuum.

While our work demonstrates the viability of the API methodology, there remain a host of new avenues for exploration. With explicit control over the phase encoding, API provides an ideal framework for augmentation with compressed sensing (CS). The phase encodes can be randomized to ensure that the sensing matrix meets the theoretical constraints necessary for signal recovery. In the same vein, constrained randomization of excitation windows (within hardware limits), might provide for a truly exciting, albeit challenging, new research direction. In our work, we assumed that we had access to the underlying coil profiles (either through the utilization of a pre-scan or otherwise). In practice, these coil profiles may not be known apriori. In those instances, the compressed sensing API approach can be modified to examine the blind deconvolution case. An example of this might be the $+/-1$ encoding examined in recent CS literature. To achieve such encoding in MR, a non selective RF pulse signal could be subtracted from the signal obtained from a multislice RF pulse to provide residual bands that follow the $+/-1$ encoding.

In our work, we noticed that in the 1D case, doubling window size and subsequently increasing overlap was beneficial to signal recovery. This however did not hold true in the 3D case. This is possibly due to the fact that in the 3D case, increasing the size of

each window while allowing for significant overlaps between excitations requires a larger budget of phase encodes to decorrelate each measurement. It is also our conjecture that these challenges observed with window size in the 3D case will prove less limiting in the non linear (CS) recovery case. All of these warrant further theoretical development and empirical testing.

A slightly more nuanced and challenging arena for further work will be in the realm of non linear phase encoding. The utilization of non linear phase encodes provide an entire new realm of possibility. The parameter space changes from the choice of $K$ encodes to selecting the $K$ set of polynomial order / coefficients. Thus the parameter space increases almost exponentially while providing a plethora of avenues to decorrelate the underlying coils. The only challenge with this type of implementation is that fact that non linear phase encodes require custom built hardware gradients and can only be implemented in a handful of locations internationally.

API focuses on through plane acceleration and as such can be augmented with well established in-plane acceleration techniques such as GRAPPA [96], SENSE [112], SMASH [97] for even higher accelerated imaging. In many ways, API forms the foundation of a new imaging approach for robust accelerated imaging.

# Appendices

# APPENDIX A

# RETROSPECTIVE RECONSTRUCTION: IAN

## A.1 Curvelet Frames, Non Medical Images and Norm Dependence

While the focus thus far has been on medical images, IAN can be used to work on a much more general class of signals and frames. None of the architecture / framework developed for IAN is exclusive to medical imaging / the frames used earlier (complex dual tree / double density dual tree wavelet). To demonstrate this, we present a super-resolution result obtained on a non medical image (Lena) using a curvelet frame [63] in Fig. A.1. For the result shown in Fig. A.1, the high resolution image was low pass filtered (anti aliasing filter) and downsampled by a factor of 4 to obtain the low resolution image. IAN recovers the underlying signal with the greatest fidelity. The recovery accuracy differential between IAN and SARA was substantial ( $4$ dB PSNR). A cursory examination of the images themselves demonstrate IAN recovers high frequency regions with greater accuracy relative to SARA (see hat fringe line in image). Even if the high frequency regions were not examined in close detail, the visual difference between the reconstruction afforded by IAN vs SARA is stark.

In our work, we have not explicitly discussed the choice of the optimal $p$. In our numerical experiments, the approach that was taken was to $p$ (typically $0.5$) while searching over the $\lambda$ parameter space. Given the single dimension of parameter search, the computational load was light. However, in reality, optimizing over both parameters $p$ and $\lambda$ will likely recover the underlying signals with higher fidelity. As a demonstration of this, we plot the recovery accuracy across iterations for different $p$ values while $\lambda$ is kept constant (Fig. A.2). It is interesting to note that despite the differences afforded by the choice of $p$, all choices of $p$ in this example outperform the recovery afforded by SARA ($32.6$ dB SNR).


Figure A.1: Single image super-resolution recovery for Lena. The observed signal was downsampled (by a factor of 4) and blurred version of the original high resolution signal (left). The recovery afforded by SARA, an analysis based reweighted $L_1$ solver, is shown in the middle column (PSNR : 30.03 dB). The recovery afforded by IAN is shown in the right column (PSNR : 34.41 dB). IAN is able to recover the high frequency regions of the image with higher fidelity relative to SARA (hat fringe line, eyes, hat striations). Even without examining these specific high frequency regions, it is trivial to see the increase in quality afforded by IAN

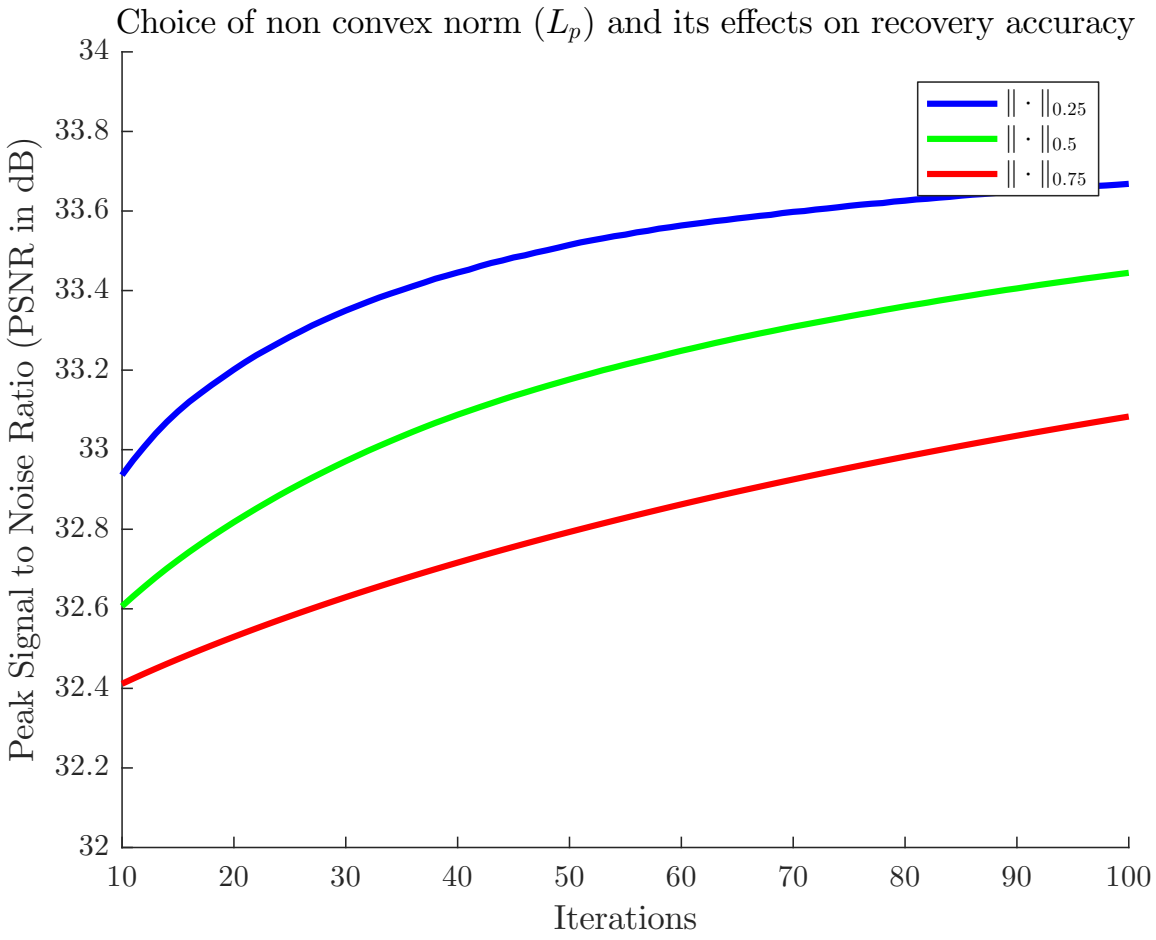


Figure A.2: Single image super-resolution recovery accuracy across iterations when $\lambda$ is fixed for different $L_p$ norms. For a fixed $\lambda$, the choice of norm can result in a reconstruction accuracy differential on the order of 1 dB PSNR.

## A.2 Total Variation Denoising

### A.2.1 Parallel Dykstra based IAN with TV

Earlier in this work, we presented a version of IAN which invoked a parallel dykstra framework for enforcement of the TV and $L_p$ proximal operators(Algorithm 5). While both algorithms (IAN with TV - Algorithm 4, IAN with TV - parallel dykstra - Algorithm 5) presented in the methods chapter work equally well for denoising, it was our experience that Algorithm 5 was computationally faster than algorithm 4 when access to a parallel computing was made available. All the denoising results presente thus far in this work has utilized the architecture specified in Algorithm 4. In Fig. A.3 we demonstrate the viability of Algorithm 5 to denoise the underlying signal with high fidelity. The MR knee image denoised in Fig. A.3 is an example of ground truth denoising where the true signal is unknown. Thus to quantify recovery accuracy we utilize the IQM metric [77]. Besides validating the utility of the parallel dykstra algorithm, Fig. A.3 demonstrates IAN's ability to denoise complicated ground truth images whose noise profile is spatially varying.

### A.2.2 Regularization

For the algorithms presented in this paper, it is necessary to tune the regularization parameters $\lambda_1$ for the $L_p$ norm and $\lambda_2$ for the TV norm. This is usually performed by invoking a grid search of the parameter space. As demonstrated in the discussion section, the parameter choice is fairly robust within an order of a magnitude of the best parameter set. This is demonstrated in the TV case in Fig. A.4

## A.3 Representative Algorithm Parameters

Below we provide the parameters necessary to replicate some of IAN's recovery results shown in this dissertation.


Figure A.3: Ground truth denoising of an MRI knee acquisition. The ground truth image is shown on the left. The image denoised using BM3D is shown in the middle column (IQM : 0.437). The image denoised using IAN with TV (IQM : 0.449) is shown on the right column. Visually, the difference between the denoising schemes can be seen by examining the bone (both above and below) the knee. In both areas, IAN renders a more uniform signal while keeping the relevant high frequency content intact. The algorithmic framework used here is the parallel dykstra approach (Algorithm 5).

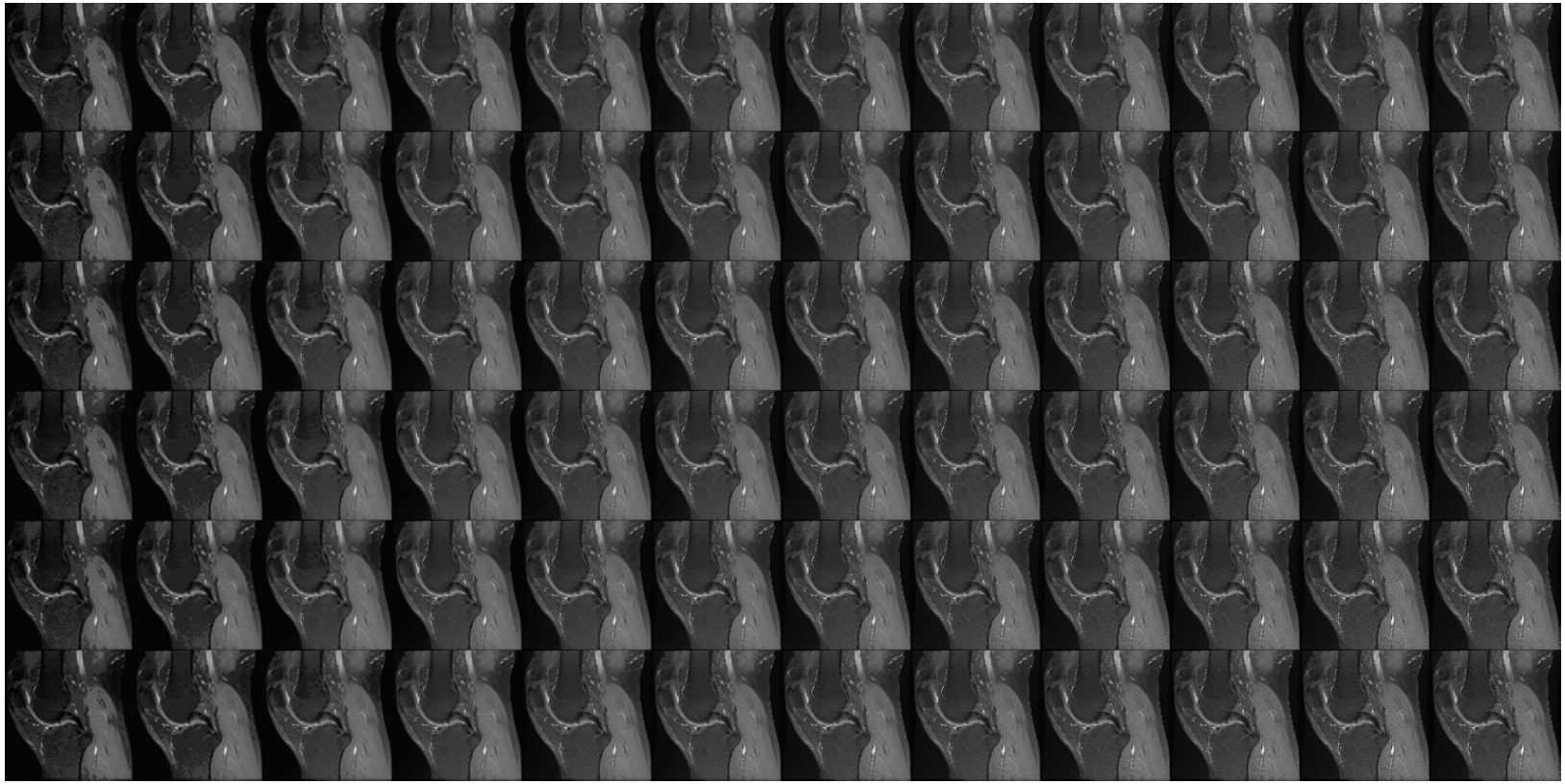


Figure A.4: This recovery montage depicts the denoising results obtained for different combination of parameter pairs. The $L_p$ norm regularization decreases from top to bottom while the TV norm regularizer decreases from left to right. The $L_p$ norm regularizer range from $1$ to $10^{-5}$ while the TV norm regularizers range from $10^{-1}$ to $10^{-4}$. Visually, there are combinations of parameter pairs for which the recovery is indistinguishable.

| MRI Super-Resolution (Fig. 4.1) | |
|---|---|
| **Parameter** | **Value** |
| $p$ | $0.5$ |
| $tol$ | $10^{-8}$ |
| $k$ | $100$ |
| $m$ | $20$ |
| $tol_d$ | $10^{-4}$ |
| $t$ | $0.5$ |
| $c$ | $500$ |
| $tol_g$ | $10^{-6}$ |
| $\lambda$ | $6.57 \times 10^{-6}$ |
| Image Source | BRAINX [70] |
| $\boldsymbol{W}$ | 6 Daubechies Wavelets + 2 Biorthogonal Wavelets with Cycle Spinning |
| $x_0$ | Lanczos 3 Interpolation |

| Fluoroscopic Super-Resolution (Fig. 4.2) | |
|---|---|
| **Parameter** | **Value** |
| $p$ | $0.5$ |
| $tol$ | $10^{-8}$ |
| $k$ | $100$ |
| $m$ | $20$ |
| $tol_d$ | $10^{-4}$ |
| $t$ | $0.5$ |
| $c$ | $500$ |
| $tol_g$ | $10^{-6}$ |
| $\lambda$ | $6.57 \times 10^{-6}$ |
| Image Source | Siemens Proprietary AX Image |
| $\boldsymbol{W}$ | 6 Daubechies Wavelets + 2 Biorthogonal Wavelets with Cycle Spinning |
| $x_0$ | Lanczos 3 Interpolation |

| CT Cervical Tumor Undersampled Recovery (Fig. 4.5) | |
|---|---|
| **Parameter** | **Value** |
| $p$ | $0.5$ |
| $tol$ | $10^{-6}$ |
| $k$ | $50$ |
| $m$ | $10$ |
| $tol_d$ | $10^{-4}$ |
| $t$ | $2.2 \times 10^{-4}$ |
| $c$ | $20$ |
| $tol_g$ | $10^{-6}$ |
| $\lambda_1$ | $6.3 \times 10^{-3}$ |
| $\lambda_2$ | $10^{-6}$ |
| Image Source | COMMUNIX [70] |
| Views | 45 |
| $\boldsymbol{W}$ | Undecimated Dual Tree Complex Wavelets |
| $x_0$ | $\vec{0}$ |

| CT Renal Obstruction Undersampled Recovery (Fig. 4.5) | |
|---|---|
| **Parameter** | **Value** |
| $p$ | $0.5$ |
| $tol$ | $10^{-6}$ |
| $k$ | $50$ |
| $m$ | $10$ |
| $tol_d$ | $10^{-4}$ |
| $t$ | $2.2 \times 10^{-4}$ |
| $c$ | $20$ |
| $tol_g$ | $10^{-6}$ |
| $\lambda_1$ | $3.98 \times 10^{-2}$ |
| $\lambda_2$ | $10^{-5}$ |
| Image Source | CENOVIX [70] |
| Views | 45 |
| $\boldsymbol{W}$ | Undecimated Dual Tree Wavelets |
| $x_0$ | $\vec{0}$ |

| CT Atherosclerosis Undersampled Recovery (Fig. 4.5) | |
|---|---|
| **Parameter** | **Value** |
| $p$ | $0.5$ |
| $tol$ | $10^{-6}$ |
| $k$ | $50$ |
| $m$ | $10$ |
| $tol_d$ | $10^{-4}$ |
| $t$ | $2.2 \times 10^{-4}$ |
| $c$ | $20$ |
| $tol_g$ | $10^{-6}$ |
| $\lambda_1$ | $3.98 \times 10^{-2}$ |
| $\lambda_2$ | $10^{-5}$ |
| Image Source | KESKONRIX [70] |
| Views | 45 |
| $\boldsymbol{W}$ | Undecimated Dual Tree Wavelets |
| $x_0$ | $\vec{0}$ |

| Phantom Denoising (Fig. 4.6) | |
|---|---|
| **Parameter** | **Value** |
| $p$ | $0.5$ |
| $tol$ | $10^{-8}$ |
| $k$ | $50$ |
| $m$ | $10$ |
| $tol_d$ | $10^{-4}$ |
| $t$ | $1$ |
| $c$ | $1$ |
| $tol_g$ | $1$ |
| $\lambda_1$ | $3.16$ |
| $\lambda_2$ | $31.62$ |
| Image Source | Siemens Proprietary |
| $\boldsymbol{W}$ | Daubechies 1-8 with Cycle Spinning |
| $x_0$ | LP image |

# APPENDIX B

# PROSPECTIVE RECONSTRUCTION: API

## B.1 Complete 3D Reconstruction

In the results section, we presented the 3D reconstruction of 6 of 112 slices to demonstrate that API was able to recover the signal with greater fidelity relative to multiband. The errors provided for Fig. 9.7 was the global recovery error across all the slices. Here we present the entire 3D reconstruction set afforded by MB and API for a complete examination of the improvement that API provides over MB (R = 8). The errors provided in Fig. B.1 - B.19 are only for the slices shown. The SNR value provided is for the entire 3D stack of 112 and not just for the slices shown.

## B.2 Static phase within each window

In the API model, the phase varies linearly across the entire slice plane and thus even within each slice. However, if we were to assume that the phase did vary linearly across slices but was constant within each slice, the resulting model would utilize standard excitation windows but now with a fixed phase. This prevents the generation of windows which have sinusoidal variations. In one of our early 3D simulations, this form static phase within each slice was invoked as a result of a coding error. The result of this simulation is plotted in Fig. B.20. At an SNR of $35$dB and an acceleration factor of 8, API is able to recover the underlying signal with $50\%$ less recovery error relative to MB.

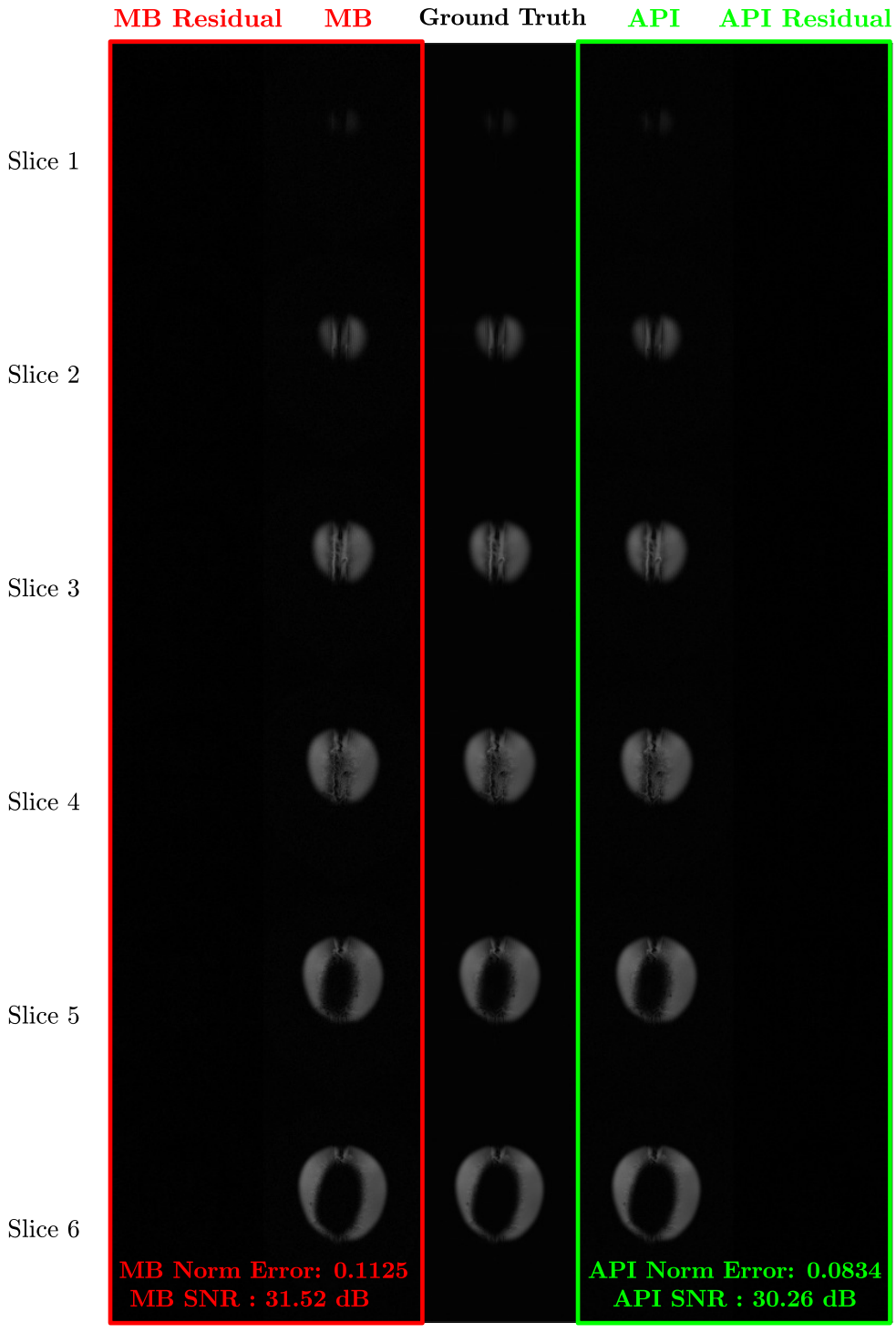


Figure B.1: 3D Recovery for Slices 1-6 when MB and API are used to recover the underlying signal for an acceleration factor of 8. The recovery afforded by each method is plotted along with the underlying ground truth and residuals. For these 6 slices, API reconstructs the underlying signal with approximately $35\%$ lower error $(0.0845)$ versus MB's $(0.1125)$.

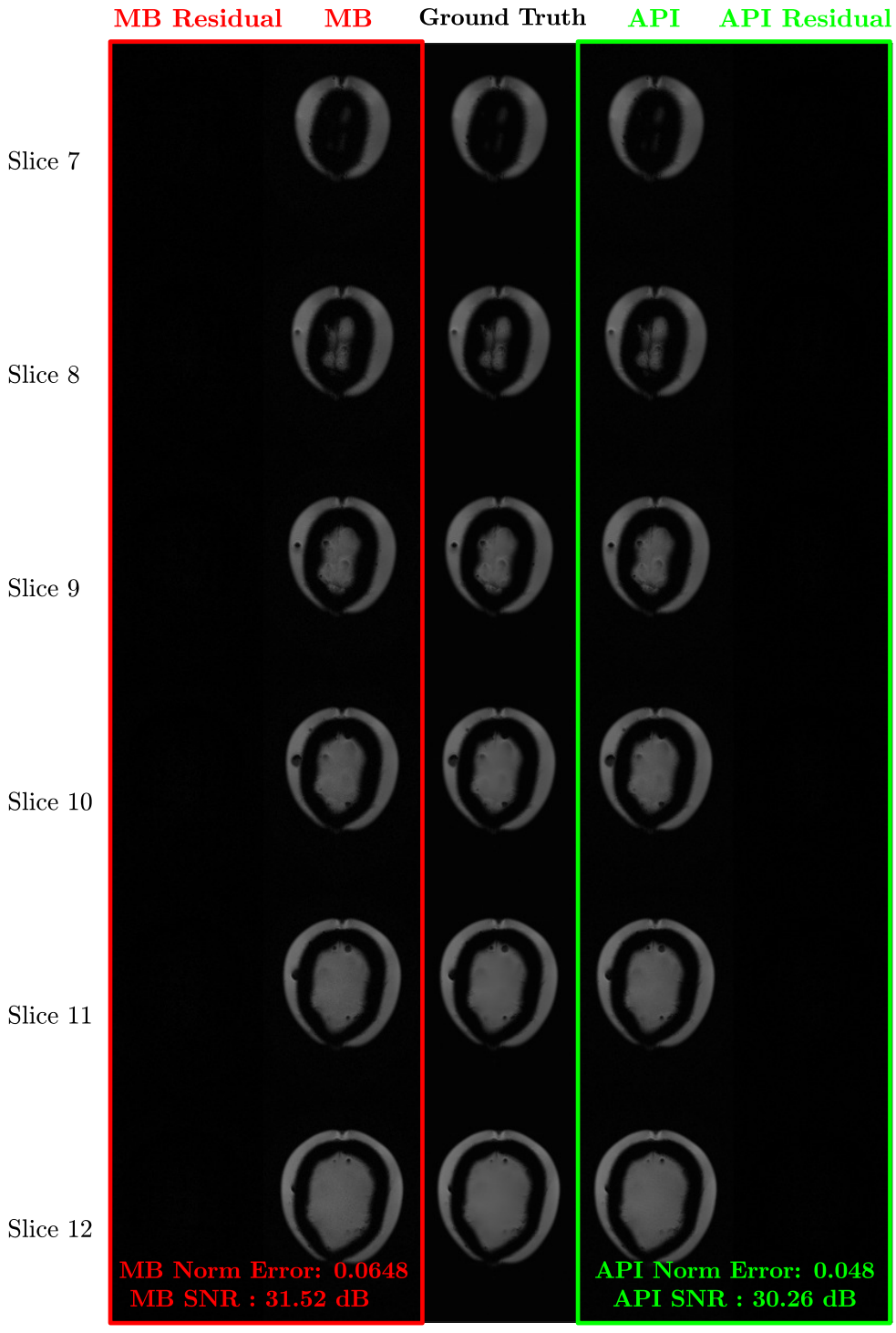


Figure B.2: 3D Recovery for Slices 7-12 when MB and API are used to recover the underlying signal for an acceleration factor of 8. The recovery afforded by each method is plotted along with the underlying ground truth and residuals. For these 6 slices, API reconstructs the underlying signal with approximately $35\%$ lower error $(0.0480)$ versus MB's $(0.0648)$.

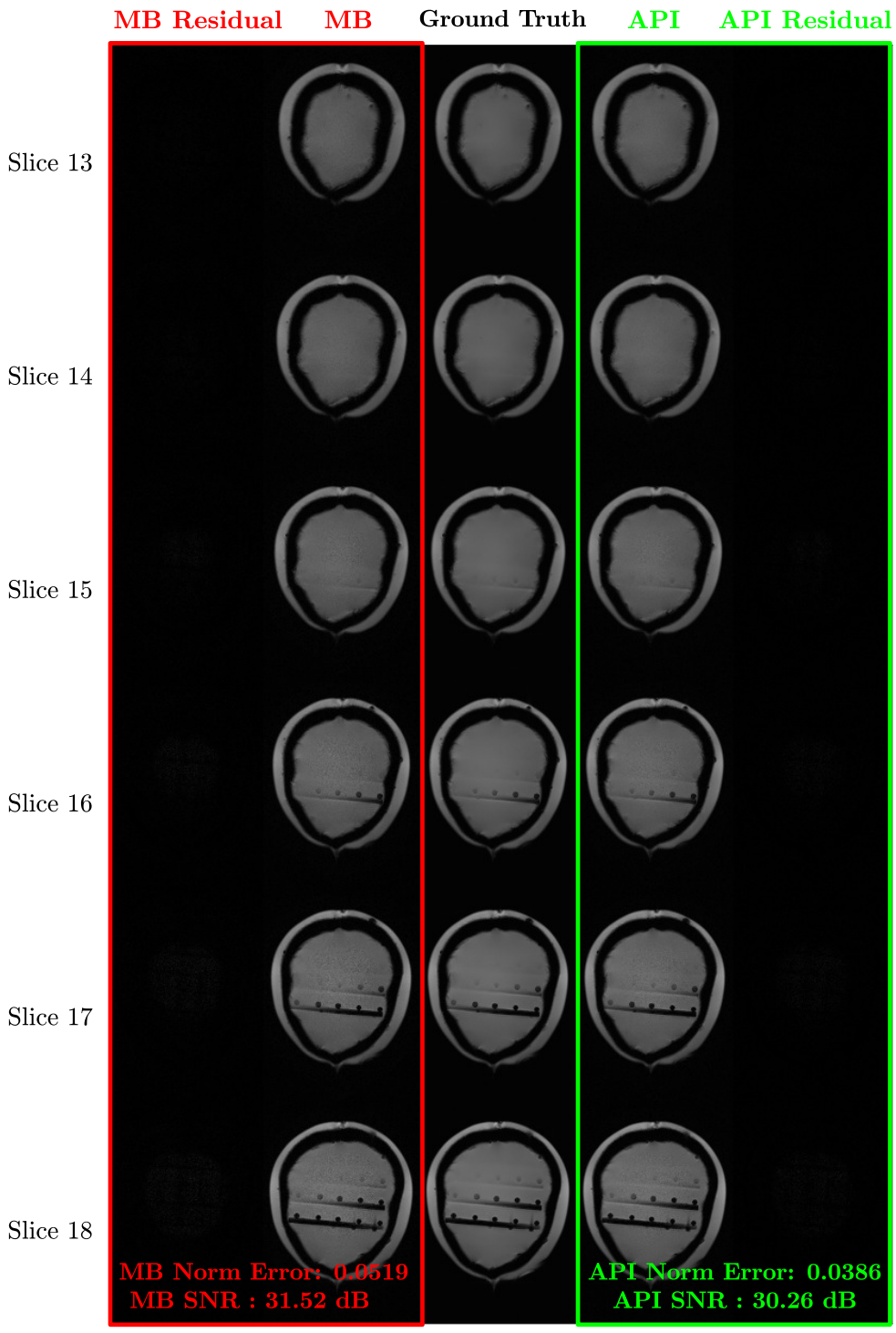


Figure B.3: 3D Recovery for Slices 13-18 when MB and API are used to recover the underlying signal for an acceleration factor of 8. The recovery afforded by each method is plotted along with the underlying ground truth and residuals. For these 6 slices, API reconstructs the underlying signal with approximately $34\%$ lower error $(0.0386)$ versus MB's $(0.0519)$.

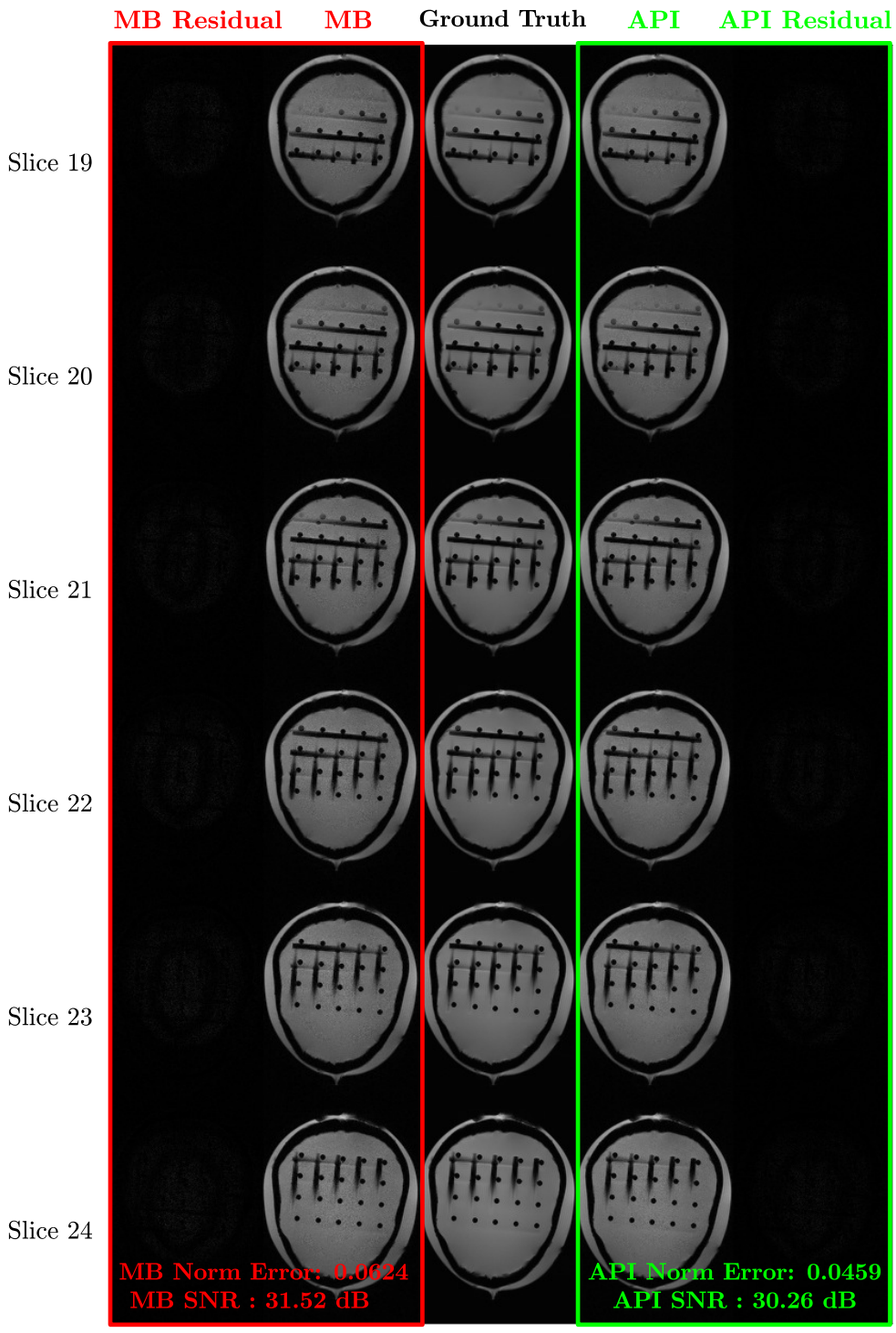


Figure B.4: 3D Recovery for Slices 19-24 when MB and API are used to recover the underlying signal for an acceleration factor of 8. The recovery afforded by each method is plotted along with the underlying ground truth and residuals. For these 6 slices, API reconstructs the underlying signal with approximately $36\%$ lower error $(0.0459)$ versus MB's $(0.0624)$.

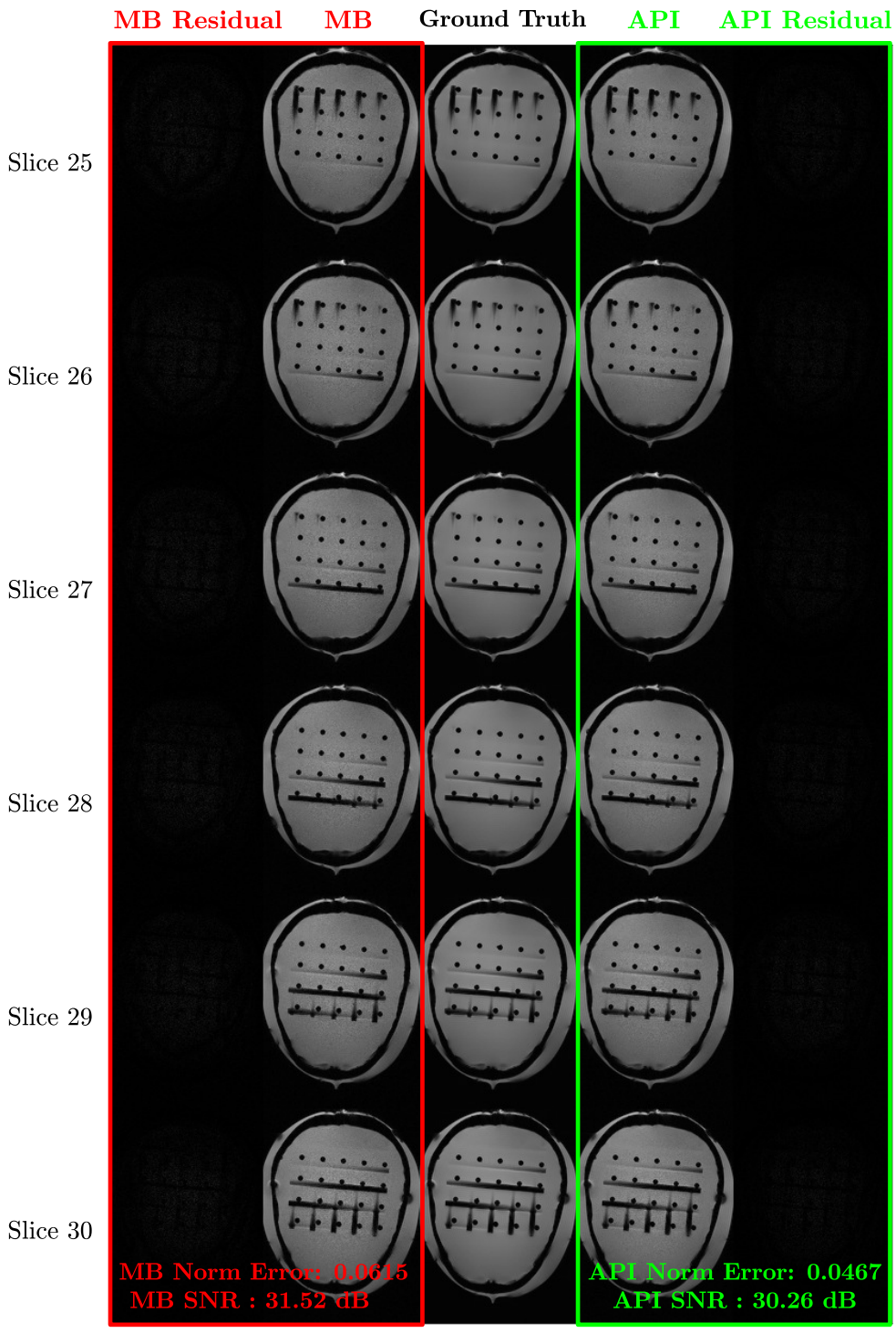


Figure B.5: 3D Recovery for Slices 25-30 when MB and API are used to recover the underlying signal for an acceleration factor of 8. The recovery afforded by each method is plotted along with the underlying ground truth and residuals. For these 6 slices, API reconstructs the underlying signal with approximately $32\%$ lower error $(0.0467)$ versus MB's $(0.0615)$.

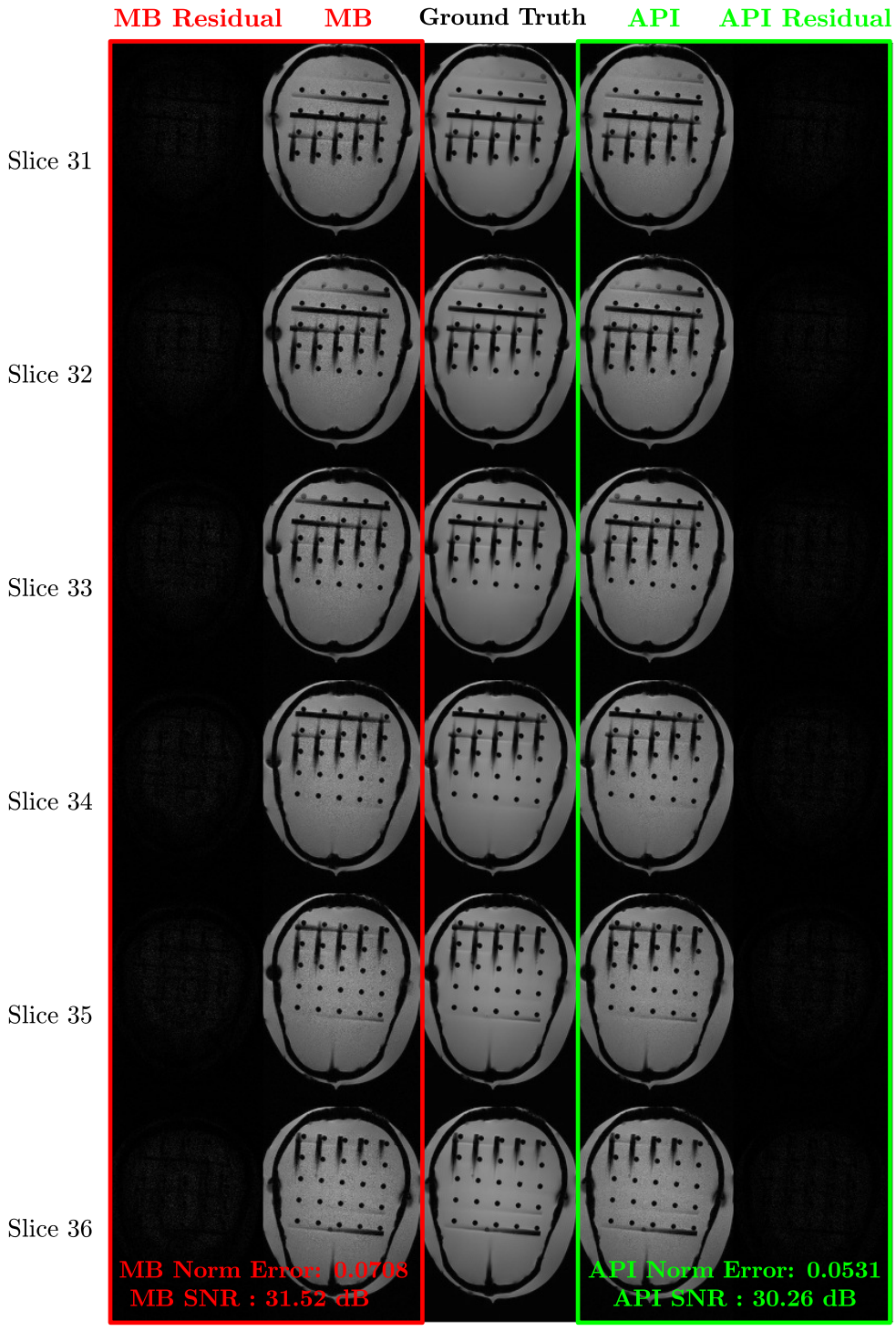


Figure B.6: 3D Recovery for Slices 31-36 when MB and API are used to recover the underlying signal for an acceleration factor of 8. The recovery afforded by each method is plotted along with the underlying ground truth and residuals. For these 6 slices, API reconstructs the underlying signal with approximately $33\%$ lower error $(0.0708)$ versus MB's $(0.0531)$.

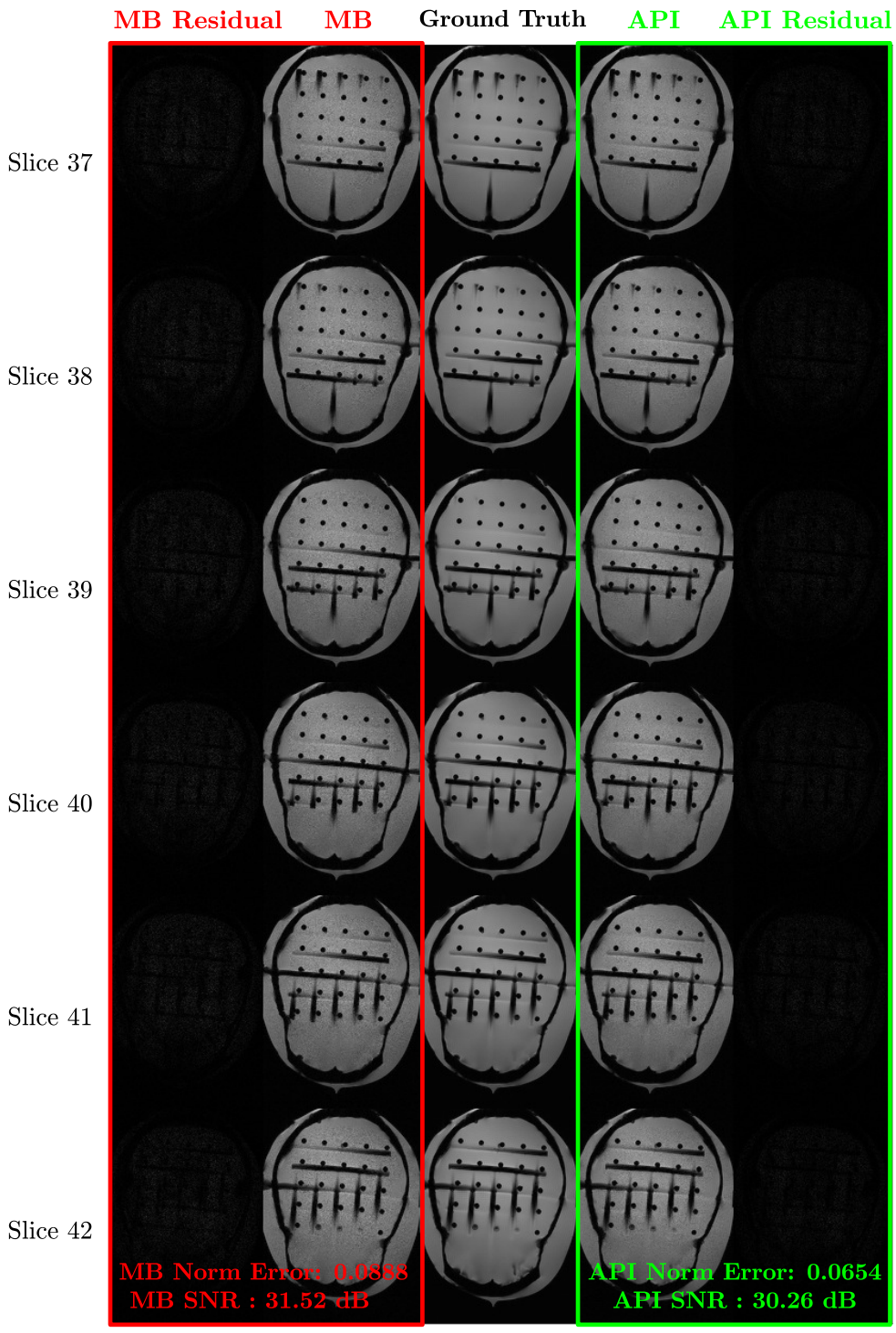


Figure B.7: 3D Recovery for Slices 37-42 when MB and API are used to recover the underlying signal for an acceleration factor of 8. The recovery afforded by each method is plotted along with the underlying ground truth and residuals. For these 6 slices, API reconstructs the underlying signal with approximately $36\%$ lower error $(0.0888)$ versus MB's $(0.0654)$.

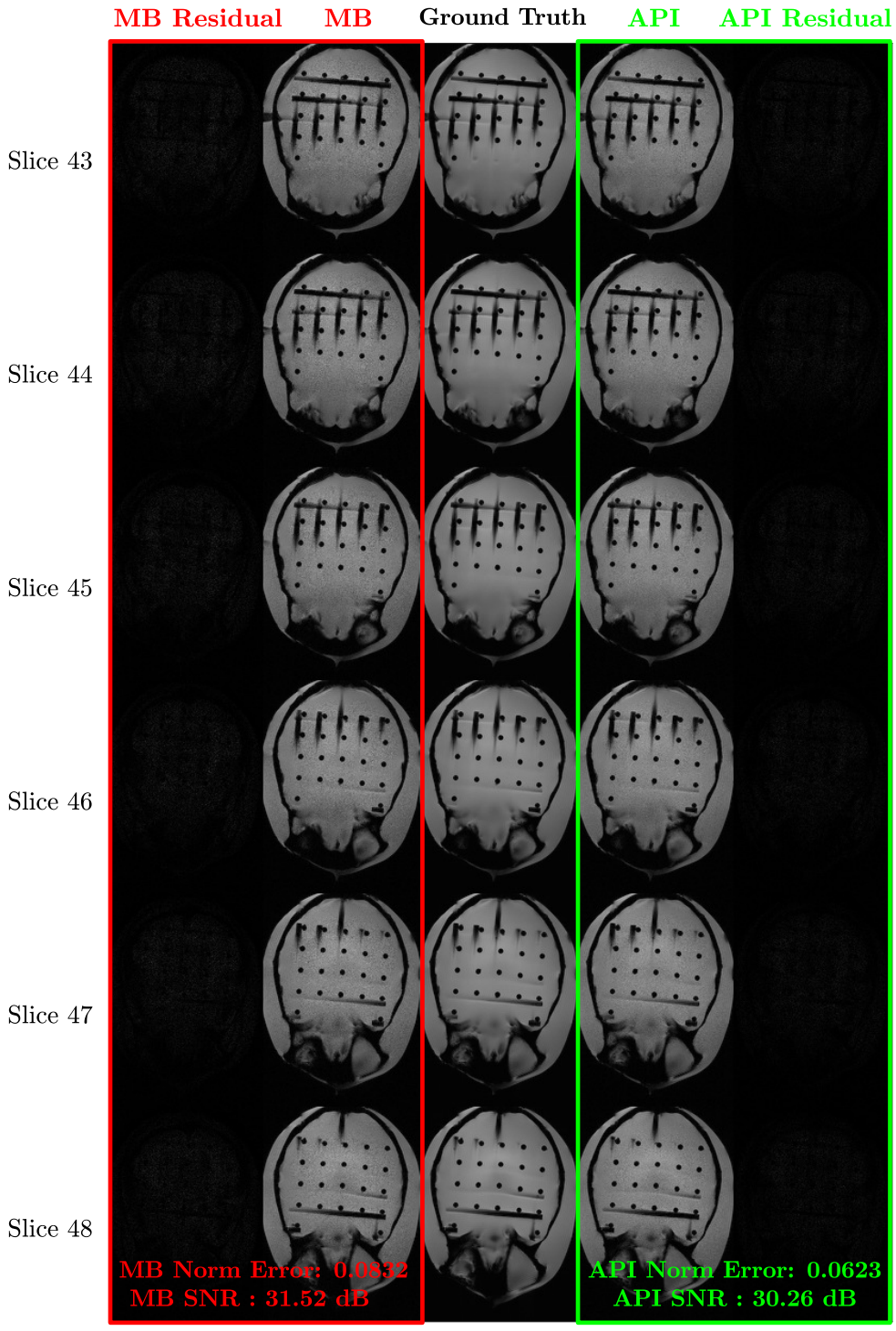


Figure B.8: 3D Recovery for Slices 43-48 when MB and API are used to recover the underlying signal for an acceleration factor of 8. The recovery afforded by each method is plotted along with the underlying ground truth and residuals. For these 6 slices, API reconstructs the underlying signal with approximately $34\%$ lower error $(0.0832)$ versus MB's $(0.0623)$.

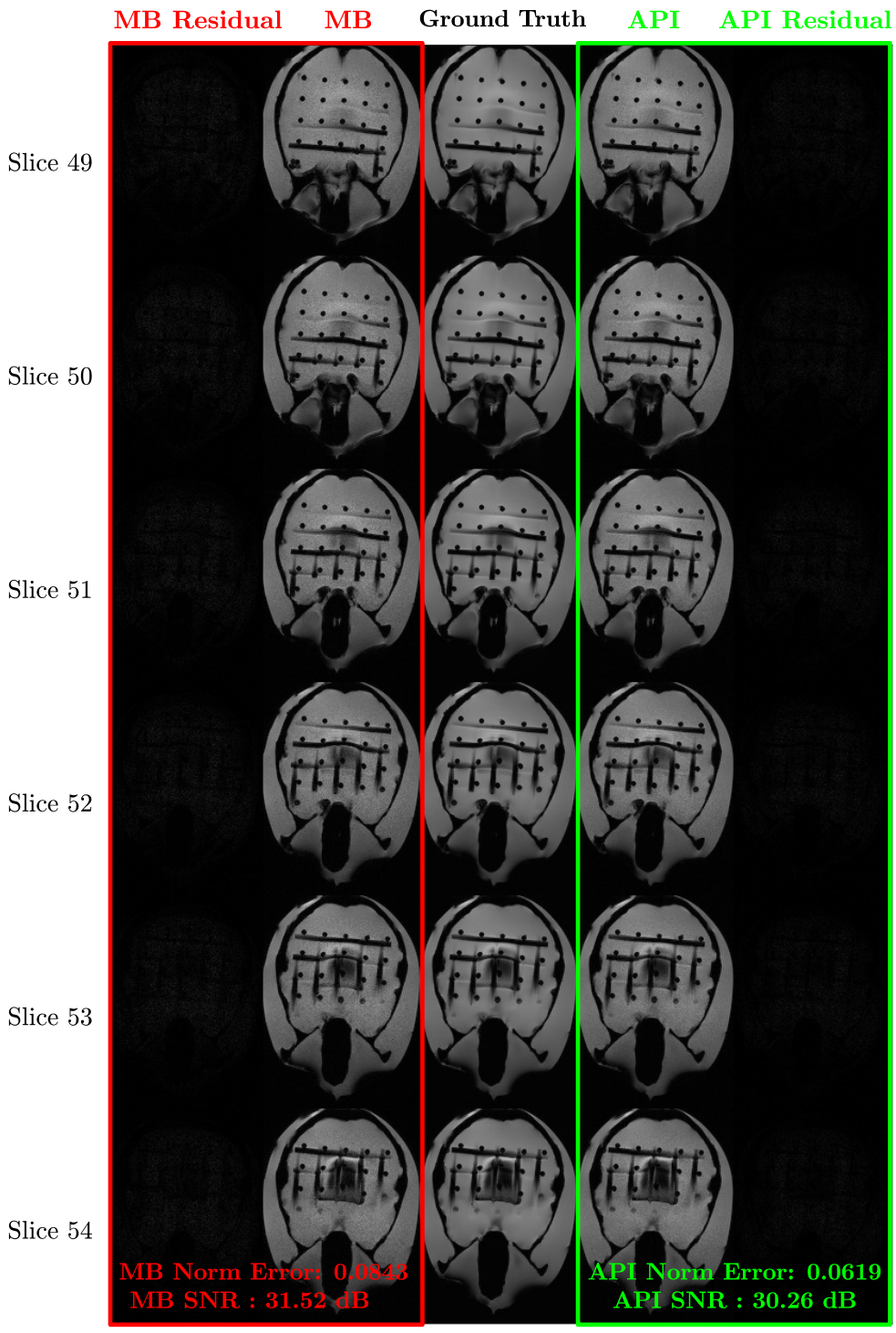


Figure B.9: 3D Recovery for Slices 49-54 when MB and API are used to recover the underlying signal for an acceleration factor of 8. The recovery afforded by each method is plotted along with the underlying ground truth and residuals. For these 6 slices, API reconstructs the underlying signal with approximately 32% lower error (0.0813) versus MB's (0.0619).

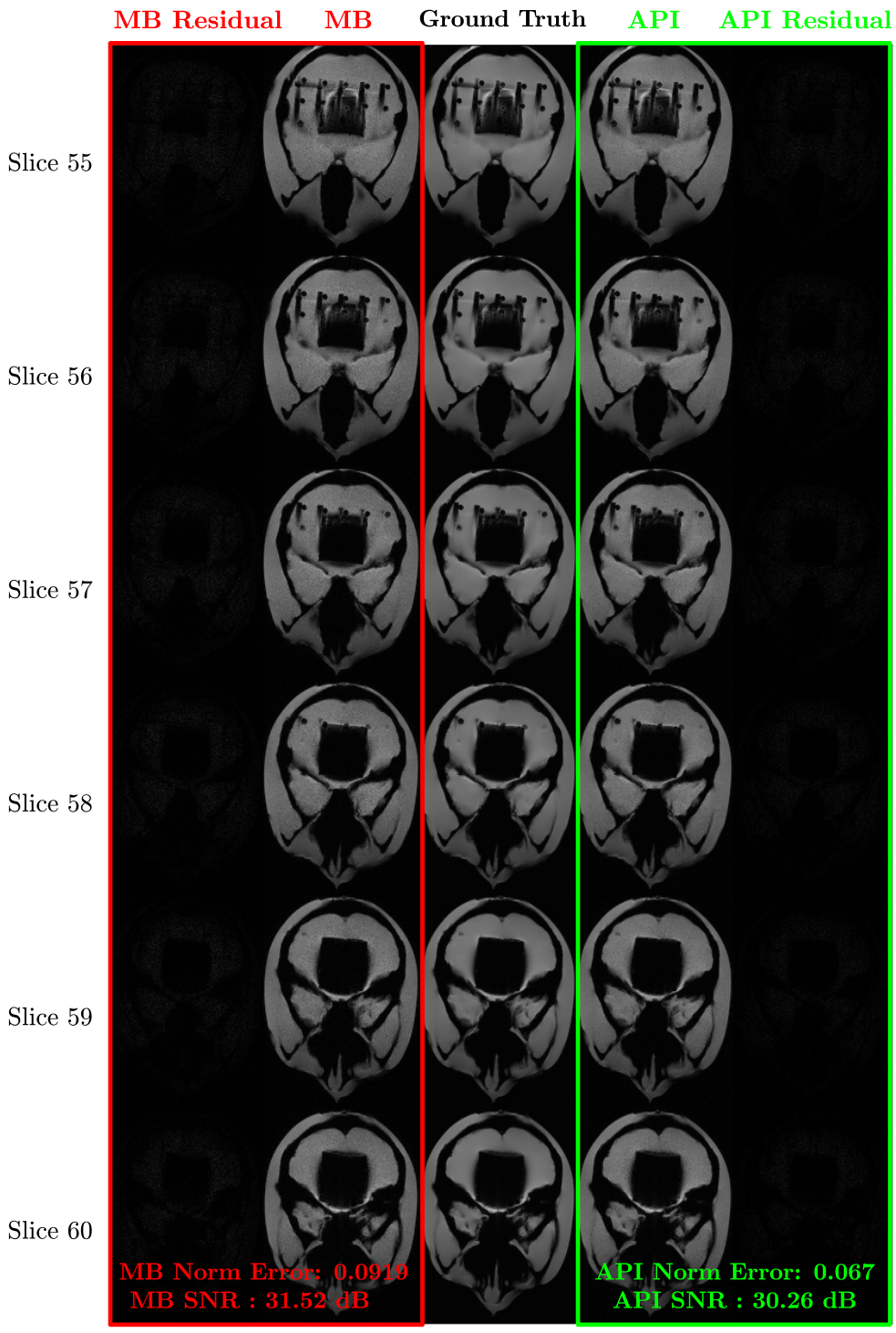


Figure B.10: 3D Recovery for Slices 55-60 when MB and API are used to recover the underlying signal for an acceleration factor of 8. The recovery afforded by each method is plotted along with the underlying ground truth and residuals. For these 6 slices, API reconstructs the underlying signal with approximately $37\%$ lower error $(0.0670)$ versus MB's $(0.0919)$.

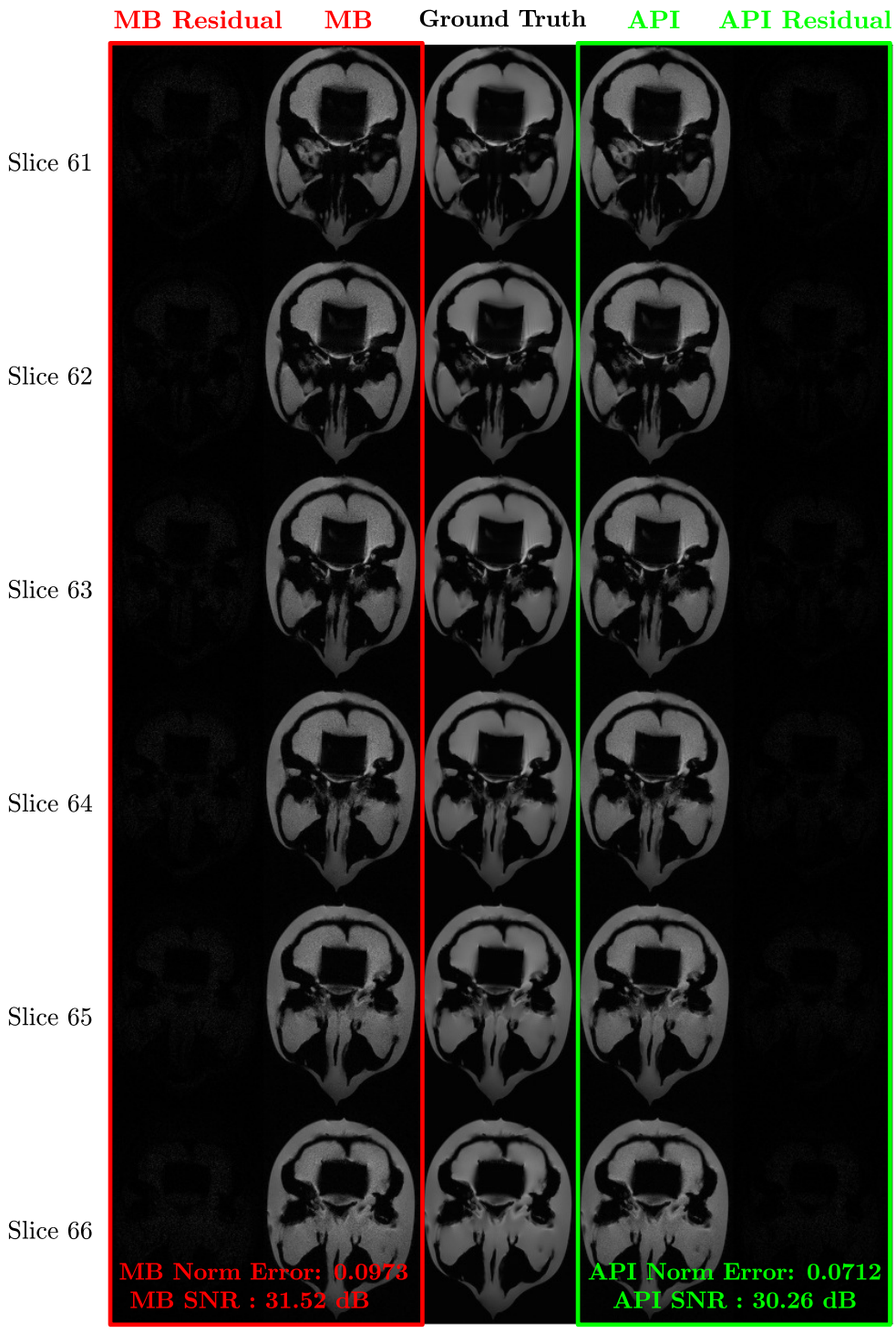


Figure B.11: 3D Recovery for Slices 61-66 when MB and API are used to recover the underlying signal for an acceleration factor of 8. The recovery afforded by each method is plotted along with the underlying ground truth and residuals. For these 6 slices, API reconstructs the underlying signal with approximately $37\%$ lower error $(0.0712)$ versus MB's $(0.0973)$.

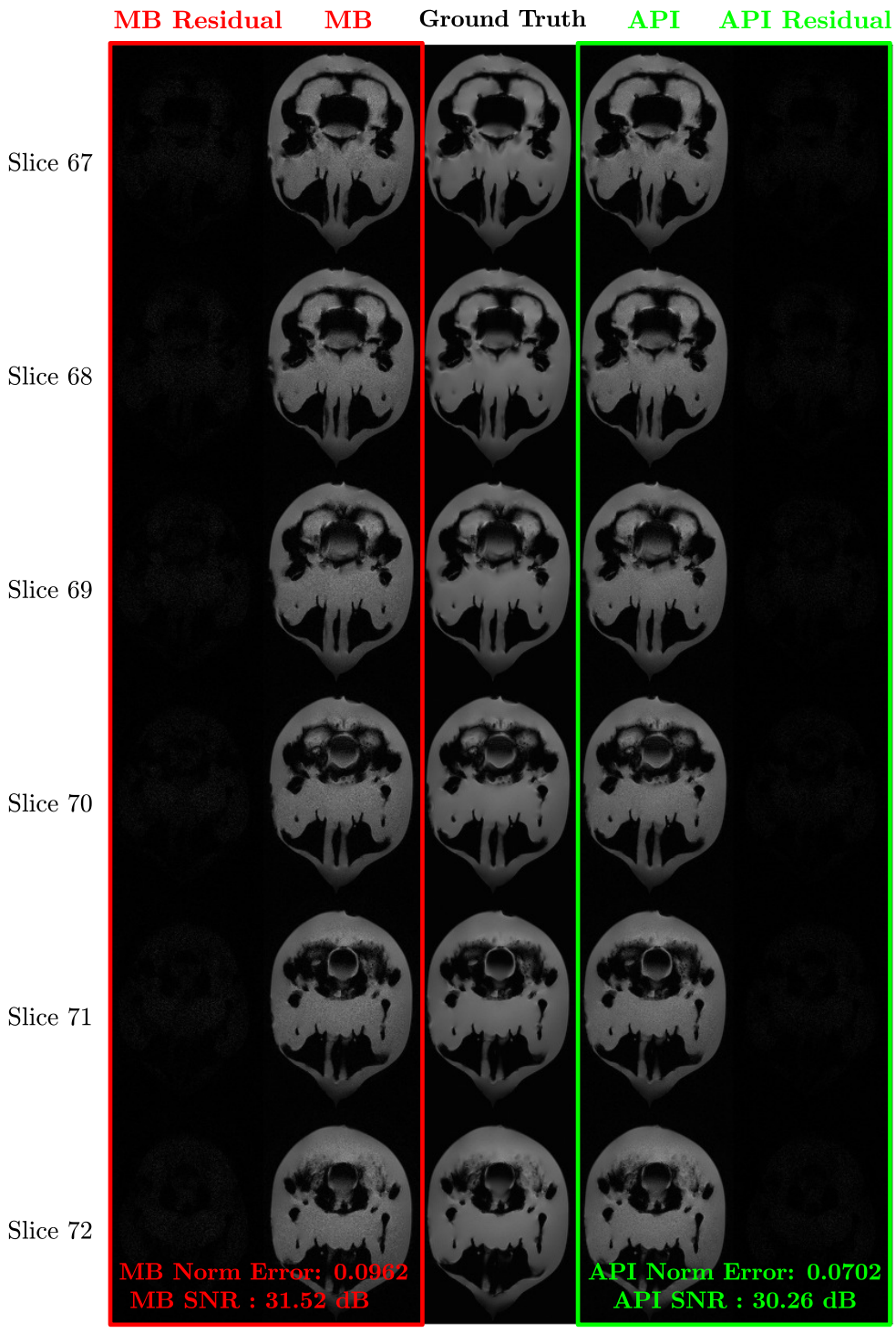


Figure B.12: 3D Recovery for Slices 67-72 when MB and API are used to recover the underlying signal for an acceleration factor of 8. The recovery afforded by each method is plotted along with the underlying ground truth and residuals. For these 6 slices, API reconstructs the underlying signal with approximately $37\%$ lower error $(0.0702)$ versus MB's $(0.0962)$.

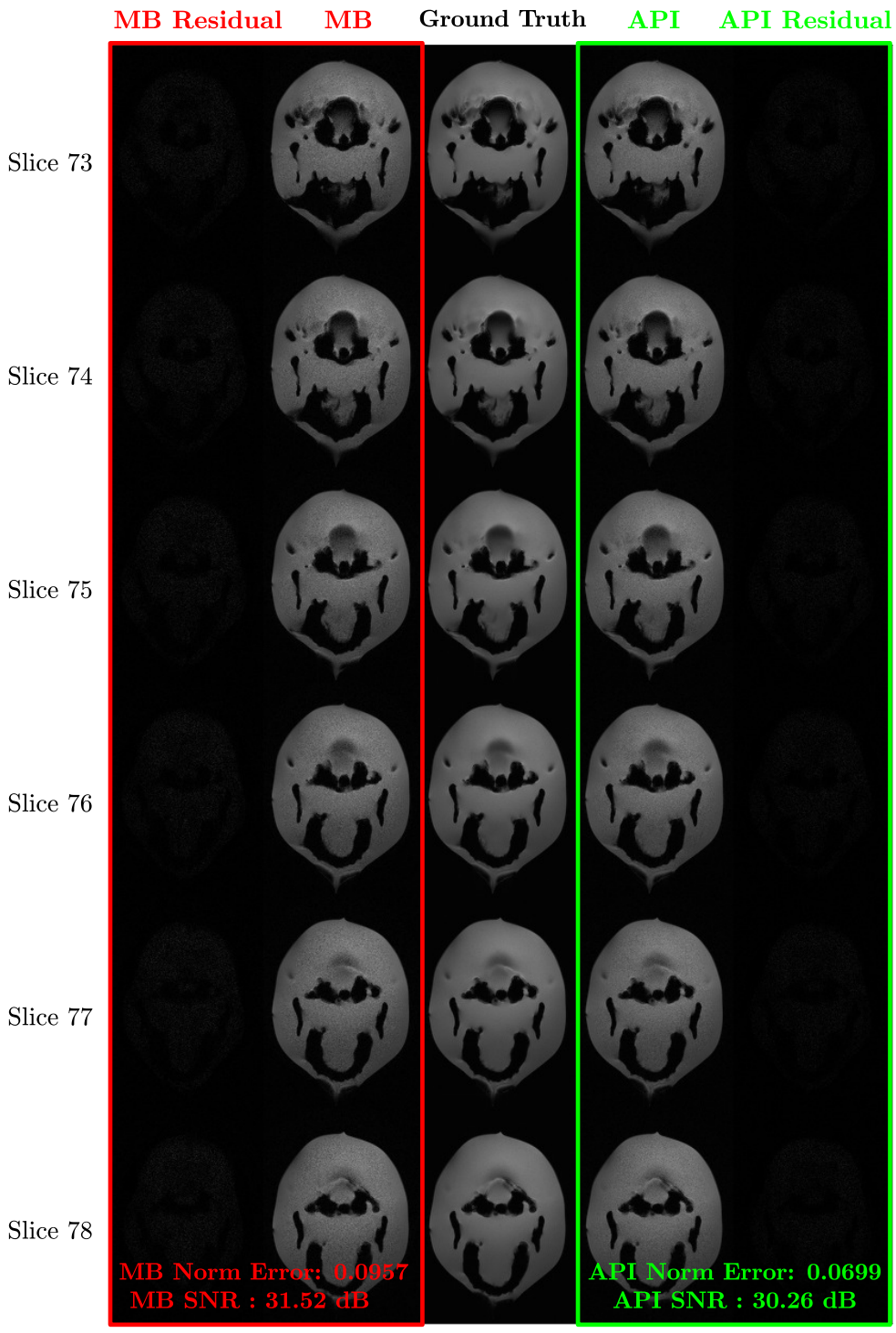


Figure B.13: 3D Recovery for Slices 73-78 when MB and API are used to recover the underlying signal for an acceleration factor of 8. The recovery afforded by each method is plotted along with the underlying ground truth and residuals. For these 6 slices, API reconstructs the underlying signal with approximately 37% lower error (0.0699) versus MB's (0.0957).

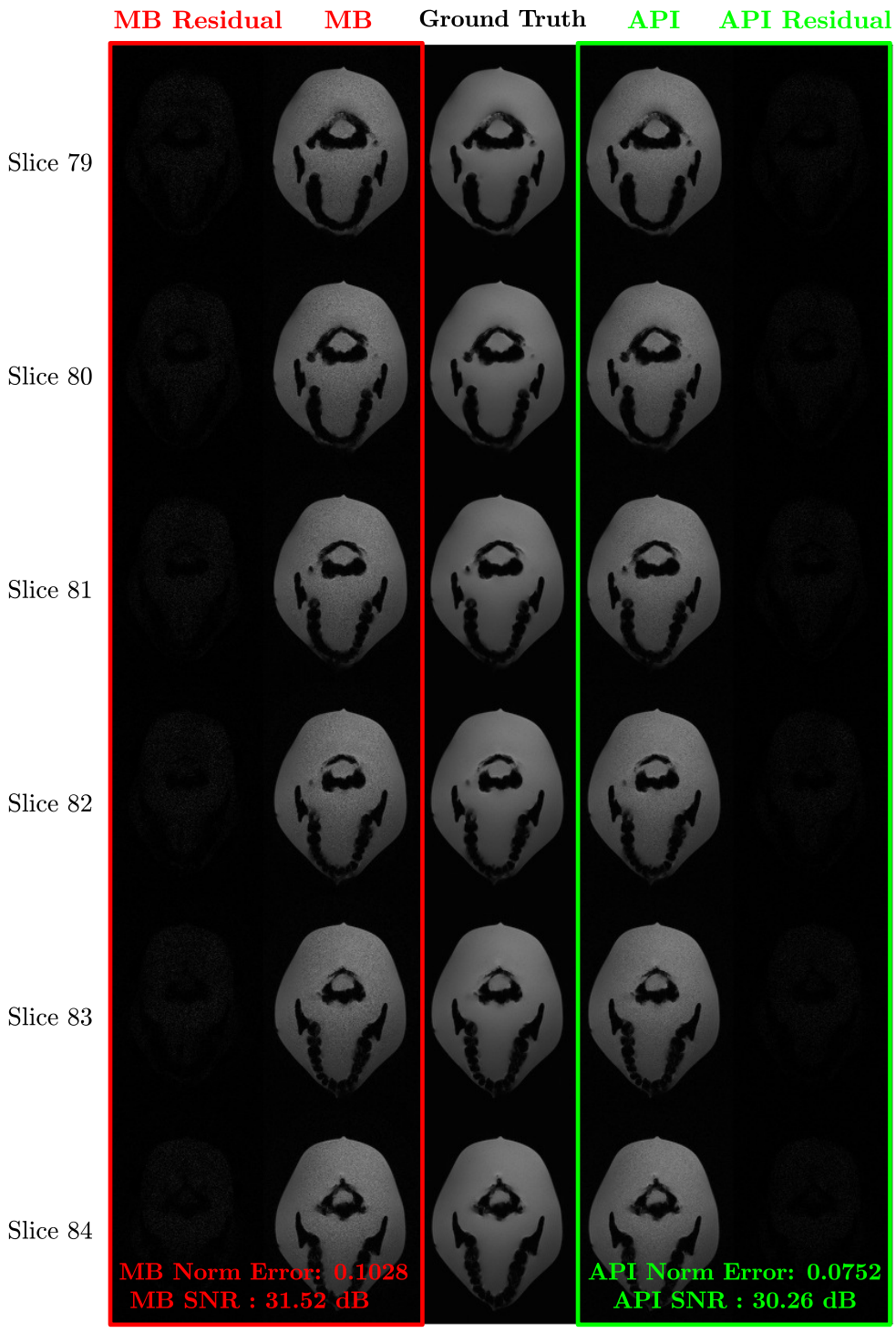


Figure B.14: 3D Recovery for Slices 79-84 when MB and API are used to recover the underlying signal for an acceleration factor of 8. The recovery afforded by each method is plotted along with the underlying ground truth and residuals. For these 6 slices, API reconstructs the underlying signal with approximately $37\%$ lower error $(0.0752)$ versus MB's $(0.1028)$.

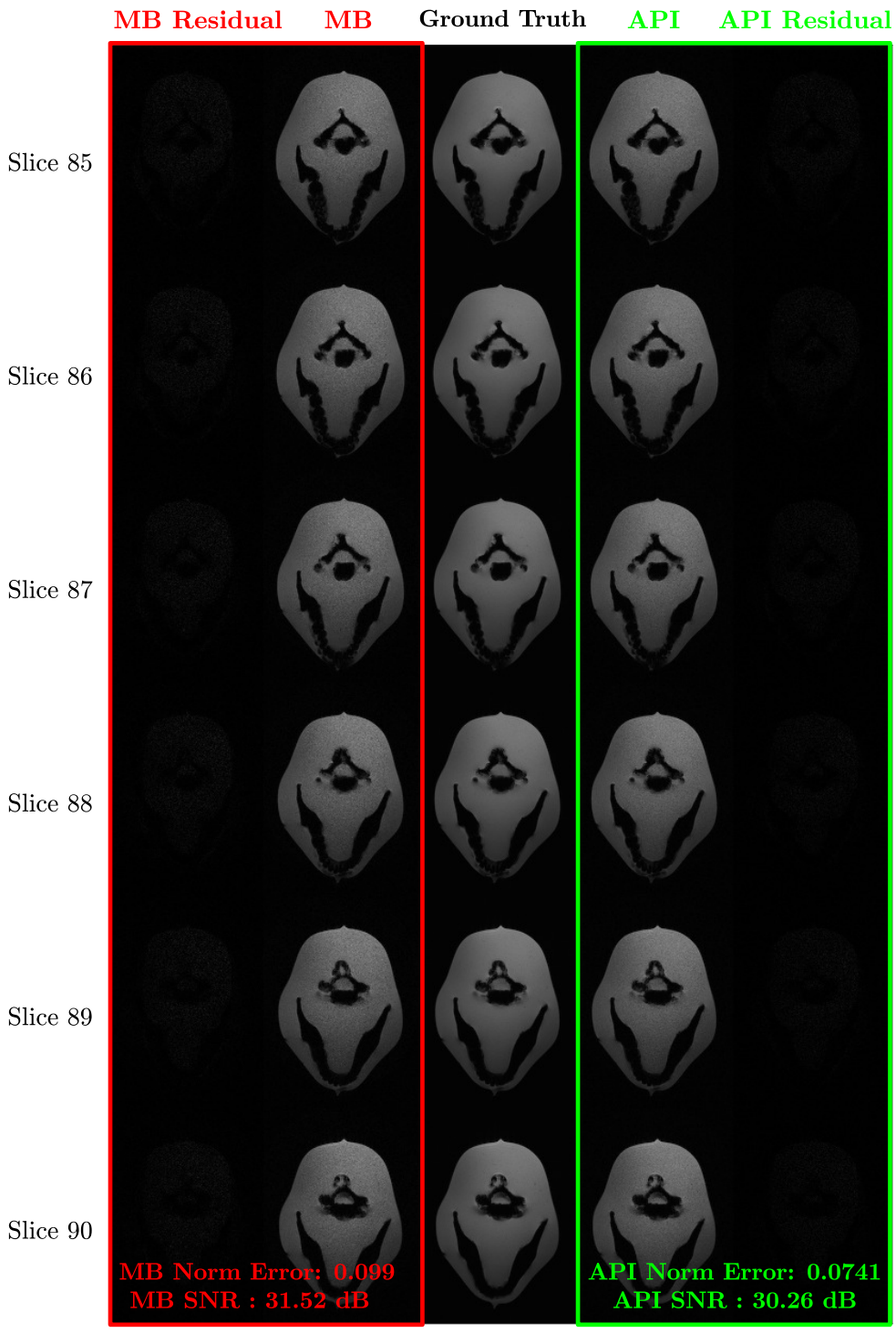


Figure B.15: 3D Recovery for Slices 85-90 when MB and API are used to recover the underlying signal for an acceleration factor of 8. The recovery afforded by each method is plotted along with the underlying ground truth and residuals. For these 6 slices, API reconstructs the underlying signal with approximately $34\%$ lower error $(0.0741)$ versus MB's $(0.099)$.

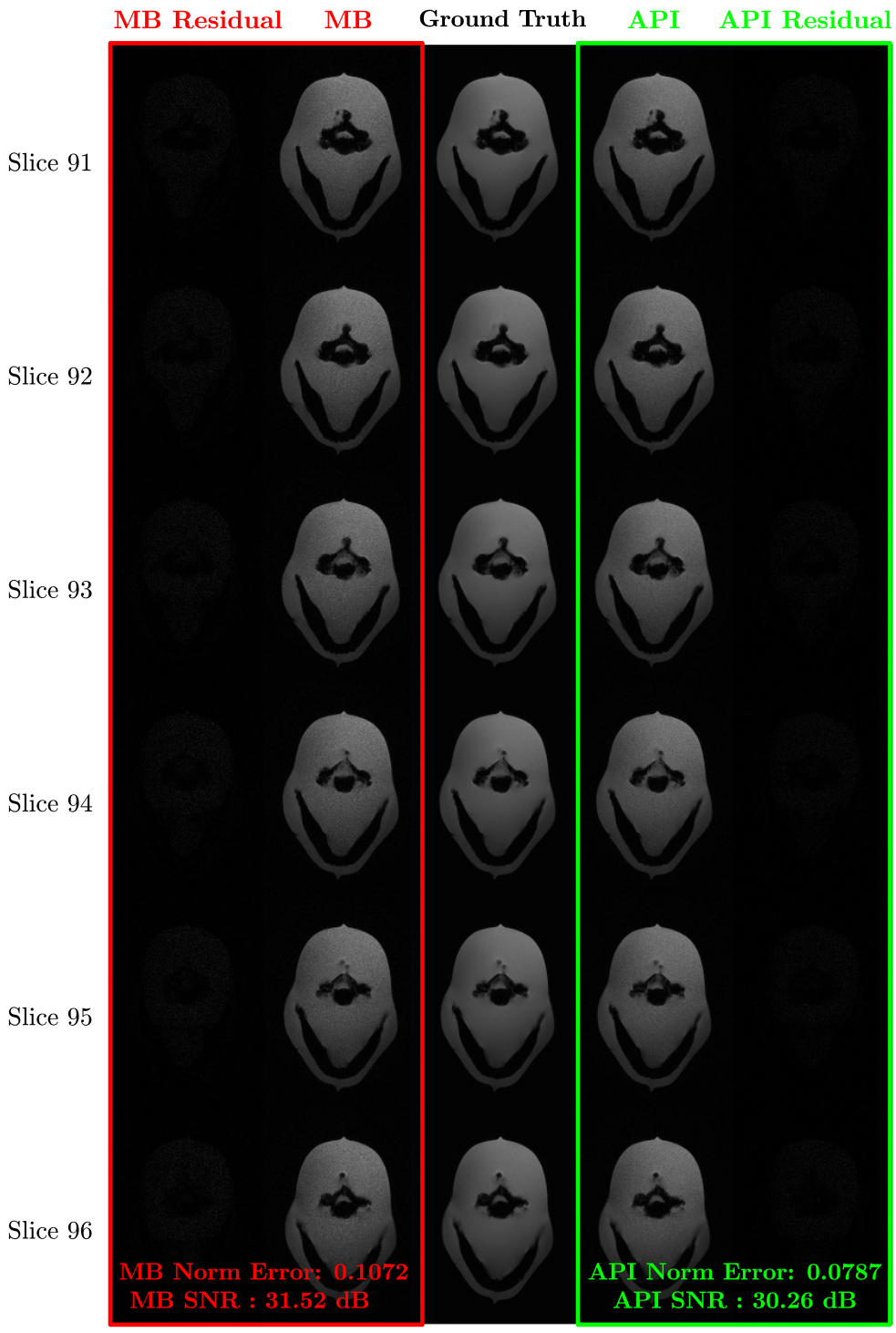


Figure B.16: 3D Recovery for Slices 91-96 when MB and API are used to recover the underlying signal for an acceleration factor of 8. The recovery afforded by each method is plotted along with the underlying ground truth and residuals. For these 6 slices, API reconstructs the underlying signal with approximately $36\%$ lower error $(0.0787)$ versus MB's $(0.1072)$.

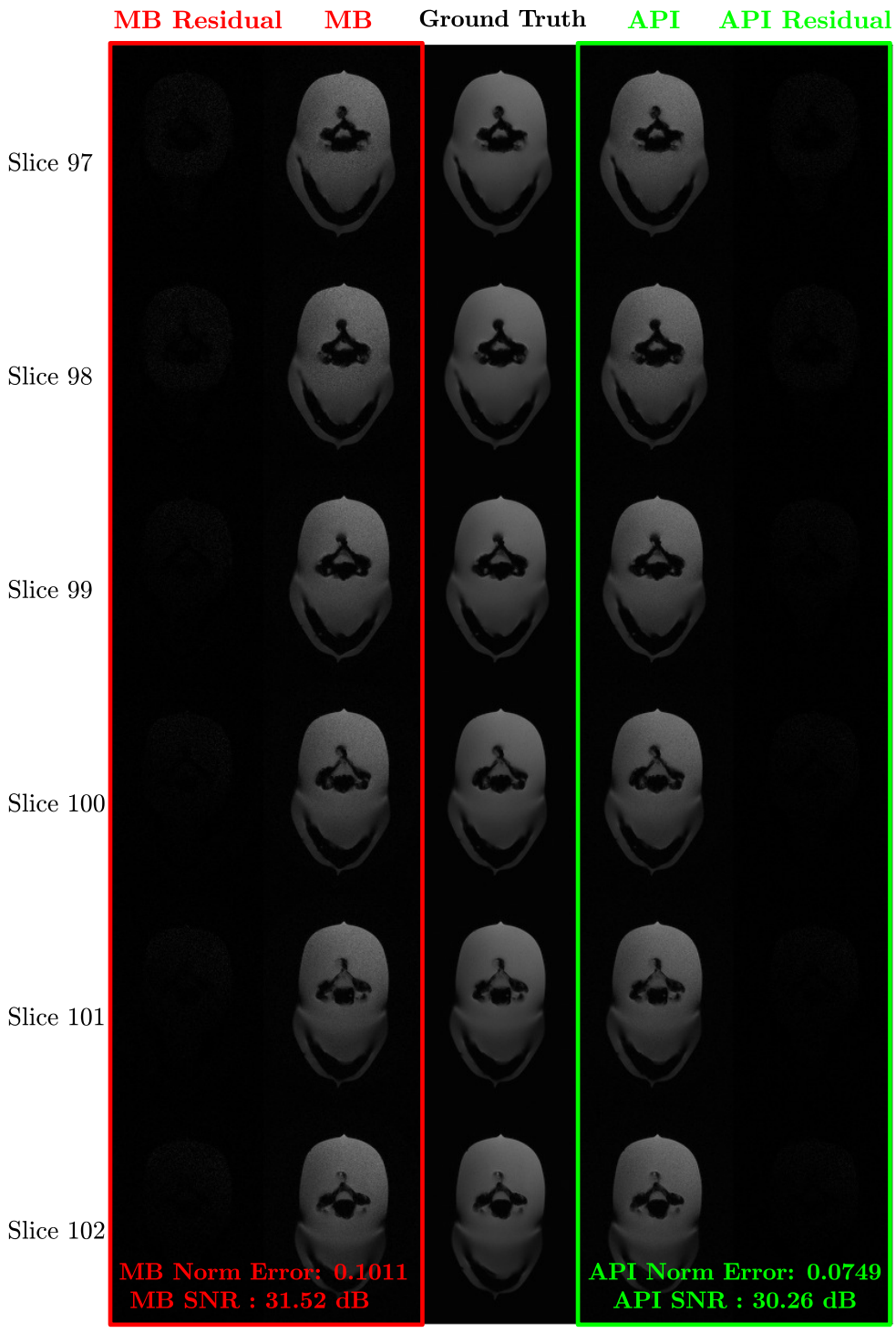


Figure B.17: 3D Recovery for Slices 97-102 when MB and API are used to recover the underlying signal for an acceleration factor of 8. The recovery afforded by each method is plotted along with the underlying ground truth and residuals. For these 6 slices, API reconstructs the underlying signal with approximately $35\%$ lower error $(0.0749)$ versus MB's $(0.1011)$.

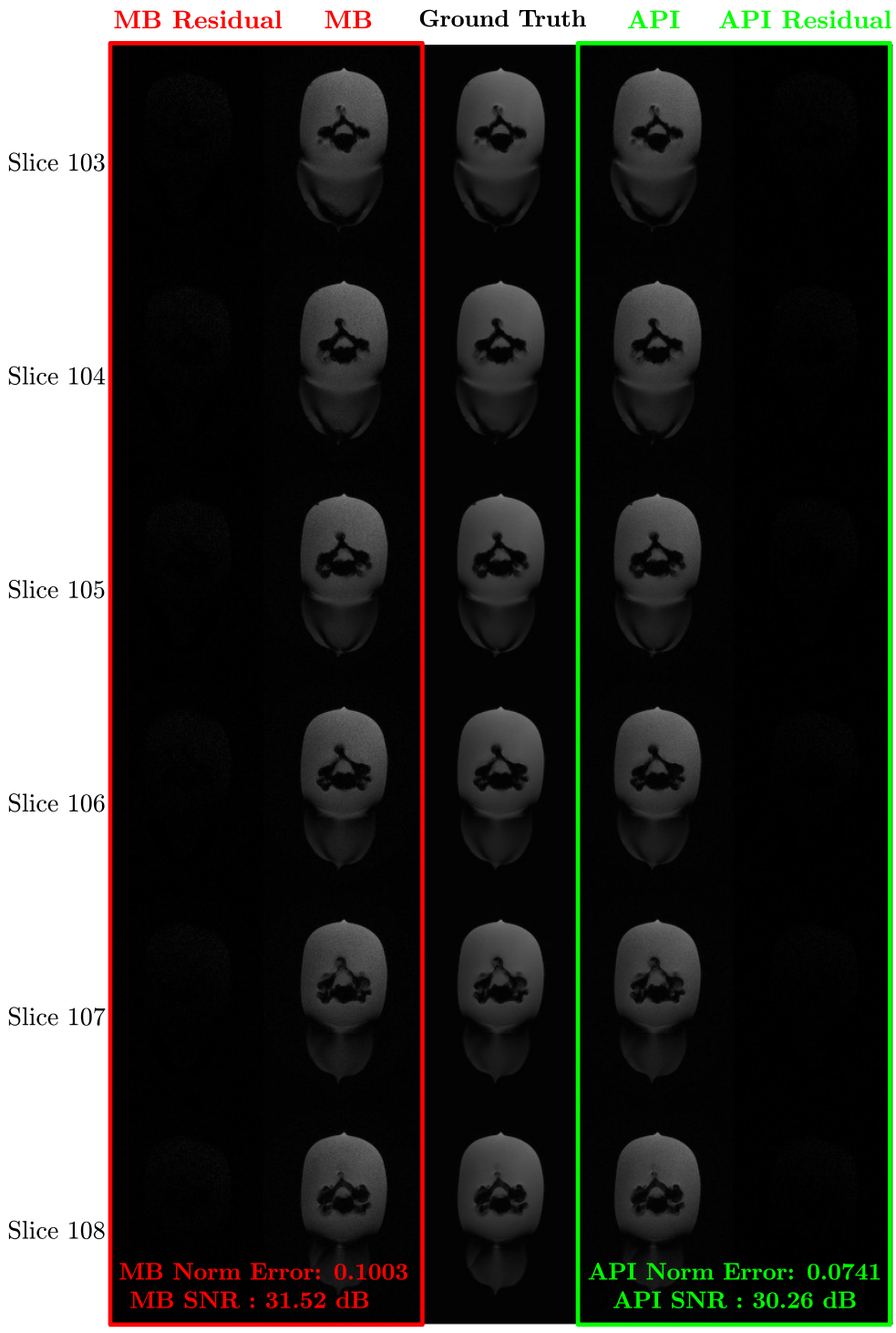


Figure B.18: 3D Recovery for Slices 103-108 when MB and API are used to recover the underlying signal for an acceleration factor of 8. The recovery afforded by each method is plotted along with the underlying ground truth and residuals. For these 6 slices, API reconstructs the underlying signal with approximately $35\%$ lower error $(0.0741)$ versus MB's $(0.1003)$.

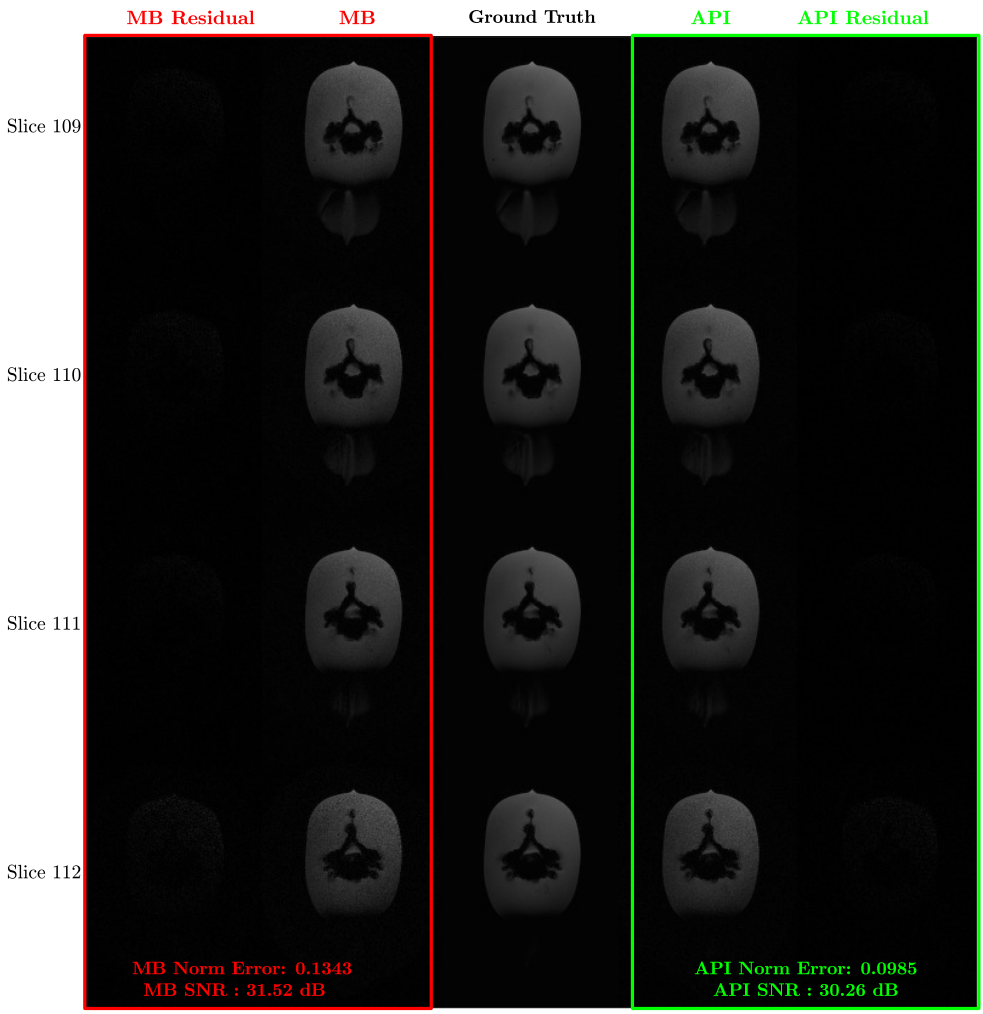


Figure B.19: 3D Recovery for Slices 109-112 when MB and API are used to recover the underlying signal for an acceleration factor of 8. The recovery afforded by each method is plotted along with the underlying ground truth and residuals. For these 4 slices, API reconstructs the underlying signal with approximately $36\%$ lower error $(0.0985)$ versus MB's $(0.1343)$.

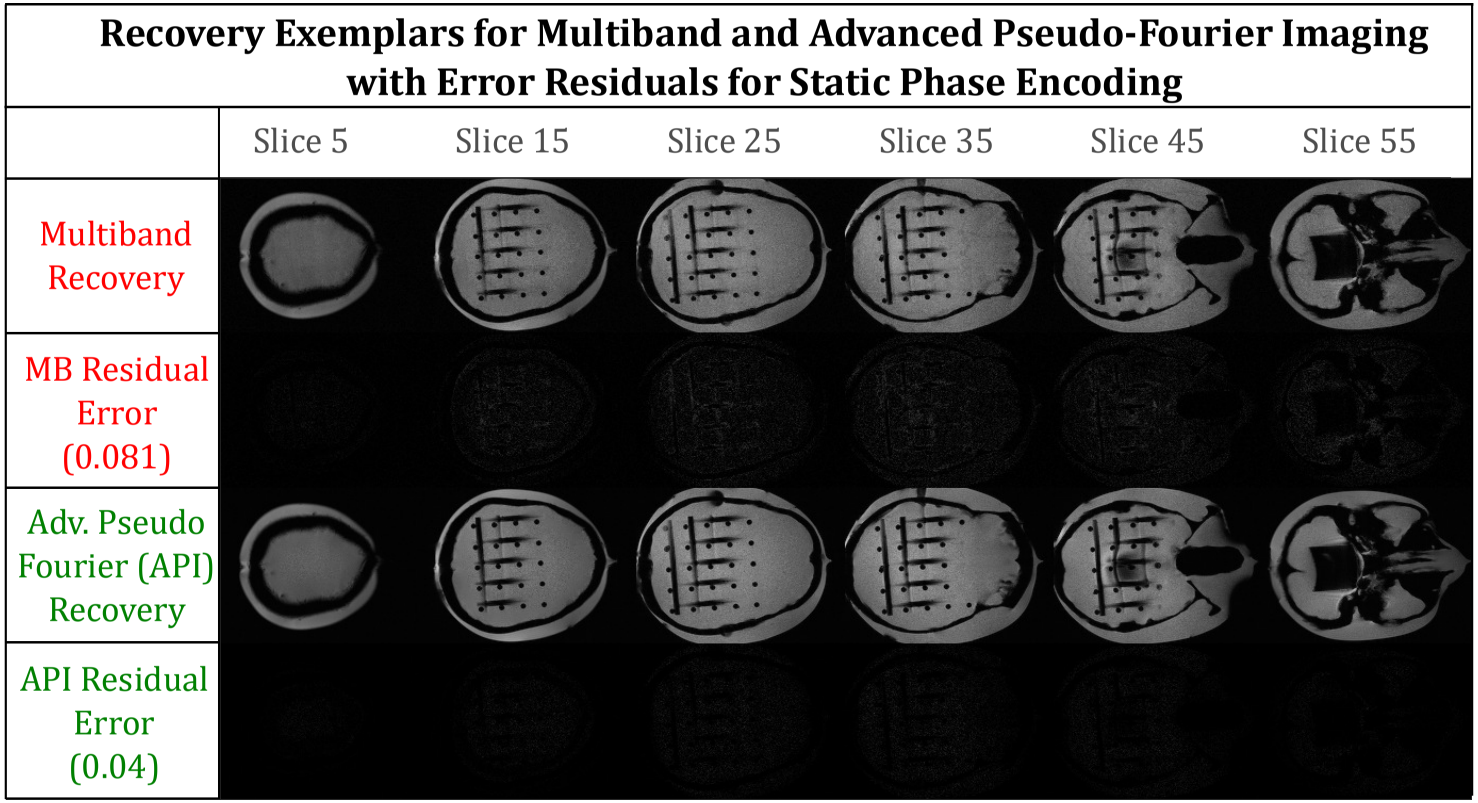


Figure B.20: In this example, instead of varying phase continuously (even within each slice), each slice was provided a phase that varied linearly between slices (the phase was constant within each window). Even with this type of formulation, for an acceleration factor of 8, API is able to recover the underlying signal with greater fidelity with a nearly $50\%$ reduction in error.

## REFERENCES


[1] P. L. Combettes and J.-C. Pesquet, "Proximal splitting methods in signal processing," in *Fixed-point algorithms for inverse problems in science and engineering*, Springer, 2011, pp. 185–212.

[2] W. Zuo, D. Meng, L. Zhang, X. Feng, and D. Zhang, "A generalized iterated shrinkage algorithm for non-convex sparse coding," in *Proceedings of the IEEE international conference on computer vision*, 2013, pp. 217–224.

[3] A. N. Tikhonov, "On the stability of inverse problems," in *Dokl. Akad. Nauk SSSR*, vol. 39, 1943, pp. 195–198.

[4] A. Tikhonov and V. Y. Arsenin, *Methods for solving ill-posed problems*. John Wiley and Sons, Inc, 1977.

[5] E. J. Candes, J. K. Romberg, and T. Tao, "Stable signal recovery from incomplete and inaccurate measurements," *Communications on pure and applied mathematics*, vol. 59, no. 8, pp. 1207–1223, 2006.

[6] J. Romberg, "Imaging via compressive sampling [introduction to compressive sampling and recovery via convex programming]," *IEEE Signal Processing Magazine*, vol. 25, no. 2, pp. 14–20, 2008.

[7] D. L. Donoho, "Compressed sensing," *Information Theory, IEEE Transactions on*, vol. 52, no. 4, pp. 1289–1306, 2006.

[8] J. M. Bioucas-Dias and M. A. Figueiredo, "A new twist: Two-step iterative shrinkage/thresholding algorithms for image restoration," *Image Processing, IEEE Transactions on*, vol. 16, no. 12, pp. 2992–3004, 2007.

[9] A. Beck and M. Teboulle, "A fast iterative shrinkage-thresholding algorithm for linear inverse problems," *SIAM Journal on Imaging Sciences*, vol. 2, no. 1, pp. 183–202, 2009.

[10] ——, "Fast gradient-based algorithms for constrained total variation image denoising and deblurring problems," *Image Processing, IEEE Transactions on*, vol. 18, no. 11, pp. 2419–2434, 2009.

[11] E. Candes and J. Romberg, "Sparsity and incoherence in compressive sampling," *Inverse problems*, vol. 23, no. 3, p. 969, 2007.

[12] E. J. Candes and J. K. Romberg, "Signal recovery from random projections," in *Electronic Imaging 2005*, International Society for Optics and Photonics, 2005, pp. 76–86.

[13] E. J. Candes and T. Tao, "Decoding by linear programming," *IEEE transactions on information theory*, vol. 51, no. 12, pp. 4203–4215, 2005.

[14] ——, "Near-optimal signal recovery from random projections: Universal encoding strategies?" *IEEE transactions on information theory*, vol. 52, no. 12, pp. 5406–5425, 2006.

[15] M. Lustig, D. Donoho, and J. M. Pauly, "Sparse mri: The application of compressed sensing for rapid mr imaging," *Magnetic resonance in medicine*, vol. 58, no. 6, pp. 1182–1195, 2007.

[16] G.-H. Chen, J. Tang, and S. Leng, "Prior image constrained compressed sensing (piccs): A method to accurately reconstruct dynamic ct images from highly undersampled projection data sets," *Medical physics*, vol. 35, no. 2, pp. 660–663, 2008.

[17] R. Otazo, D. Kim, L. Axel, and D. K. Sodickson, "Combination of compressed sensing and parallel imaging for highly accelerated first-pass cardiac perfusion mri," *Magnetic Resonance in Medicine*, vol. 64, no. 3, pp. 767–776, 2010.

[18] R. Baraniuk and P. Steeghs, "Compressive radar imaging," in *Radar Conference, 2007 IEEE*, IEEE, 2007, pp. 128–133.

[19] M. Herman and T. Strohmer, "Compressed sensing radar," in *Radar Conference, 2008. RADAR'08. IEEE*, IEEE, 2008, pp. 1–6.

[20] I. Daubechies, M. Defrise, and C. De Mol, "An iterative thresholding algorithm for linear inverse problems with a sparsity constraint," *arXiv preprint math/0307152*, 2003.

[21] Y. Nesterov, "A method of solving a convex programming problem with convergence rate o (1/k2)," in *Soviet Mathematics Doklady*, vol. 27, 1983, pp. 372–376.

[22] S. Becker, J. Bobin, and E. J. Candès, "Nesta: A fast and accurate first-order method for sparse recovery," *SIAM Journal on Imaging Sciences*, vol. 4, no. 1, pp. 1–39, 2011.

[23] M. Grant and S. Boyd, "Graph implementations for nonsmooth convex programs," in *Recent Advances in Learning and Control*, ser. Lecture Notes in Control and Information Sciences, V. Blondel, S. Boyd, and H. Kimura, Eds., `http://stanford.edu/~boyd/graph_dcp.html`, Springer-Verlag Limited, 2008, pp. 95–110.

[24] ——, *CVX: Matlab software for disciplined convex programming, version 2.1*, `http://cvxr.com/cvx`, Mar. 2014.

[25] R. Carrillo, J. McEwen, and Y. Wiaux, "Sparsity averaging reweighted analysis (sara): A novel algorithm for radio-interferometric imaging," *Monthly Notices of the Royal Astronomical Society*, vol. 426, no. 2, pp. 1223–1234, 2012.

[26] R. E. Carrillo, J. D. McEwen, D. Van De Ville, J.-P. Thiran, and Y. Wiaux, "Sparsity averaging for compressive imaging," *Signal Processing Letters, IEEE*, vol. 20, no. 6, pp. 591–594, 2013.

[27] E. Y. Sidky, R. Chartrand, and X. Pan, "Image reconstruction from few views by non-convex optimization," in *Nuclear Science Symposium Conference Record, 2007. NSS'07. IEEE*, IEEE, vol. 5, 2007, pp. 3526–3530.

[28] R. Chartrand, "Nonconvex compressive sensing and reconstruction of gradient-sparse images: Random vs. tomographic fourier sampling," in *Image Processing, 2008. ICIP 2008. 15th IEEE International Conference on*, IEEE, 2008, pp. 2624–2627.

[29] R. Chartrand, E. Y. Sidky, and X. Pan, "Nonconvex compressive sensing for x-ray ct: An algorithm comparison," in *Signals, Systems and Computers, 2013 Asilomar Conference on*, IEEE, 2013, pp. 665–669.

[30] P. Ochs, Y. Chen, T. Brox, and T. Pock, "Ipiano: Inertial proximal algorithm for non-convex optimization," *arXiv preprint arXiv:1404.4805*, 2014.

[31] R. Chartrand, "Fast algorithms for nonconvex compressive sensing: Mri reconstruction from very few data," in *Biomedical Imaging: From Nano to Macro, 2009. ISBI'09. IEEE International Symposium on*, IEEE, 2009, pp. 262–265.

[32] J. Trzasko, C. Haider, and A. Manduca, "Practical nonconvex compressive sensing reconstruction of highly-accelerated 3d parallel mr angiograms," in *Biomedical Imaging: From Nano to Macro, 2009. ISBI'09. IEEE International Symposium on*, IEEE, 2009, pp. 274–277.

[33] J. D. Trzasko, C. R. Haider, E. A. Borisch, N. G. Campeau, J. F. Glockner, S. J. Riederer, and A. Manduca, "Sparse-capr: Highly accelerated 4d ce-mra with parallel imaging and nonconvex compressive sensing," *Magnetic Resonance in Medicine*, vol. 66, no. 4, pp. 1019–1032, 2011.

[34] J. Trzasko, A. Manduca, and E. Borisch, "Sparse mri reconstruction via multiscale l0-continuation," in *Statistical Signal Processing, 2007. SSP'07. IEEE/SP 14th Workshop on*, IEEE, 2007, pp. 176–180.

[35] J. Trzasko and A. Manduca, "Highly undersampled magnetic resonance image reconstruction via homotopic-minimization," *Medical imaging, iEEE Transactions on*, vol. 28, no. 1, pp. 106–121, 2009.

[36] E. J. Candes, M. B. Wakin, and S. P. Boyd, "Enhancing sparsity by reweighted 1 minimization," *Journal of Fourier analysis and applications*, vol. 14, no. 5-6, pp. 877–905, 2008.

[37] R. Chartrand and W. Yin, "Iteratively reweighted algorithms for compressive sensing," in *Acoustics, speech and signal processing, 2008. ICASSP 2008. IEEE international conference on*, IEEE, 2008, pp. 3869–3872.

[38] D. Needell, "Noisy signal recovery via iterative reweighted l1-minimization," in *Signals, Systems and Computers, 2009 Conference Record of the Forty-Third Asilomar Conference on*, IEEE, 2009, pp. 113–117.

[39] M. S. Asif and J. Romberg, "Fast and accurate algorithms for re-weighted l1-norm minimization," 2012.

[40] T. Blumensath, M. Yaghoobi, and M. E. Davies, "Iterative hard thresholding and l0 regularisation," in *Acoustics, Speech and Signal Processing, 2007. ICASSP 2007. IEEE International Conference on*, IEEE, vol. 3, 2007, pp. III–877.

[41] L. Mancera and J. Portilla, "L0-norm-based sparse representation through alternate projections.," in *ICIP*, Citeseer, 2006, pp. 2089–2092.

[42] M. Hyder and K. Mahata, "An approximate l0 norm minimization algorithm for compressed sensing," in *Acoustics, Speech and Signal Processing, 2009. ICASSP 2009. IEEE International Conference on*, IEEE, 2009, pp. 3365–3368.

[43] J. Portilla, "Image restoration through l0 analysis-based sparse optimization in tight frames," in *Image Processing (ICIP), 2009 16th IEEE International Conference on*, IEEE, 2009, pp. 3909–3912.

[44] T. Blumensath and M. E. Davies, "Iterative thresholding for sparse approximations," *Journal of Fourier Analysis and Applications*, vol. 14, no. 5-6, pp. 629–654, 2008.

[45] T. Blumensath, "Accelerated iterative hard thresholding," *Signal Processing*, vol. 92, no. 3, pp. 752–756, 2012.

[46] M. Elad, P. Milanfar, and R. Rubinstein, "Analysis versus synthesis in signal priors," *Inverse problems*, vol. 23, no. 3, p. 947, 2007.

[47] D. L. Donoho, "High-dimensional centrally symmetric polytopes with neighborliness proportional to dimension," *Discrete & Computational Geometry*, vol. 35, no. 4, pp. 617–652, 2006.

[48] I. W. Selesnick and M. A. Figueiredo, "Signal restoration with overcomplete wavelet transforms: Comparison of analysis and synthesis priors," in *SPIE Optical Engineering+ Applications*, International Society for Optics and Photonics, 2009, pp. 74460D–74460D.

[49] E. J. Candes, M. B. Wakin, and S. P. Boyd, "Enhancing sparsity by reweighted 1 minimization," *Journal of Fourier analysis and applications*, vol. 14, no. 5-6, pp. 877–905, 2008.

[50] E. J. Candes, Y. C. Eldar, D. Needell, and P. Randall, "Compressed sensing with coherent and redundant dictionaries," *Applied and Computational Harmonic Analysis*, vol. 31, no. 1, pp. 59–73, 2011.

[51] N. Parikh and S. Boyd, "Proximal algorithms," *Foundations and Trends in optimization*, vol. 1, no. 3, pp. 123–231, 2013.

[52] P. L. Combettes and V. R. Wajs, "Signal recovery by proximal forward-backward splitting," *Multiscale Modeling & Simulation*, vol. 4, no. 4, pp. 1168–1200, 2005.

[53] P. L. Combettes and J.-C. Pesquet, "A douglas–rachford splitting approach to nonsmooth convex variational signal recovery," *Selected Topics in Signal Processing, IEEE Journal of*, vol. 1, no. 4, pp. 564–574, 2007.

[54] N. Pustelnik, C. Chaux, and J.-C. Pesquet, "Parallel proximal algorithm for image restoration using hybrid regularization," *Image Processing, IEEE Transactions on*, vol. 20, no. 9, pp. 2450–2462, 2011.

[55] J. Kovacevic and A. Chebira, "Life beyond bases: The advent of frames (part i)," *Signal Processing Magazine, IEEE*, vol. 24, no. 4, pp. 86–104, 2007.

[56] ——, "Life beyond bases: The advent of frames (part ii)," *Signal Processing Magazine, IEEE*, vol. 24, no. 5, pp. 115–125, 2007.

[57] I. W. Selesnick, R. G. Baraniuk, and N. C. Kingsbury, "The dual-tree complex wavelet transform," *Signal Processing Magazine, IEEE*, vol. 22, no. 6, pp. 123–151, 2005.

[58] I. W. Selesnick, "The double-density dual-tree dwt," *Signal Processing, IEEE Transactions on*, vol. 52, no. 5, pp. 1304–1314, 2004.

[59] P. Hill, A. Achim, and D. Bull, "The undecimated dual tree complex wavelet transform and its application to bivariate image denoising using a cauchy model," in *Image Processing (ICIP), 2012 19th IEEE International Conference on*, 2012, pp. 1205–1208.

[60] R. Chartrand, "Exact reconstruction of sparse signals via nonconvex minimization," *Signal Processing Letters, IEEE*, vol. 14, no. 10, pp. 707–710, 2007.

[61] M. A. Figueiredo, "Some advances on the use of admm in imaging: Non-periodic and blind deconvolution," First French-German Mathematical Image Analysis Conference, 2014.

[62] C. Wagner and I. W. Selesnick. (2004). 2-d double-density complex wavelet transform, (visited on 07/20/2014).

[63] E. Candes, L. Demanet, D. Donoho, and L. Ying, "Fast discrete curvelet transforms," *Multiscale Modeling & Simulation*, vol. 5, no. 3, pp. 861–899, 2006.

[64] Y. Lou, T. Zeng, S. Osher, and J. Xin, "A weighted difference of anisotropic and isotropic total variation model for image processing," University of California at Los Angeles, Department of Mathematics, Tech. Rep., 2014.

[65] E. Y. Sidky, J. H. Jørgensen, and X. Pan, "Convex optimization problem prototyping for image reconstruction in computed tomography with the chambolle–pock algorithm," *Physics in medicine and biology*, vol. 57, no. 10, p. 3065, 2012.

[66] M. S. Almeida and M. Figueiredo, "Deconvolving images with unknown boundaries using the alternating direction method of multipliers," *IEEE Transactions on Image processing*, vol. 22, no. 8, pp. 3074–3086, 2013.

[67] R. Chartrand and W. Yin, "Iteratively reweighted algorithms for compressive sensing," in *Acoustics, speech and signal processing, 2008. ICASSP 2008. IEEE international conference on*, IEEE, 2008, pp. 3869–3872.

[68] R. E. Carrillo. (2013). Sopt: Sparse optimization, (visited on 05/15/2014).

[69] N. Zachariah. (2015). Ian : Non convex signal recovery.

[70] OsiriX. (2014). Dicom sample image set.

[71] S. Mallat and G. Yu, "Super-resolution with sparse mixing estimators," *Image Processing, IEEE Transactions on*, vol. 19, no. 11, pp. 2889–2900, 2010.

[72] W. Dong, L. Zhang, R. Lukac, and G. Shi, "Sparse representation based image interpolation with nonlocal autoregressive modeling," *IEEE Transactions on Image Processing*, vol. 22, no. 4, pp. 1382–1394, 2013.

[73] W. Dong, G. Shi, and X. Li, "Nonlocal image restoration with bilateral variance estimation: A low-rank approach," *Image Processing, IEEE Transactions on*, vol. 22, no. 2, pp. 700–711, 2013.

[74] Z. Wang, A. C. Bovik, H. R. Sheikh, and E. P. Simoncelli, "Image quality assessment: From error visibility to structural similarity," *Image Processing, IEEE Transactions on*, vol. 13, no. 4, pp. 600–612, 2004.

[75] K. Dabov, A. Foi, V. Katkovnik, and K. Egiazarian, "Image denoising by sparse 3-d transform-domain collaborative filtering," *Image Processing, IEEE Transactions on*, vol. 16, no. 8, pp. 2080–2095, 2007.

[76] P. Chatterjee and P. Milanfar, "Patch-based near-optimal image denoising," *Image Processing, IEEE Transactions on*, vol. 21, no. 4, pp. 1635–1649, 2012.

[77] X. Kong, K. Li, Q. Yang, L. Wenyin, and M.-H. Yang, "A new image quality metric for image auto-denoising," in *Computer Vision (ICCV), 2013 IEEE International Conference on*, IEEE, 2013, pp. 2888–2895.

[78] A. Ahmed, J Romberg, and B Recht, "Blind deconvolution using convex programming," 2012.

[79] R. Bruck, T. Kuczumow, and S. Reich, "Convergence of iterates of asymptotically nonexpansive mappings in banach spaces with the uniform opial property," in *Colloq. Math*, vol. 65, 1993, pp. 169–179.

[80] K. Lange, D. R. Hunter, and I. Yang, "Optimization transfer using surrogate objective functions," *Journal of computational and graphical statistics*, vol. 9, no. 1, pp. 1–20, 2000.

[81] T. Blumensath and M. E. Davies, "Iterative thresholding for sparse approximations," *Journal of Fourier Analysis and Applications*, vol. 14, no. 5-6, pp. 629–654, 2008.

[82] S. Voronin and R. Chartrand, "A new generalized thresholding algorithm for inverse problems with sparsity constraints," in *Acoustics, Speech and Signal Processing (ICASSP), 2013 IEEE International Conference on*, IEEE, 2013, pp. 1636–1640.

[83] F. Browder and W. V. Petryshyn, "Construction of fixed points of nonlinear mappings in hilbert space," *Journal of Mathematical Analysis and Applications*, vol. 20, no. 2, pp. 197–228, 1967.

[84] Z. Opial, "Weak convergence of the sequence of successive approximations for nonexpansive mappings," *Bull. Amer. Math. Soc.*, vol. 73, no. 4, pp. 591–597, Jul. 1967.

[85] H. H. Bauschke and P. L. Combettes, *Convex analysis and monotone operator theory in hilbert spaces*. Springer Science & Business Media, 2011.

[86] A. R. De Pierro, "A modified expectation maximization algorithm for penalized likelihood estimation in emission tomography.," *IEEE transactions on medical imaging*, vol. 14, no. 1, pp. 132–137, 1994.

[87] D. N. Ku, D. P. Giddens, C. K. Zarins, and S. Glagov, "Pulsatile flow and atherosclerosis in the human carotid bifurcation. positive correlation between plaque location and low oscillating shear stress.," *Arteriosclerosis, Thrombosis, and Vascular Biology*, vol. 5, no. 3, pp. 293–302, 1985.

[88] S Glagov, C. Zarins, D. Giddens, and D. N. Ku, "Hemodynamics and atherosclerosis. insights and perspectives gained from studies of human arteries.," *Archives of pathology & laboratory medicine*, vol. 112, no. 10, pp. 1018–1031, 1988.

[89] T. B. Oliver, G. A. Lammie, A. R. Wright, J. Wardlaw, S. G. Patel, R. Peek, C. V. Ruckley, and D. A. Collie, "Atherosclerotic plaque at the carotid bifurcation: Ct angiographic appearance with histopathologic correlation," *American journal of neuroradiology*, vol. 20, no. 5, pp. 897–901, 1999.

[90] G. N. Foutrakis, H. Yonas, and R. J. Sclabassi, "Saccular aneurysm formation in curved and bifurcating arteries," *American Journal of Neuroradiology*, vol. 20, no. 7, pp. 1309–1317, 1999.

[91] S. Ramani, T. Blu, and M. Unser, "Monte-carlo sure: A black-box optimization of regularization parameters for general denoising algorithms," *Image Processing, IEEE Transactions on*, vol. 17, no. 9, pp. 1540–1554, 2008.

[92] C. M. Stein, "Estimation of the mean of a multivariate normal distribution," *The annals of Statistics*, pp. 1135–1151, 1981.

[93] Z. Xu, X. Chang, F. Xu, and H. Zhang, "L(1/2) regularization: A thresholding representation theory and a fast solver," *IEEE Transactions on neural networks and learning systems*, vol. 23, no. 7, pp. 1013–1027, 2012.

[94] R. W. Brown, Y.-C. N. Cheng, E. M. Haacke, M. R. Thompson, and R. Venkatesan, *Magnetic resonance imaging: Physical principles and sequence design*. John Wiley & Sons, 2014.

[95] D. G. Nishimura, *Principles of magnetic resonance imaging*. Stanford University, 1996.

[96] M. A. Griswold, P. M. Jakob, R. M. Heidemann, M. Nittka, V. Jellus, J. Wang, B. Kiefer, and A. Haase, "Generalized autocalibrating partially parallel acquisitions (grappa)," *Magnetic resonance in medicine*, vol. 47, no. 6, pp. 1202–1210, 2002.

[97] P. M. Jakob, M. A. Grisowld, R. R. Edelman, and D. K. Sodickson, "Auto-smash: A self-calibrating technique for smash imaging," *Magnetic Resonance Materials in Physics, Biology and Medicine*, vol. 7, no. 1, pp. 42–54, 1998.

[98] R. M. Heidemann, M. A. Griswold, A. Haase, and P. M. Jakob, "Vd-auto-smash imaging," *Magnetic Resonance in Medicine*, vol. 45, no. 6, pp. 1066–1074, 2001.

[99] M. Blaimer, F. Breuer, M. Mueller, R. M. Heidemann, M. A. Griswold, and P. M. Jakob, "Smash, sense, pils, grappa: How to choose the optimal method," *Topics in Magnetic Resonance Imaging*, vol. 15, no. 4, pp. 223–236, 2004.

[100] J. Cuppen and A. van Est, "Reducing mr imaging time by one-sided reconstruction," *Magnetic Resonance Imaging*, vol. 5, no. 6, pp. 526–527, 1987.

[101] D Faul, J Abart, and P Margosian, "Quick measurement of magnetic field variations within the body," *Radiology*, vol. 153, p. 303, 1984.

[102] D. C. Noll, D. G. Nishimura, and A. Macovski, "Homodyne detection in magnetic resonance imaging," *IEEE transactions on medical imaging*, vol. 10, no. 2, pp. 154–163, 1991.

[103] M. Lustig, D. L. Donoho, J. M. Santos, and J. M. Pauly, "Compressed sensing mri," *Signal Processing Magazine, IEEE*, vol. 25, no. 2, pp. 72–82, 2008.

[104] H. Jung, K. Sung, K. S. Nayak, E. Y. Kim, and J. C. Ye, "K-t focuss: A general compressed sensing framework for high resolution dynamic mri," *Magnetic Resonance in Medicine*, vol. 61, no. 1, pp. 103–116, 2009.

[105] U. Gamper, P. Boesiger, and S. Kozerke, "Compressed sensing in dynamic mri," *Magnetic Resonance in Medicine*, vol. 59, no. 2, pp. 365–373, 2008.

[106] H. Gao, S. Rapacchi, D. Wang, J. Moriarty, C. Meehan, J. Sayre, G. Laub, P. Finn, and P. Hu, "Compressed sensing using prior rank, intensity and sparsity model

(prism): Applications in cardiac cine mri," in *Proceedings of the 20th Annual Meeting of ISMRM, Melbourne, Australia*, 2012, p. 2242.

[107] R. Otazo, E. Candès, and D. K. Sodickson, "Low-rank plus sparse matrix decomposition for accelerated dynamic mri with separation of background and dynamic components," *Magnetic Resonance in Medicine*, vol. 73, no. 3, pp. 1125–1136, 2015.

[108] P. C. Lauterbur, "Image formation by induced local interactions: Examples employing nuclear magnetic resonance," 1973.

[109] C. Mistretta, O Wieben, J Velikina, W Block, J Perry, Y. Wu, and K Johnson, "Highly constrained backprojection for time-resolved mri," *Magnetic resonance in medicine*, vol. 55, no. 1, pp. 30–40, 2006.

[110] C. Ahn, J. Kim, and Z. Cho, "High-speed spiral-scan echo planar nmr imaging-i," *IEEE transactions on medical imaging*, vol. 5, no. 1, pp. 2–7, 1986.

[111] P Mansfield, A. A. Maudsley, and T Bains, "Fast scan proton density imaging by nmr," *Journal of Physics E: Scientific Instruments*, vol. 9, no. 4, p. 271, 1976.

[112] K. P. Pruessmann, M. Weiger, M. B. Scheidegger, P. Boesiger, *et al.*, "Sense: Sensitivity encoding for fast mri," *Magnetic resonance in medicine*, vol. 42, no. 5, pp. 952–962, 1999.

[113] S. Moeller, E. Yacoub, C. A. Olman, E. Auerbach, J. Strupp, N. Harel, and K. Uğurbil, "Multiband multislice ge-epi at 7 tesla, with 16-fold acceleration using partial parallel imaging with application to high spatial and temporal whole-brain fmri," *Magnetic Resonance in Medicine*, vol. 63, no. 5, pp. 1144–1153, 2010.

[114] M. Barth, F. Breuer, P. J. Koopmans, D. G. Norris, and B. A. Poser, "Simultaneous multislice (sms) imaging techniques," *Magnetic Resonance in Medicine*, vol. 75, no. 1, pp. 63–81, 2016.

[115] J. Xu, S. Moeller, E. J. Auerbach, J. Strupp, S. M. Smith, D. A. Feinberg, E. Yacoub, and K. Uğurbil, "Evaluation of slice accelerations using multiband echo planar imaging at 3t," *Neuroimage*, vol. 83, pp. 991–1001, 2013.

[116] F. A. Breuer, M. Blaimer, R. M. Heidemann, M. F. Mueller, M. A. Griswold, and P. M. Jakob, "Controlled aliasing in parallel imaging results in higher acceleration (caipirinha) for multi-slice imaging," *Magnetic Resonance in Medicine*, vol. 53, no. 3, pp. 684–691, 2005.

[117] K. Setsompop, B. A. Gagoski, J. R. Polimeni, T. Witzel, V. J. Wedeen, and L. L. Wald, "Blipped-controlled aliasing in parallel imaging for simultaneous multislice

echo planar imaging with reduced g-factor penalty," *Magnetic Resonance in Medicine*, vol. 67, no. 5, pp. 1210–1224, 2012.

[118] S. F. Cauley, J. R. Polimeni, H. Bhat, L. L. Wald, and K. Setsompop, "Interslice leakage artifact reduction technique for simultaneous multislice acquisitions," *Magnetic resonance in medicine*, vol. 72, no. 1, pp. 93–102, 2014.

[119] Y. M. Kadah and X. Hu, "Pseudo-fourier imaging (pfi): A technique for spatial encoding in mri," *Medical Imaging, IEEE Transactions on*, vol. 16, no. 6, pp. 893–902, 1997.

[120] S. Moeller, E. Yacoub, C. A. Olman, E. Auerbach, J. Strupp, N. Harel, and K. Uğurbil, "Multiband multislice ge-epi at 7 tesla, with 16-fold acceleration using partial parallel imaging with application to high spatial and temporal whole-brain fmri," *Magnetic Resonance in Medicine*, vol. 63, no. 5, pp. 1144–1153, 2010.

[121] A. Wirgin, "The inverse crime," *arXiv preprint math-ph/0401050*, 2004.

[122] J.-F. Cai, E. J. Candès, and Z. Shen, "A singular value thresholding algorithm for matrix completion," *SIAM Journal on Optimization*, vol. 20, no. 4, pp. 1956–1982, 2010.

[123] M. R. Hestenes and E. Stiefel, *Methods of conjugate gradients for solving linear systems*. NBS, 1952, vol. 49.

[124] J. R. Shewchuk *et al.*, *An introduction to the conjugate gradient method without the agonizing pain*, 1994.

[125] S Moeller, J Xu, E. Auerbach, E Yacoub, and K Ugurbil, "Signal leakage (l-factor) as a measure for parallel imaging performance among simultaneously multi-slice (sms) excited and acquired signals," in *Proceedings of the 20th Annual Meeting of ISMRM, Melbourne, Australia*, 2012, p. 519.

[126] P. M. Robson, A. K. Grant, A. J. Madhuranthakam, R. Lattanzi, D. K. Sodickson, and C. A. McKenzie, "Comprehensive quantification of signal-to-noise ratio and g-factor for image-based and k-space-based parallel imaging reconstructions," *Magnetic resonance in medicine*, vol. 60, no. 4, pp. 895–907, 2008.

[127] J. Xu, S. Moeller, E. J. Auerbach, J. Strupp, S. M. Smith, D. A. Feinberg, E. Yacoub, and K. Uğurbil, "Evaluation of slice accelerations using multiband echo planar imaging at 3t," *Neuroimage*, vol. 83, pp. 991–1001, 2013.

[128] D. G. Norris, P. J. Koopmans, R. Boyacioğlu, and M. Barth, "Power independent of number of slices (pins) radiofrequency pulses for low-power simultaneous mul-

tislice excitation," *Magnetic resonance in medicine*, vol. 66, no. 5, pp. 1234–1240, 2011.

[129] S. Conolly, D. Nishimura, and A. Macovski, "Sweep-diagram analysis of selective adiabatic pulses," *Journal of Magnetic Resonance (1969)*, vol. 83, no. 3, pp. 549–564, 1989.

[130] G. H. Glover, "Phase-offset multiplanar (pomp) volume imaging: A new technique," *Journal of Magnetic Resonance Imaging*, vol. 1, no. 4, pp. 457–461, 1991.